

THESE EN CO-TUTELLE
entre l'Ecole Centrale de Lyon (France)
et l'Université Taras Chevchenko de Kyiv (Ukraine)
(Discipline : électronique et automatique)

présentée devant
l'Ecole Centrale de Lyon
pour obtenir le grade de
DOCTEUR DE L'ECOLE CENTRALE DE LYON

soutenue publiquement le 17 juillet 2007

par
Arthur BENOLOV

Nouveaux procédés d'élaboration et de mise en œuvre de capteurs et microsystèmes en silicium et silicium poreux par des méthodes luminescentes et électriques

Commission d'examen composée de :

Prof. Georges Bremond	Président
Prof. Valeriy Skrychevsky	Directeur de thèse (Ukraine)
Prof. Yves Robach	Directeur de thèse (France)
Dr. Michel Cabrera	Co-directeur de thèse (France)
Prof. Philippe Allongue	Rapporteur
Prof. Mykola Klyui	Rapporteur
Prof. Nicole Jaffrezic-Renault	Examinatrice invitée



ECOLE CENTRALE DE LYON
DIRECTION DE LA RECHERCHE

liste des personnes Habilitées à Diriger des Recherches en poste à l'Ecole Centrale de Lyon

Nom-Prénom	Corps grade	Laboratoire ou à défaut département ECL	Etablissement
AURIOL Philippe	professeur	CEGELY	ECL
BEROUAL Abderrahmane	professeur	CEGELY	ECL
BURET François	maître de conférences	CEGELY	ECL
JAFFREZIC-RENAULT Nicole	directeur de recherche	CEGELY	CNRS/ECL
KRÄHENBÜHL Laurent	directeur de recherche	CEGELY	CNRS/ECL
MARTELET Claude	professeur	CEGELY	ECL
NICOLAS Alain	professeur	CEGELY	ECL
NICOLAS Laurent	directeur de recherche	CEGELY	CNRS/ECL
SIMONET Pascal	chargé de recherche	CEGELY	CNRS/ECL
THOMAS Gérard	professeur	CEGELY	ECL
VOLLAIRE Christian	maître de conférences	CEGELY	ECL

Nbre Cégely 11

HELLOUIN Yves	maître de conférences	DER EEA	ECL
LE HELLEY Michel	professeur	DER EEA	ECL

Nbre DER EEA 2

GUIRALDENQ Pierre	professeur émérite	DER STMS	ECL
VINCENT Léo	professeur	DER STMS	ECL

Nbre DER STMS 2

LOHEAC Jean-Pierre	maître de conférences	ICJ	ECL
MAITRE Jean-François	professeur émérite	ICJ	ECL
MARION Martine	professeur	ICJ	ECL
MOUSSAOUI Mohand	professeur	ICJ	ECL
MUSY François	maître de conférences	ICJ	ECL
ROUY MIRONESCU Elisabeth	professeur	ICJ	ECL
ZINE Abdel-Malek	maître de conférences	ICJ	ECL

Nbre ICJ 7

DAVID Bertrand	professeur	ICTT	ECL
----------------	------------	------	-----

Nbre ICTT 1

CLOAREC Jean-Pierre	maître de conférences	LEOM	ECL
GAFFIOT Frédéric	professeur	LEOM	ECL
GAGNAIRE Alain	maître de conférences	LEOM	ECL
GARRIGUES Michel	directeur de recherche	LEOM	CNRS/ECL
GENDRY Michel	directeur de recherche	LEOM	CNRS/ECL
GRENET Geneviève	directeur de recherche	LEOM	CNRS/ECL
HOLLINGER Guy	directeur de recherche	LEOM	CNRS/ECL
JOSEPH Jacques	professeur	LEOM	ECL
KRAWCZYK Stanislas	directeur de recherche	LEOM	CNRS/ECL
MARTIN Jean-René	professeur émérite	LEOM	ECL
O'CONNOR Ian	maître de conférences	LEOM	ECL

PHANER-GOUTORBE Magali	professeur	LEOM	ECL
ROBACH Yves	professeur	LEOM	ECL
SOUTEYRAND Eliane	directeur de recherche	LEOM	CNRS/ECL
TARDY Jacques	directeur de recherche	LEOM	CNRS/ECL
VIKTOROVITCH Pierre	directeur de recherche	LEOM	CNRS/ECL

Nbre LEOM 16

CHEN Liming	professeur	LIRIS	ECL
-------------	------------	-------	-----

Nbre LIRIS 1

BAILLY Christophe	professeur	LMFA	ECL
BERTOGLIO Jean-Pierre	directeur de recherche	LMFA	CNRS/ECL
BLANC-BENON Philippe	directeur de recherche	LMFA	CNRS/ECL
CAMBON Claude	directeur de recherche	LMFA	CNRS/ECL
CARRIERE Philippe	chargé de recherche	LMFA	CNRS/ECL
CHAMPOUSSIN J-Claude	professeur émérite	LMFA	ECL
COMTE-BELLOT genevièvre	professeur émérite	LMFA	ECL
FERRAND Pascal	directeur de recherche	LMFA	CNRS/ECL
GALLAND Marie-Annick	maître de conférences	LMFA	ECL
GODEFERD Fabien	chargé de recherche	LMFA	CNRS/ECL
HENRY Daniel	directeur de recherche	LMFA	CNRS/ECL
JEANDEL Denis	professeur	LMFA	ECL
JUVE Daniel	professeur	LMFA	ECL
LE RIBAUT Catherine	chargée de recherche	LMFA	CNRS/ECL
LEBOEUF Francis	professeur	LMFA	ECL
PERKINS Richard	professeur	LMFA	ECL
ROGER Michel	professeur	LMFA	ECL
SCOTT Julian	professeur	LMFA	ECL
SIMOENS Serge	chargé de recherche	LMFA	CNRS/ECL
TREBINJAC Isabelle	maître de conférences	LMFA	ECL

Nbre LMFA 20

BENAYOUN Stéphane	professeur	LTDS	ECL
CAMBOU Bernard	professeur	LTDS	ECL
COUILLET Bernard	maître de conférences	LTDS	ECL
DANESCU Alexandre	maître de conférences	LTDS	ECL
FOUVRY Siegrid	chargé de recherche	LTDS	CNRS/ECL
GEORGES Jean-Marie	professeur émérite	LTDS	ECL
GUERRET Chrystelle	chargé de recherche	LTDS	CNRS/ECL
HERTZ Dominique	past	LTDS	ECL
ICHCHOU Mohamed	maître de conférences	LTDS	ECL
JEZEQUEL Louis	professeur	LTDS	ECL
JUVE Denyse	ingénieur de recherche	LTDS	ECL
KAPSA Philippe	directeur de recherche	LTDS	CNRS/ECL
LE BOT Alain	chargé de recherche	LTDS	CNRS/ECL
LOUBET Jean-Luc	directeur de recherche	LTDS	CNRS/ECL
MARTIN Jean-Michel	professeur	LTDS	ECL
MATHIA Thomas	directeur de recherche	LTDS	CNRS/ECL
MAZUYER Denis	professeur	LTDS	ECL
PERRET-LIAUDET Joël	maître de conférences	LTDS	ECL
SALVIA Michelle	maître de conférences	LTDS	ECL
SIDOROFF François	professeur	LTDS	ECL
STREMSDOERFER Guy	professeur	LTDS	ECL
THOUVEREZ Fabrice	professeur	LTDS	ECL
TREHEUX Daniel	professeur	LTDS	ECL
VANNES André-Bernard	professeur émérite	LTDS	ECL

Nbre LTDS 24

Total HdR ECL

84

Acknowledgments

The present work was carried out in the former laboratory LEOM (currently Institut des Nanotechnologies de Lyon, INL) of Ecole Centrale de Lyon (ECL) in collaboration with the Taras Shevchenko Kiev National University, Ukraine. These institutions are gratefully acknowledged. My research work in France was funded by CROUS through a scholarship from the French government.

I would like to thank my French supervisors, Pr. Jean-René Martin, Dr. Michel Cabrera and Pr. Yves Robach for accepting me in LEOM for my co-tutorial thesis. I am very grateful for their confidence in me and for our fruitful scientific discussions during these three years.

I warmly thank Pr. Valery Skryshevsky, for supervising my research work with great patience and care from the part of the Laboratory of Physics of Semiconductors (Kiev National University). His constant support and valuable advices have been very precious to me.

I am grateful to Pr. George Bremond for accepting to be a President of the examination commission. I warmly acknowledge Pr. Philippe Allongue, Pr. Mykola I. Klyui and Pr. Nicole Jaffrezic-Renault for accepting to judge my thesis, for all their remarks, comments and opinions which helped me to improve a description and a scientific interpretation of the results presented in this manuscript.

I am grateful to Dr. Gengzhau Xu, Dr. Radoslaw Mazurczyk, and Dr. Eli Bou Chakra for their kind help with some experiments I have carried out.

I thank Pr. Gennadiy Kuznetsov, Dr. Sergey Litvinenko and all my colleagues from the Laboratory of Physics of Semiconductors (Kiev National University) for the fruitful collaboration and their professional help.

My special thanks to Mme Therese Martin and Mr. Philippe Billoux who helped me a lot with my administrative adventures in France.

I want to warmly thank all my colleagues and friends for the unforgettable time we have had together:

- Yann Chevolut, Graziella El Khoury, Benjamin Hannes, and all others from LEOM;
- my Ukrainian colleagues: Irina Gavrilchenko, Yuriy Shulimov, Alexey Kozinets, Ivan Ivanov, and others;
- Nikolaich, Yurik, Andrey, Jackson and all other my university friends.

Liste of scientific publications and communications

Articles

1. A.I. Benilov, I.V. Gavrilchenko, I.V. Benilova, V.A. Skryshevsky, M. Cabrera, *Impact of Gas Adsorption and pH of Solutions on Radiative Lifetime of Modified Porous Silicon Layers*, Sensor Electronics and Microsystem Technologies, 2007, **2**: p. 35-40
2. A.I. Benilov, I.V. Gavrilchenko, I.V. Benilova, V.A. Skryshevsky, M. Cabrera, *Influence of pH Solution on Photoluminescence of Porous Silicon*, Sensors and Actuators A (Physical), 2007, **137**: 345-349
3. A.I. Benilov, M. Cabrera, V.A. Skryshevsky, J.-R. Martin, *Porous silicon localization for implementation in matrix biosensors*, Materials Science & Engineering B, 2007. **139**: p. 221-225
4. Benilov, A.I. and V.A. Skryshevsky, *Improvement over the luminescence lifetime measurement technique*. Bulletin of the University of Kiev, Series: Physics & Mathematics, 2006. **4**: p. 269-278
5. V. A. Skryshevsky, V. M. Zinchuk, A. I. Benilov, Yu. S. Milovanov, O. V. Tretyak, *Overcharging of porous silicon localized states at gas adsorption*, Semicond. Sci. Technol. 2006, **21**:p. 1605—1608
6. Benilov, A.I., A.I. Tsyganova, S.V. Litvinenko, and V.A. Skryshevsky, *Eddy-current application for conductivity measurement in semiconductor sensing systems*. Bulletin of the University of Kyiv, 2005. **8** (Radiophysics and electronics): p. 11-13.

Conferences

1. Benilov, A.I., I.V. Gavrilchenko, V.A. Skryshevsky, and M. Cabrera, *Influence of pH solution on photoluminescence of porous silicon*. in *2nd International Conference "Electronics and applied physics"*. 2006. Kyiv, Ukraine.

2. Benilov, A.I., I.V. Gavrilchenko, V.A. Skryshevsky, and M. Cabrera, *Impact of Gas Adsorption on Radiative Lifetime of Modified Porous Silicon Layers*. in 5th *International Conference on Porous Semiconductors Science and Technology*. 2006. Sitges-Barcelona, Spain.
3. V. Skryshevsky, S. Litvinenko, A. Kozinets, A. I. Benilov, Yu. Skryshevsky, I. V. Blonsky, *Analysis of surface recombination velocity in nanocrystalline silicon/silicon heterostructures: new photovoltaic transducing principle for sensor application*, in 1st *Ukraine-Korea Seminar on Nanophotonics and Nanophysics NANOPHOTONICS-NANOPHYSICS*. 2005, Kiev, Ukraine.
4. A. Benilov, V. Skryshevsky, M. Cabrera, J.-R. Martin, *DNA Bioarrays on Localized Porous Silicon*. in *International Conference "Functional Materials" ICFM-2005*. October 3-8 2005. Crimea, Ukraine
5. A. Benilov., V. Skryshevsky, M. Cabrera, J.-R. Martin, *Matrix DNA Sensors Based on Porous Silicon Localization*. in 3rd *International Conference on Optoelectronic Information Technologies "Photonics-OSD 2005"*. April 26-28, 2005. Vinnytsia, Ukraine
6. A.I.Benilov, A.I.Tsyganova, V.A.Skryshevsky, *Application of eddy current method for NO/NO₂ sensing*. in *Fourth International Young Scientists' Conference on Applied Physics*. June 21-23, 2004. Kyiv, Ukraine

Table of contents

TABLE OF CONTENTS	1
ACRONYMS	5
INTRODUCTION GENERALE	7
GENERAL INTRODUCTION	11
FIRST CHAPTER	15
State of the Art	
1. Porous Silicon	15
2. Porous Silicon Formation	16
2.1. Electrochemical Formation of Porous Silicon	16
2.2. Chemical formation of porous silicon	21
2.3. Porous silicon formation by spark erosion	21
2.4. Local formation of porous silicon	21
3. Properties of porous silicon	22
3.1. Luminescence	22
3.2. Optical properties	24
3.3. Electrical properties	25
4. Porous silicon-based sensors and transducers	26
4.1. Photoluminescence-based transduction	26
4.2. Porous silicon optical transducers	26
4.3. Porous silicon electrical transducers	28
5. Conclusion and objectives	28
SECOND CHAPTER	31
Improvement over Photoluminescence Lifetime Measurement Technique Applicable for Porous Silicon	
1. Introduction	31
2. Time Domain Measurement	32
2.1. Time Correlated Single Photon Counting	33
2.2. Multiple Photons Counting	34
2.3. Analog Mode of Photoluminescence Detection	37
3. Frequency Domain Measurement	38
4. Comparison between the different methods	41
5. PL lifetime measurement setup	42
6. Conclusion	45

THIRD CHAPTER **47****Influence of pH Solution on Photoluminescence of Porous Silicon**

1. Introduction	47
2. Samples and Experiment	48
3. Photoluminescence Measurement	49
4. Sensor protection by PEDOT layer	52
5. Comparison with other sensors	52
6. Conclusions	53

FOURTH CHAPTER **55****Porous Silicon Substrates with Incorporated Catalytic Metal Nanoparticles for Sensors Application**

1. Mechanism of silicon etching at metal doping	55
2. Samples preparation	58
2.1. Ag incorporation	58
2.2. Pt incorporation	58
2.3. Ni incorporation	59
3. Characterization methods	59
3.1. Characterization of porous Si(Ag)-Si	59
3.2. Carachterization of porous Si(Pt)-Si	60
3.3. Characterization of porous Si(Ni)-Si	62
4. Characterization and analysis of Pt-p-Si structures	64
4.1. C-V characterization	64
4.2. I-V characterization	65
4.3. Dielectric constant and thickness estimation	65
5. Conclusion and perspectives	68

FIFTH CHAPTER **69****Overcharging of Porous Silicon Localized States at Gas Adsorption**

1. Introduction	69
2. Principle of DLTS	70
3. Experimental	72
4. Experimental results	73
5. Discussion	76
6. Conclusion	77

SIXTH CHAPTER **79****Application of Eddy Current Method for Silicon / Porous Silicon Conductivity Monitoring**

1. Introduction	79
1.1. Eddy currents	80
1.2. Eddy current based conductivity measurement	81
2. Eddy current based conductometer	82
3. Detection of NO ₂	85
4. Conclusion	86

SEVENTH CHAPTER	87
<hr/>	
Porous Silicon Localization for Implementation in Matrix Biosensors	
1. Introduction	87
2. Principle of porous silicon localization	88
2.1. Electrochemical etching of silicon	88
2.2. Porous silicon localization for p-Si	89
2.3. Porous silicon localization for n-Si	90
2.4. Impact of electric field	91
3. Experimental	91
4. Results and discussion	92
4.1. Profile measurement	92
4.2. Local porosity estimation from contact angle measurement	94
4.3. Optical measurement	95
5. Conclusion	97
EIGHTH CHAPTER	99
<hr/>	
Electrical Discharge Machining of Silicon	
1. Introduction	99
1.1. Spark discharge and erosion	100
1.2. Single electrode EDM	102
1.3. The role of dielectric	103
1.4. Micro and nano EDM	103
1.5. Summary of strategy and objectives	104
2. Development of a μ EDM setup	105
2.1. Preparing of μ EDM electrode	105
2.2. Positioning actuators and mechanical frame	107
2.3. EDM power generator	109
2.4. Discharge control techniques	113
2.4.1. Control by tool-workpiece gap adjustment	114
2.4.2. Control by graduate approaching	115
2.4.3. Digital control of a spark	116
2.5. μ EDM control software	118
2.6. μ EDM metrology	119
3. EDM machining experiments	120
3.1. Cavity with a tip inside	121
3.2. Microchannel with two cavities	125
3.3. Towards the μ EDM	129
4. Porous silicon formation	132
5. Conclusion	134
CONCLUSIONS AND PERSPECTIVES	137
<hr/>	
CONCLUSION ET PERSPECTIVES	141
<hr/>	
ANNEX 1	145
<hr/>	
μ EDM Electronics Schematic	
ANNEX 2	149
<hr/>	
μ EDM Scripting Language	
BIBLIOGRAPHY	153
<hr/>	

Acronyms

AES	Auger electron spectroscopy
AFM	Atomic Force Microscope
CAD/CAM	Computer-aided Design / Computer-aided Manufacturing
CY3	Indodicarbocanine 3
DLTS	Deep Levels Transient Spectroscopy
ECM	Electrochemical Machining
EDM	Electrical Discharge Machining
IGBT	Isolated Gate Bipolar Transistor
ISFET	Ion Selective Field Effect Transistor
FFT	Fast Fourier Transformation
FTIR	Fourier Transformation Infrared (spectrometry or spectrometer)
FWHM	Full Width at Half Maximum
LED	Light Emitting Diode
MCU	Microcontroller Unit
MOS	Metal-Oxide-Semiconductor (technology)
MRR	Material Remove Ratio
PEDOT	Poly (3,4-ethylenedioxythiophene)
PL	Photoluminescence
ppb, ppm	Particles per billion, particles per million
RIE	Reactive Ion Etching
SEM	Scanning Electron Microscope
SERS	Surface Enhanced Raman Scattering
SNR	Signal to Noise Ratio
TCSPC	Time Correlated Single Photon Counting
TTL	Transistor-Transistor Logic
UV	Ultraviolet
WEDM	Wire-EDM
μEDM	Micro Electrical Discharge Machining

Introduction générale

Le développement futur de microsystèmes hétérogènes en silicium monocristallin et en silicium poreux est anticipé pour tirer pleinement profit de chacun des deux matériaux : la compatibilité avec la technologie principale de la microélectronique pour le premier et des propriétés physiques inhabituelles pour le deuxième.

Le silicium poreux fait en effet l'objet d'une attention soutenue en tant que matériau de base pour capteurs à cause de ses propriétés optiques et électriques qui forment une combinaison unique. Le silicium poreux présente une photoluminescence intense dans le domaine visible à température ambiante qui peut atteindre un rendement quantique de 10%. Cette propriété permet d'envisager opportunément le développement d'émetteurs de lumière basé sur le silicium. Le silicium poreux est aussi un matériau semiconducteur à résistance électrique élevée qui peut être modulée à la baisse par des gaz ou des solvants, ce qui est prometteur pour le développement de nouveaux capteurs. Enfin, il présente une surface développée importante, qui peut être mise à profit pour des capacités des biocapteurs, par exemple des puces à ADN ou des puces à protéines.

Malheureusement, le silicium poreux est aussi sujet à une dégradation rapide principalement à cause de son oxydation à l'air ou dans un environnement ouvert (ce qui provoque une chute de la photoluminescence et un changement des propriétés optiques). Ce phénomène contraire empêche le développement de capteurs basés sur le silicium poreux en dépit du potentiel de ce matériau. Pour résoudre ce problème clef, un engagement à long terme de la communauté scientifique sera sans doute nécessaire (à condition que cela s'avère possible). Par ailleurs, bien que le silicium poreux puisse être facilement et rapidement fabriqué avec un équipement simple, le développement de méthodes d'élaboration non basées sur des produits chimiques très réactifs et permettant aussi un contrôle localisé de sa formation, faciliterait son adoption en Microtechnologie.

Cette thèse traite de différents aspects de la technologie du silicium poreux qui incluent les questions liées à la fabrication, à la modification, aux mesures effectuées sur ce matériau, ainsi que des applications pour des capteurs. Notre objectif a été de continuer à explorer le potentiel de matériau en tant que capteur, tout en tentant de trouver des conditions de stabilisation de préparation ou d'utilisation, lorsque cela était possible. Cela inclut notamment le développement de méthodes non conventionnelles d'élaboration (par exemple par décharges électriques comme discuté ci-dessous).

Le mémoire est organisé de la manière suivante. Dans le premier chapitre, nous dressons une vue d'ensemble du silicium poreux. Sont traitées les questions concernant la fabrication de ce matériau et les propriétés utiles pour constituer des capteurs. Nous montrerons les avantages et les inconvénients de ce matériau unique.

Dans les deuxième et troisième chapitres, nous traiterons du développement de capteurs basés sur des mesures de durée de vie de photoluminescence du silicium poreux. Notre objectif était d'évaluer, si des mesures basées sur des propriétés plus intrinsèques au matériau, que des mesures de rendement de fluorescence, pouvaient aboutir à des capteurs plus stables. C'est pourquoi le deuxième chapitre est consacré à différents aspects instrumentaux concernant les mesures d'intensité et de durée de vie de photoluminescence. Ce travail sert de base dans le troisième chapitre à la mise en œuvre du silicium poreux comme capteur de pH dans différentes solutions. Un capteur compact basé sur une DEL est décrit. Des tentatives pour stabiliser le capteur avec un encapsulage en polymère sont aussi incluses dans cette partie.

Le quatrième chapitre traite de l'incorporation de différents métaux catalytiques (Ag et pour la première fois Pt et Ni) dans le silicium poreux afin de créer des matrices semiconductrices avec des nanoclusters métalliques dans les pores. L'objet de ce travail exploratoire était (i) de déterminer si ces nouvelles structures présentaient une photoluminescence et (ii) d'évaluer une utilisation potentielle comme transducteur électrique.

Dans les deux chapitres suivants, nous nous sommes focalisés sur le développement de capteurs de gaz. Notamment, nous présentons dans le cinquième chapitre, une technique de spectroscopie dynamique des niveaux profonds (Deep Level Transient Spectroscopy ou DLTS). L'influence de l'absorption de différents gaz (Ar, N₂, CO₂ et O₂) sur les spectres DLTS d'hétérojonction Si – Si poreux est rapportée. Le sixième chapitre décrit une méthode de mesure sans contact (basée sur des courants de Foucault) pour suivre les changements de conductivité électrique du silicium et du silicium poreux en présence de NO₂.

Le septième chapitre traite de la formation localisée du silicium poreux sur un substrat en silicium. Nous présentons un exemple de structure mixte silicium monocristallin / silicium poreux avec comme application les biopuces. Nous montrons notamment l'élaboration et la gravure de silicium poreux assistée par la lumière. Cette méthode pourrait simplifier l'élaboration de puces à ADN basées sur des substrats en silicium poreux. Malheureusement comme nous le verrons, sa résolution spatiale est limitée par la longueur de diffusion des porteurs de charge, ce qui restreint son champ d'application aux biopuces basse densité (ce qui est toutefois important).

Dans le huitième et dernier chapitre, nous procéderons à un travail exploratoire sur l'usinage localisée du silicium par micro électroérosion (micro electro discharge machining ou μ EDM). Ce chapitre inclut aussi un bref rapport sur la fabrication non conventionnelle de silicium poreux par décharges électriques, qui est un procédé lié à la micro électroérosion. Cette méthode présente en effet un grand intérêt pour préparer du silicium poreux localisé, premièrement parce qu'elle pourrait ne pas être limitée par la longueur de diffusion des porteurs de charge et deuxièmement parce qu'elle n'implique pas l'utilisation de produits chimiques très réactif pouvant causer l'instabilité du matériau. De plus, nous montrons aussi que la micro électroérosion présente en soi un très grand intérêt pour la fabrication de dispositifs basés sur du silicium pour des applications variées (microfluidiques, capteurs, micromoules pour l'injection de polymère, etc.) Le développement de l'instrument décrit dans ce chapitre permettra notamment d'étudier la transition entre érosion et porosification par microdécharges, ce qui est un sujet relativement vierge à notre connaissance.

Ce mémoire comporte aussi deux annexes. Les deux concernent le banc de microélectroérosion (partie matérielle et le logiciel). L'Annexe 1 donne les schémas électroniques de l'instrument. L'annexe 2 décrit le langage logiciel développé pour contrôler le dispositif expérimental.

General Introduction

It is conceivable that in the future, heterogeneous microdevices made of standard crystalline silicon and porous silicon may allow taking full advantages of both materials: compatibility with the main stream microelectronics technology for the former and unusual physical properties for the latter.

Porous silicon has attracted indeed a great deal of attention as a material for sensors because of a combination of a set of unique optical and electrical properties. Porous silicon manifests an intense visible photoluminescence at room temperature that can achieve up to 10% in quantum efficiency. This phenomenon gives an important opportunity to develop silicon based light emitters. It is also a semiconductor material that has a high electrical resistance that can be decreased in presence of some gases and solvents, which is promising for the development of new sensors. Lastly, it manifests a high developed surface that is quite favorable for sensors and biosensors (e.g. DNA chips and biochips).

Unfortunately, porous silicon is also subjected to fast degradation mainly due to oxidation in open air or in aqueous environment (that particularly leads to photoluminescence dying and optical properties change). This negative occurrence impedes greatly the development of porous silicon based sensors in spite of all capabilities of this material. To solve this issue will probably request the long term commitment of the scientific community (if possible at all). Although porous silicon can be easily and quickly prepared by simple equipment, the development of ways of implementation not based on strong chemical and allowing also local control of properties, may facilitate a wider acceptance in microtechnology.

This thesis deals with various aspects of porous silicon technology that includes the questions of fabrication, modification, measurement, and application in sensor devices. Our

goal was to continue to explore the potential of porous silicon as a sensing system, trying to find stabilizing conditions of preparation or use when it was possible. This includes the development of non conventional preparation technique (e.g. spark erosion as discussed below).

This memory is organized the following manner. In the first chapter we give a general view on porous silicon. The aspects of porous silicon formation and its capabilities to be used as a material for sensors will be reviewed. We will also discuss some advantages and drawbacks of this unique material.

In the second and third chapter, we report the development of sensors based on the lifetime measurement of porous silicon fluorescence. Our goal was to evaluate if measurements based on more intrinsic properties than classical fluorescence yield could leave to more stable sensors. Therefore, the second chapter is devoted to the instrumental aspects of porous silicon photoluminescence intensity and decay time measurements. This work is applied in the third chapter to the use of porous silicon to detect different pH solutions. A LED based compact sensor is described. An attempt to stabilize the sensor with a covering polymer is reported.

Chapter four deals with the incorporation of different catalytic metals (Ag and for the first time Pt and Ni) into porous silicon. This may be used to create semiconductor matrices with metallic nanoclusters in the pores. In this exploratory work, our goal was (i) to determine if these new structures show some photoluminescence and (ii) to evaluate their potential for electrical transducers.

In the following two chapters, we focus on the development of gas sensing systems. Notably in the fifth chapter, the deep level transient spectroscopy (DLTS) study of porous silicon is presented. The influence of absorbance of different gases (Ar, N₂, CO₂, and O₂) on DLTS spectra of Si-porous Si heterojunction is reported. Chapter six describes a contactless conductivity measurement method implementation based on eddy current to monitor Si and porous Si conductivity changes in presence of NO₂.

Chapter seven deals with the formation of porous silicon locally on a silicon substrate. We present an example of mixed monocrystalline / porous silicon structure in the field of biochips. The implementation of light-assisted etching of porous silicon is considered. This method could greatly simplify the fabrication of biochip based substrates with localized porous silicon. Unfortunately as we shall see, its spatial resolution is limited by the diffusion of free carriers, which restraint this technology to the important but limited field of low density biochips.

In the last eighth chapter we perform an exploratory work on the local machining of silicon by micro electro discharge machining (μ EDM). This chapter includes also a brief report on the non conventional preparation of porous silicon by electrical spark processing, which is closely related to μ EDM. This method may be indeed of high interest to prepare localized porous silicon because firstly, it may be not limited by free carriers diffusion and secondly, because it does not involve strong chemicals leading to material instabilities. Moreover, we report also that μ EDM is by itself of high interest for the fabrication of silicon-based devices for various implementations (microfluidic, sensors, micromold for polymer injection etc.) The development of the instrument described in this chapter, will allow the analysis of the frontier between silicon erosion and porosification by spark processing, which is a relatively new subject to our knowledge.

There are two annexes attached to this thesis. Both of them concern the μ EDM setup hardware and software implementation. Annex 1 gives a full schematic of the electronics of the μ EDM setup. Annex 2 describes a scripting language developed to control the μ EDM setup.

First Chapter

State of the Art

This chapter gives a general introduction on porous silicon pointing to the increased interest to this material. Porous silicon possesses many unique properties, which give a chance for wide implementation of this material in different domains, such as chemical and biological sensors and optical devices. Particularly porous silicon was investigated in our work as an electrical and optical transducer for constructing chemical sensing systems.

1. Porous Silicon

For the first time porous silicon was created in the year 1956 by anodic (electrochemical) etching of crystalline silicon wafers in water-ethanol solution of hydrofluoric acid (HF) [1, 2]. It was found that such kind of treatment of crystalline silicon can produce a porous material: sponge-like structures, micro-columns, nano-wires or nanocrystallites. These nanocrystallites can be easily oxidized in ambient air. The size of pores formed during anodization process depends on silicon wafer doping level, etching mode (etching time and anodization current), and illumination conditions of the sample. According to the pores size, porous silicon can fall into one of the following categories: *nanoporous* silicon (pores diameter < 4 nm), *mesoporous* silicon (pores diameter is in range of 4—50 nm), and *macroporous* silicon (pores diameter is > 50 nm).

Porous silicon has semiconductor properties. However, its resistivity is very high (order of 10^4 — 10^8 $\Omega\cdot\text{cm}$), due to low concentration of free carriers and its low mobility

(10^{-3} — $4.0 \text{ cm}^2/\text{V}$) [3]. Diminution of nanocrystallites size leads to an increase of forbidden gap that can vary in porous silicon within the range 1.4 — 3.0 eV [4-6].

For a long period of time, porous silicon was applied for SOI (silicon on insulator) technology, where porous silicon layer was additionally annealed in oxygen atmosphere to produce a porous silicon oxide further used as a substrate for Si epitaxy [7]. But after the discovering by Canham in 1990 of an intense visible luminescence at room temperature [8], porous silicon attracted an enormous attention of researchers wishing to implement silicon optoelectronic devices and different kind of sensors. Such an interest is caused by the possibility to transform crystalline silicon to nanocrystalline material that can manifest optical transitions. The other important point is the creation of silicon LEDs according to a process compatible with existing MOS technology.

Porous silicon is composed of a silicon skeleton permeated by a network of pores. In general case, the distribution of pores and its size in the porous Si layer is uniform, so a macro-parameter is introduced to characterize the porous Si—porosity, which can be defined as follows [9]:

$$P = \frac{V_{pores}}{V_{pores} + V_{Si}} \quad (1.1)$$

Where V_{pores} is the total volume of pores, and V_{Si} is the volume of residual silicon.

Experimentally the porosity of porous silicon is usually estimated by mass measures before etching and just after it, or by optical methods (porous silicon layer thickness and refractive index measurement). The effective surface of porous silicon is enormously large and can reach a value of several hundreds of m^2 per cm^{-3} [10], which is one reason for the interest of implementing this material in sensor devices.

2. Porous Silicon Formation

Most often, porous silicon can be produced by electrochemical dissolution of silicon crystal in HF-based solution. Additionally, other ways can be used, such as chemical etching [11], spark erosion [12] or laser ablation [13]. The porous silicon samples described in this thesis were fabricated mostly by electrochemical anodization of silicon in a hydrofluoric acid (HF) based electrolyte.

2.1. Electrochemical Formation of Porous Silicon

The typical cell for silicon electrochemical etching is shown in Figure 1.1 which was used in our experiments. Positive potential is applied on silicon wafer (anode) immersed in water-alcohol solution of hydrofluoric acid; counter electrode has negative potential

correspondingly [9, 14-17]. As far as silicon manifests insufficient wettability contacting with water/HF, an alcohol is used to improve it (usually ethanol or propanol) to produce a uniformly etched porous silicon layer.

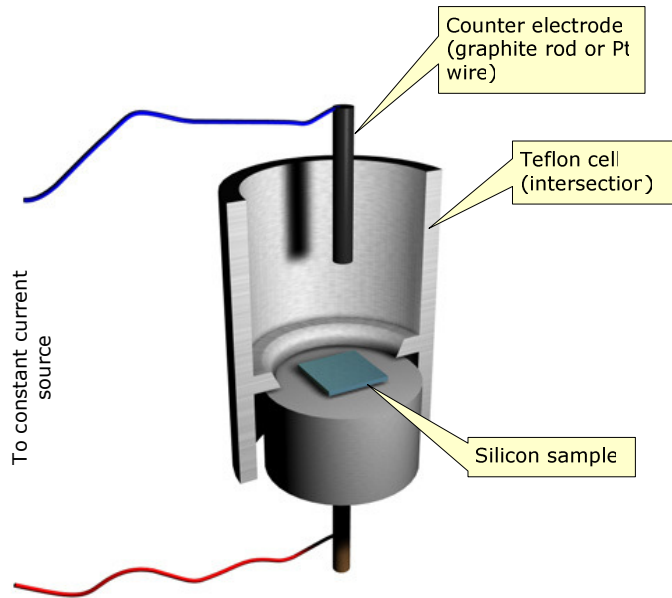


Figure 1.1

Anodization cell (shown in section) for electrochemical porous silicon formation.

Usually, the definition of the area of the wafer to be porosified by HF is performed with mechanical separation (for example by ‘O-ring’ or varnish). Sometimes a supplementary illumination can be required for porous Si formation (especially on n-doped wafers). In this case, the sample can be illuminated from the top of the etching cell (via the etching solution) or special cell geometry (double-tank, for instance) can also be used to produce a back side illumination of the sample during anodization process [18, 19]. Most often, simple electrochemical etching is used to produce nano- and meso- porous silicon films on silicon substrates. Macroporous silicon is usually produced on n-doped silicon wafers previously patterned by standard photolithography; these wafers are further etched under anodic bias and backlight illumination (in order to generate holes in n-doped Si) in hydrofluoric acid based solution [20].

Electrochemical porous silicon formation process is well studied, however, several models have been developed successfully to describe the process [9, 14, 21-23]. Among all these models they distinguish the main three of them [15, 24, 25]. However that may be, all these models claims that holes play a leading role in porous silicon formation. It is also claimed that each hole supplied by bulk and reaching the surface acts in the dissolution reaction of silicon [16].

The first model usually mentioned is a quantum-mechanical model of pores formation. This model claims that dimensional quantization due to Si crystallites size

diminution leads to widening of the forbidden band and formation of energy barriers between the substrate and silicon nanocrystallites of already formed porous Si. This energy barrier impedes the transition of holes from silicon substrate to nanocrystallites area (which is depleted of holes).

The second important model — the diffusion limited model — considers that the growth of pores is defined by the holes diffusion through the depleted region towards active nodes of silicon surface, where these holes participates in the process of silicon dissolution.

Finally, the third model describes the growth of pores based upon electric fields distribution and voltage applied between the Helmholtz layer in electrolyte and space-charge region in silicon, thus the pores growth is determined by the properties of electrolyte-silicon interface.

Porous silicon is formed at relatively small potentials (0.5—5 V) and currents (10—400 mA/cm²) applied between the reference electrode and silicon wafer. Thus, pores grow at condition when the process of silicon dissolution is limited by how fast holes reach the surface [15]. In most cases, a constant current source is used to bias the sample during the etching. Actually, the formation of porous Si layer influences greatly the conductivity of the whole circuit (counter electrode — electrolyte — porous Si — Si — anode) as far as porous Si possesses very low conductivity. To avoid this influence, a constant current flow should be implemented to produce a homogeneous porous Si layer. A good electric contact between the wafer and the anodic electrode is also important to obtain homogeneous layers of porous Si. So the contact is usually made using the entire back surface metallization of the wafer. This prevents lateral potential variation across the wafer that would cause changes in the local current density.

A simple scheme of processes which takes place on the silicon surface, can be described as follows (Figure 1.2). More precise model also includes the participation of H₂O molecules at silicon etching (in order to dissolve one atom of silicon it is necessary to bring to the surface two holes and one molecule of H₂O) [15, 26-29]. The model, proposed by Lehmann and Gösele also explains the emission of hydrogen bubbles during the silicon etching [21].

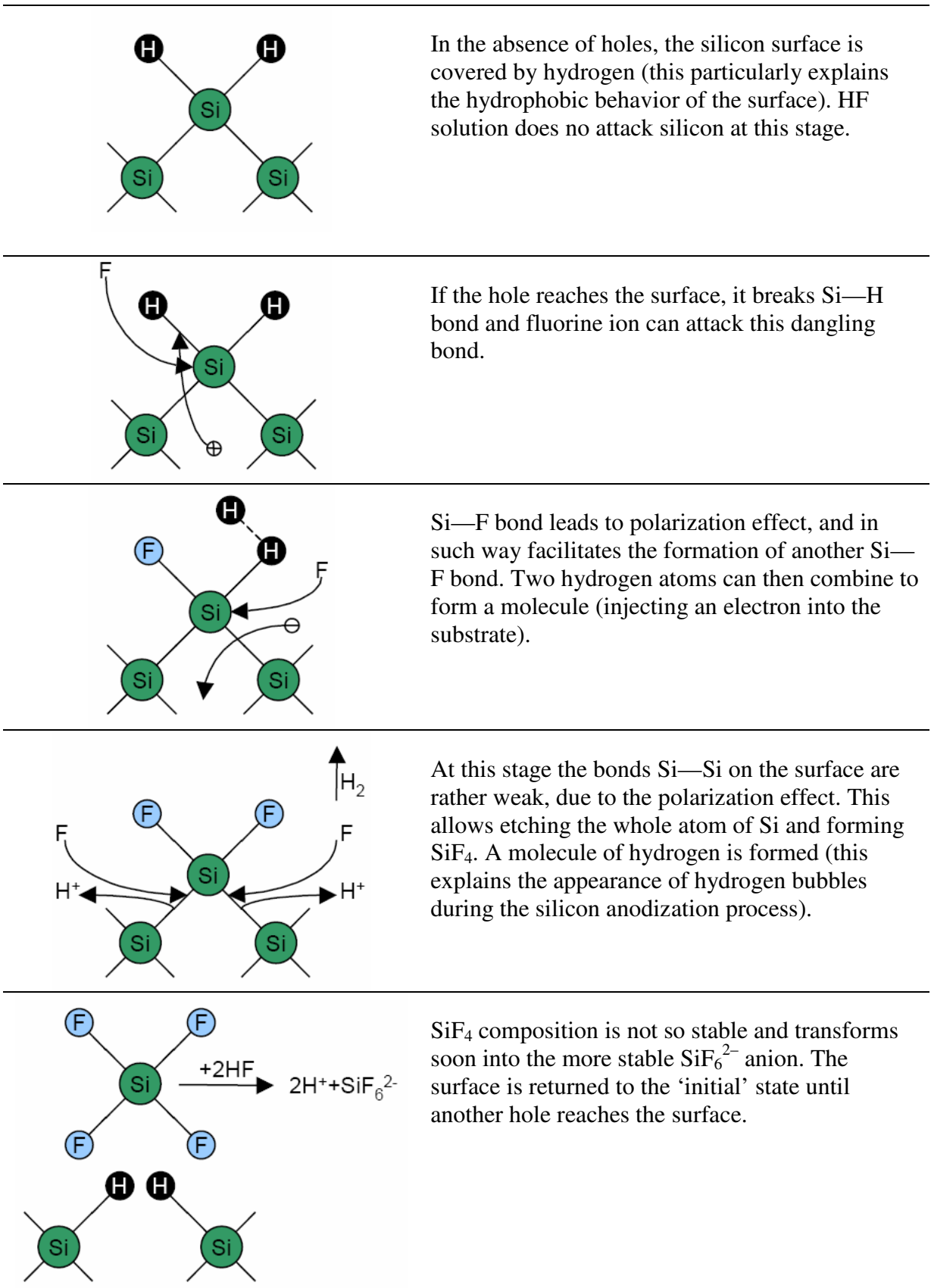


Figure 1.2 Electrochemical etching of silicon by HF [18].

Porous Si pores size, silicon nanocrystallites dimension, and growth rate can be easily controlled by varying anodization conditions (HF concentration and anodization

current). On the surface of porous Si, the nanocrystallites can be as small as 2.0—2.5 nm. Smaller crystallites are found to be not stable mechanically [24]. The etching rate of silicon crystal and the porosity of porous silicon formed depend also on the doping level of the silicon wafer (Figure 1.3, Figure 1.4).

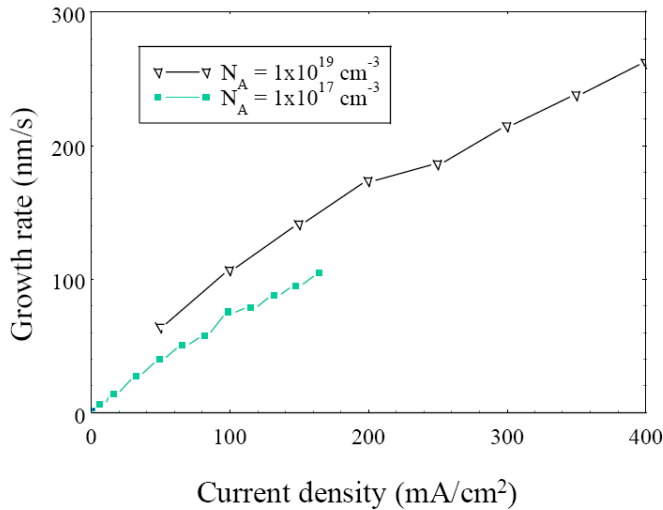


Figure 1.3

Porous silicon growth rate as a function of current density for low-doped ($N_A=10^{17} \text{ cm}^{-3}$) and high-doped ($N_A=10^{19} \text{ cm}^{-3}$) p-type silicon [18].

For strong anodization current densities, the porous silicon formation turns into electropolishing process. Since the anodization process does not affect the porous Si already formed, high current density can be also used to produce free-standing porous silicon films and membranes [30, 31].

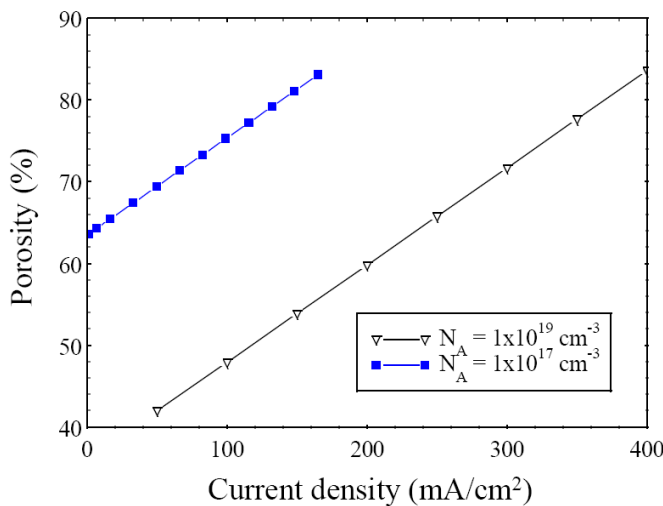


Figure 1.4

Porous silicon porosity as a function of anodization current density for low-doped ($N_A=10^{17} \text{ cm}^{-3}$) and high-doped ($N_A=10^{19} \text{ cm}^{-3}$) p-type silicon [18].

Highly doped silicon allows varying the porosity of porous Si in wide ranges, in comparison to a moderately doped one (Figure 1.4). So, for optical applications, where a wide range of porosities is required, most often highly doped silicon slabs are used (usually p-doped), paragraph 4.2 will give more details [32, 33].

2.2. Chemical formation of porous silicon

Alternatively, porous silicon can also be formed by etching in HF:HNO₃ water solution. This process is usually referred as stain etching [11, 34, 35]. During the stain etching, HNO₃ acid oxidizes the surface of silicon. Silicon oxide can then be easily etched by HF. These reactions are carried out without application of any supplementary current or voltage, so the properties of the porous silicon formed can be adjusted only by choosing different concentrations of HNO₃ and HF in water solution [35, 36]. Porous silicon fabricated by the stain etching method is inhomogeneous in both porosity and thickness due to the intense hydrogen bubbles formation, which remains on the surface of the wafer during the etching process. Porous Si near-surface layer dissolution in HF:HNO₃ solution also increases the inhomogeneity of porous Si formed by stain etching [36].

2.3. Porous silicon formation by spark erosion

In 1992 R. Hummel showed that porous silicon can be prepared in air or in a dry nitrogen atmosphere, utilizing a spark-erosion technique [12, 37]. The principal of this method consists in the formation of an electrical spark between the silicon surface and a reference electrode. This technique does not involve aqueous solutions or fluorine contaminants; however the samples prepared yield similar photoluminescence spectra as those obtained by anodic etching in HF or chemical etching in HF:HNO₃ solution. However, with this method the wafer is exposed to the sparks during several hours under a high voltage (15 kV). The spark processing can be performed in air or in inert gas at room temperature.

It was also shown that the energy put into the spark discharge defines the size of pores [38]. Actually the pores are formed by the silicon material evaporation, induced by spark impact. This phenomenon actually pushed us to the idea of spark-processing of silicon, which will be described in the chapter 8 of this thesis.

2.4. Local formation of porous silicon

In most applications of porous silicon in optical (waveguides and photonic structures), micromechanical, and sensor systems, it is necessary to form locally the porous material on top of the bulk of crystalline silicon. Usually, different masking materials are used to provide a localized Si surface protection against the etching solution. These include silicon nitride [39] or simple photoresist layer [40]. There are some difficulties to apply standard photolithographic resins for the localization of porous silicon, since this implies the development and the removal of photoresist, that usually involves polymer etching in alkaline solution which etches also the porous silicon [41]. Different modifications of the lithographic process, such as additional steps of thermal annealing [40], can make these resins compatible

with porous silicon localization. However, durational etching and photoresist removal is not allowed in this case anyway.

As explained above, a single layer resist mask is not appropriate for deep etching process, light assisted etching can be applied to produce localized porous silicon on n-doped silicon wafers [42]. This method is based on the principle that n-Si etching takes place only in case of external excitation for holes generation. This method of porous silicon localization is quite interesting, since it does not require additional lithographic steps for but just a localized illumination, however it is applicable mostly to n-doped silicon slabs (whereas the photosensitivity of p-doped Si — HF electrolyte interface has been also shown [43]). We will try to study and develop this method in the seventh chapter of this thesis.

Ion implantation technique to change locally the conductivity type of silicon has also been reported [44-46]. In this case local n-doped areas on p-doped silicon act as a pattern mask that defines the regions of etching (as it was mentioned above, HF etching solution does not touch n-doped Si since it is holes depleted). Conversely, positive ions can be implanted into n-doped slabs to produce localized p-doped regions etched by HF solution [47]. However, this method creates barrier layers (like pn-junctions), which are sometimes undesirable.

3. Properties of porous silicon

3.1. Luminescence

As mentioned above, porous silicon layers produced by electrochemical etching of silicon slabs (1—10 Ω -cm) can manifest an intense visible luminescence at room temperature [48]. Stain etched porous Si manifest similar luminescent properties. It was reported that the photoluminescence mechanisms involved in both cases seem to be the same [49].

Considering porous silicon luminescence emission spectrum, two typical spectral peaks can be distinguished: the first one is approximately at 400 nm of wavelength having 10 ns decay time (fast band, usually referred as F-band), and the second one is at 500—800 nm (Figure 1.6, e) having decay time of 50 ns—10 μ s at room temperature (slow band, usually referred as S-band). The F-band is observed only in oxidized porous Si, and it is probably originated from contaminated or defective Si oxide [9, 50, 51]. Annealing in water vapor activates the blue emission indicating a possible major role of adsorbed hydroxyls in the emission process. The origin of the F-band can be explained by recombination in small nanocrystals that have wide bandgap, whereas the S-band originates when an exciton (created by external excitation) moves towards the surface or interface and recombines in large crystals with narrow bandgap, correspondingly (Figure 1.5).

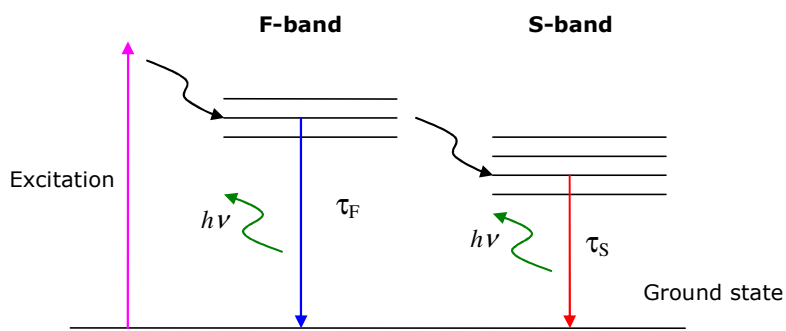


Figure 1.5

Porous silicon photoluminescence energy diagram.

Usually, the effective quantum efficiency of photoluminescence of the S-band is higher comparing to the F-band and can reach 10%. Even today, the physical mechanisms of porous silicon visible luminescence are subject of constant discussion. Many researchers draw out the theory of quantum confinement effect in silicon nanocrystals [52, 53]. However there are a lot of experimental data for the evidence of surface groups and defects existence, which can be also a cause of luminescent phenomenon or have an influence on quantum efficiency of the luminescence.

Alternatively other models of porous silicon luminescence can be also considered:

- Emission from hydrogenated amorphous silicon or other hydrogen groups SiH_x which cover the surface of porous silicon just after its formation by anodization process in HF based solution.
- Luminescence from other molecular groups (like, siloxen $\text{Si}_6\text{O}_3\text{H}_6$, or SiO_x defective complexes), which can be formed on porous silicon surface during anodization.
- Radiative recombination of charge carriers through localized states of developed porous silicon surface.
- Radiative recombination of charge carriers localized on volume defects of porous silicon or on oxide film which usually covers the surface of porous silicon.

Spark-erosion process, which leads to the formation of silicon nanoclusters, also manifests a visible photoluminescence [54, 55] and electroluminescence [56]. Due to the nature of the preparation technique, PL spectrum of spark eroded porous silicon samples are usually shifted to the blue region (410—550 nm, Figure 1.6 a—d) [37, 57-59].

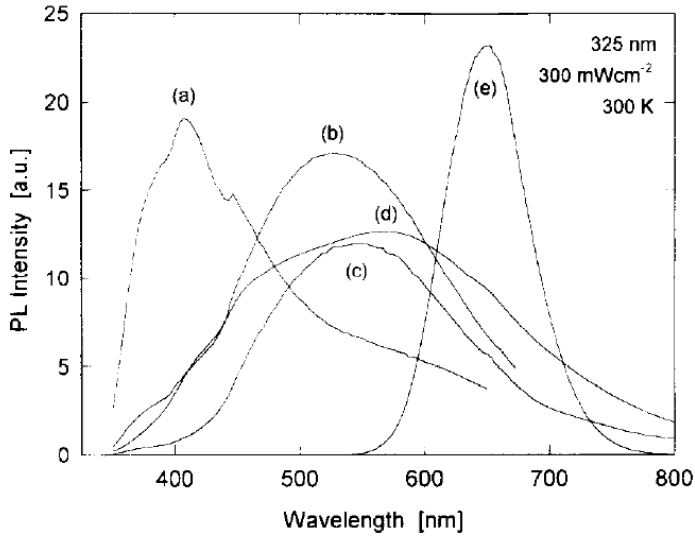


Figure 1.6

Typical room-temperature PL spectra of spark-eroded porous silicon in different environment (excited at 325 nm):
a) flowing of compressed air;
b) stagnant air;
c) pure nitrogen;
d) CO₂ atmosphere;
e) porous silicon produced by classical anodic etching process.
(This figure is taken from [60]).

The PL intensity of spark-eroded silicon remains relatively stable under UV illumination, whereas the PL intensity of conventional HF-etched porous Si decreases substantially under these conditions due to the hydrogen loss [58]. However, the PL spectrum maximum of spark-eroded porous Si is shifted correspondingly by shifting the excitation wavelength that indicates the inhomogeneity of porous Si layers produced by the spark erosion process. This was originally the major reason for us to investigate spark erosion.

3.2. Optical properties

Besides its visible luminescence, porous silicon manifests other interesting optical properties. The variations of porosity value actually correspond to the variations of refractive index and transmission spectrum of the material. The effective index of refraction for the heterogeneous material in case of macroscopic particles (diameter of which is much smaller of wavelength, $d \ll \lambda$) can be estimated according to the Bruggeman effective environment approximation [24]. In this approximation, porous Si is considered as a 3D isotropic mixture of silicon and whatever is inside the pores [33]:

$$P \left(\frac{\hat{\epsilon}_e - \hat{\epsilon}}{\hat{\epsilon}_e + 2\hat{\epsilon}} \right) + (1 - P) \left(\frac{\hat{\epsilon}_{Si} - \hat{\epsilon}}{\hat{\epsilon}_{Si} + 2\hat{\epsilon}} \right) = 0 \quad (1.2)$$

where P is the porous Si porosity, $\hat{n} = \sqrt{\hat{\epsilon}}$ and $\hat{\epsilon} = \epsilon_r + i\epsilon_i$ are the complex refractive index and complex permittivity of porous Si, $\hat{\epsilon}_{Si}$ and $\hat{\epsilon}_e$ correspond to the permittivities of silicon and the environment (inside the pores).

As far as it is not so difficult to vary the porosity (by changing of anodization current during porous Si formation process) it is possible to create a layer of porous silicon with defined refractive index and thickness or even multilayer structures, such as Bragg mirrors and microcavities [20, 61, 62]. Usually, a highly-doped p-type Si (p^+ -Si) is used to

fabricate these optical devices, as far as p⁺-Si allows wide variation of its porosity, and yet its refractive index (Figure 1.4, Figure 1.7).

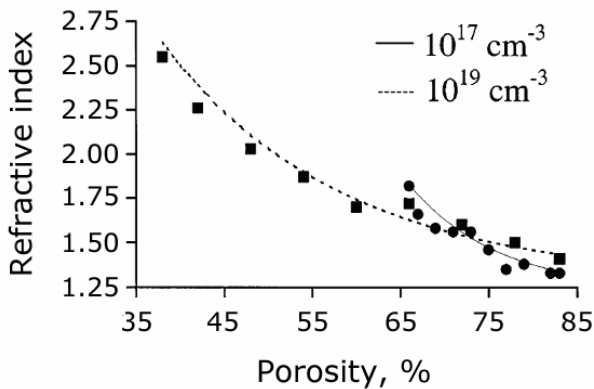


Figure 1.7

Porous silicon refractive index as a function of porosity of p-doped Si with different concentration of dopant [63].

3.3. Electrical properties

Nanoporous and mesoporous silicon are depleted of free charge carriers [21, 64, 65], which explain the very low electrical conductivity of porous layer (10^{-7} — $10^{-4} \Omega^{-1}\text{cm}^{-1}$). Electrical conductivity and PL properties of porous silicon are strongly correlated: highly luminescent porous silicon at room temperature has low value of conductivity, becoming insulating-like for the most luminescent samples [65, 66]. It was shown, however, that the presence of free charge carriers can be restored at absorption of certain gases (particularly NO and NO₂) [64, 67-69] and solvents [70, 71]. Figure 1.8 represents the dependence of free carriers concentration on NO₂ pressure.

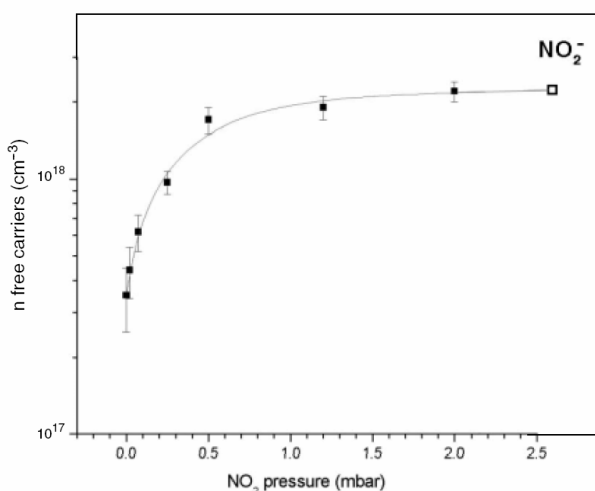


Figure 1.8

The dependence of free carriers density in porous Si layer versus the NO₂ partial pressure estimated by IR spectra. This figure is taken from [64].

The changes of free carriers concentration can be monitored by FTIR studies [71] or directly by passing a current through the porous Si layer. There is no reliable explanation of the origin of the influence of adsorbed substance on porous silicon conductivity. However, it can be assumed that as far as porous silicon is composed of small loosely connected crystallites, the electronic transport in such a structure is limited by energy barriers between

the particles, then adsorbates might lower these barriers, thus enhancing the conductivity [66]. NO₂ molecules adsorption leads to holes injection to the porous layer that leads to the increase of conductivity.

4. Porous silicon-based sensors and transducers

Porous silicon has attracted much attention as a new optoelectronic material since the first observation of its efficient photoluminescence at room temperature. As far as porous surface is very developed [72], any modification of the surface can influence different properties of porous silicon (mechanical, electrical and optical). Owing to this fact, porous silicon was claimed to be a promising material for implementation in various sensing devices. Chemical sensors based on porous Si display some advantages when compared with other transducers: low cost of product, possibility of improved performance due to its optical properties. The investigation of porous silicon luminescence and its optical and electrical properties is being carried out in many laboratories.

4.1. Photoluminescence-based transduction

It has been observed by many researchers that the photoluminescence of porous silicon is quenched upon exposure to certain solvents and gases. The PL intensity drops by three orders of magnitude when porous Si is immersed in organic solvent of dielectric constant varying from 2 to 20 [73]. The PL quenching increases with the dipole momentum of adsorbed molecules [73-79]. Photoluminescence quenching effect can be provoked by binding of the gas or vapor molecules to the silicon nanocrystallites, which introduces the way for non-radiative recombination. This effect is widely used to create different kind of gas or vapor sensors using porous silicon as photoluminescent transducer [75, 76, 80].

The high sensitivity of porous Si PL to different environment is explained by nonradiative recombination pathways (surface states trapping, interfacial energy transfer, and interfacial charge transfer) that are directly connected to the chemical environment around the Si skeleton. The nonradiative processes occur in parallel with the radiative ones, so there is a competition between these processes [17].

It was reported, however, that PL of porous Si is not stable and degrades under UV illumination due to the photooxidation effect [81-83]. This phenomenon limits greatly the lifetime of porous Si photoluminescent sensors.

4.2. Porous silicon optical transducers

Even a single thin porous silicon layer manifests sharp spectral fringes that can be measured by reflective spectrometry or ellipsometry. Interference on a single homogeneous

layer of porous Si gives maximal reflection for the cophased waves reflected from the top interface and the bottom interface of this porous layer (Figure 1.9).

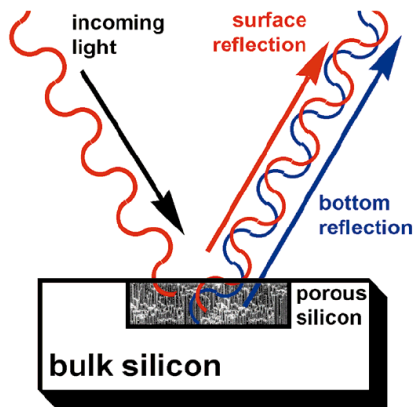


Figure 1.9

A schematic view of optical interference on a single layer of porous silicon [80].

For a normal incidence of incoming light, the maxima will appear at the following wavelength of reflectance spectrum (1.3):

$$\lambda_{\max}(k) = \frac{2nd}{k}, \quad k \in \mathbb{N} \quad (1.3)$$

where n is refractive index of porous Si layer and d is its thickness.

At adsorption of a substance inside the pores, the refractive index n of the porous silicon layer is changed according to the permittivity of the adsorbed matter (formula (1.2)).

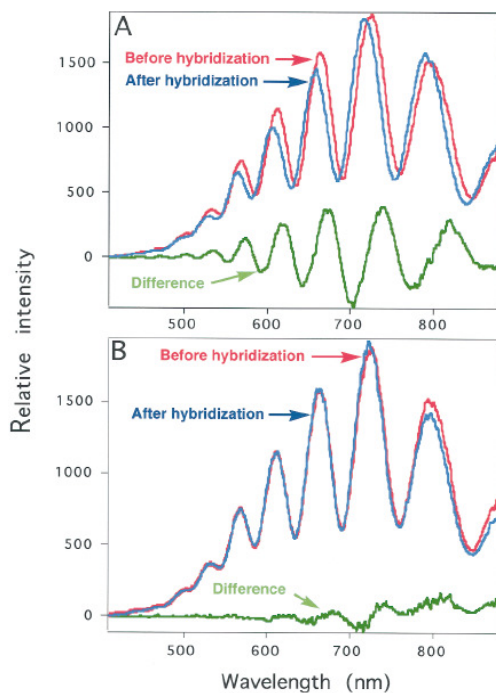


Figure 1.10

Interferometric reflectance spectra of DNA-modified porous Si layers.

Figure A shows the Fabry-Perot fringes for complementary DNA sequences.

Figure B shows the control experiment of exposition of the sensor to non-complementary DNA sequences.

These figures are taken from [84].

Obviously, any changes of porous Si layer refractive index lead to interference fringes displacement. Particularly this phenomenon was used to detect non-labeled DNA hybridization (Figure 1.10) [84, 85] or other bimolecular interaction [86] and also the presence of different vapors [87-89] and solvents [90]. The use of multilayer optical structures,

such as Bragg reflectors and resonators can make the interference even sharper, which increases the resolution of such transducers [91-94].

However the instability of porous Si layers (mainly due to oxidation) affects dramatically its optical properties. Thus, such transducers are not yet very popular.

4.3. Porous silicon electrical transducers

The phenomenon of conductivity increase in presence of certain adsorbates gave an opportunity to create a sensitive and cheap sensor based on porous silicon. The Figure 1.11 represents a feedback of such a NO₂ sensor composed of a single porous silicon layer grown on silicon substrate with golden electrodes deposited on it by evaporation [67]. A Voltage is applied between these golden electrodes and the current flow through the porous Si layer is monitored. This type of sensors allows detecting NO₂ concentrations as low as 10 ppb, whereas the permissible concentration of this gas in air is 3 ppm [24].

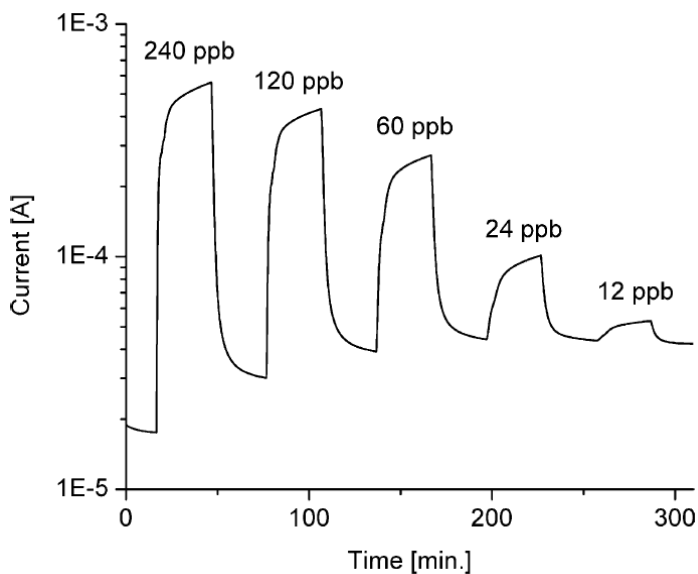


Figure 1.11

Dynamic response of simple conductivity sensor to different concentrations of NO₂ in dry air. This figure is taken from [67].

Porous silicon based structures are also used for capacitive or potentiometric measurements [95-100]. In devices of this type, this material is used mainly to increase the active surface area and in such way to ameliorate the sensor sensitivity [101].

5. Conclusion and objectives

As one can see, porous silicon possesses a set of unique optical and electrical properties, which allow creating of different kinds of transducers (optical and electrical). The very important property of porous silicon is its developed surface and a high sensitivity under adsorption. However, this fact has also a negative side: fast porous silicon surface degradation, which is caused by the influence of adsorbed substance as well as by storage of samples under

normal conditions. Several approaches were proposed to stabilize the material properties [102, 103], however none of them does not allows completely avoiding porous Si degradation.

The porous silicon formation itself is quite a primitive process which on the one hand prepossesses by the simplicity of porous silicon material obtaining, but on the other hand imposes some difficulties in the integration in current microelectronic technologies (as far as porous silicon formation usually requires strong reagents like HF or HNO₃ acids and is not compatible with habitual photolithography).

In this connection we can mark the actual problems of porous silicon technology to be overcome:

- The modification of photolithographic approaches to be applied for the localized porous silicon formation, or development of alternative methods which do not involve strong etching chemicals and/or photolithographic steps;
- Stabilization of the porous silicon surface, which is important to implement porous silicon in various chemical sensors;
- Development of new type of transducers avoiding the drawbacks mentioned above or diminishing its influence on the signal output;
- Development and implementation of new technologies for porous silicon based devices and measurement system fabrication.

We will deal with these problems in our research work, from the physical point of view as well as considering pragmatically the questions related to the instrumentation and realization of full-fledged operational sensing systems based on porous silicon using its optical and electrical properties. In our work we want to study the photoluminescence of porous Si (and especially the degradation process) in order to find some possible ways of its stabilization. We will also concert some aspects of improvement of existing sensors, based on porous Si that includes the problems of fabrication (local formation), sensitivity, and stability increase by surface modification and measurement techniques.

Second Chapter

Improvement over Photoluminescence Lifetime Measurement Technique Applicable for Porous Silicon

In this chapter we describe and compare different methods of photoluminescence lifetime or decay time measurement. Time domain and frequency domain methods of lifetime estimation are examined. Several adjustments to the classical measurement approaches are proposed and considered in details. The modified methods were successfully implemented for porous silicon photoluminescence (PL) lifetime measurement. The proposed modified schemes of photoluminescence decay time measurement allow the construction of sensitive and low-cost measurement systems to study the PL kinetics of nanocrystalline semiconductors having a wide dynamic range of PL lifetime and intensity. The material of this chapter was published in [104].

1. Introduction

Photoluminescence (PL) is a fundamental process in which a substance absorbs a photon, leading to an excitation to a higher electronic energy state, followed by an emission of a photon back out, with a transition back to a lower energy state. PL is defined like an excess over heat radiation. This excess radiation has a finite duration, which significantly exceeds the period of light oscillations. This definition distinguishes luminescence from equilibrium heat radiation and from any other types of nonequilibrium radiations, which are practically noninertial (its duration comes to the period of light oscillations, i.e. 10^{-15} seconds). For the

luminescence process, the phenomena of absorption and radiation are divided by intermediate processes, that is why the radiation can exist for a long time even after the excitation. The scale time of the emission can vary in a wide range. For instance, fluorescence can occur during excitation, i.e. in nanosecond time range, while phosphorescence can last for hours or even days. Fast and slow components of luminescence often exist simultaneously, for organic molecules and nanocrystalline semiconductors, for example. That is why an important task is the accurate measurement of the quantum efficiency and the kinetics of the luminescence. [105].

In the present work, we are focused on several techniques of PL lifetime estimation which allow constructing a sensing system with both PL intensity and lifetime detection using porous silicon as an object of investigation. The PL of porous silicon manifests large dynamic ranges of intensity (up to 10% of quantum efficiency) and lifetime (from nanoseconds to microseconds and even milliseconds at low temperatures). Thus, the development of improved PL measurement techniques is quite a problem of current importance for a good adaptation of the instrumentation to this material.

2. Time Domain Measurement

A straightforward approach for PL lifetime estimation is a time domain measurement. After the excitation of a fluorescent material by a short-time light pulse, a photoluminescence response is detected during a fixed timeframe. Assuming the excitation pulse being a $\delta(t)$ function, the luminescence response can be considered as the pulse response of the luminescent material (Figure 2.1).

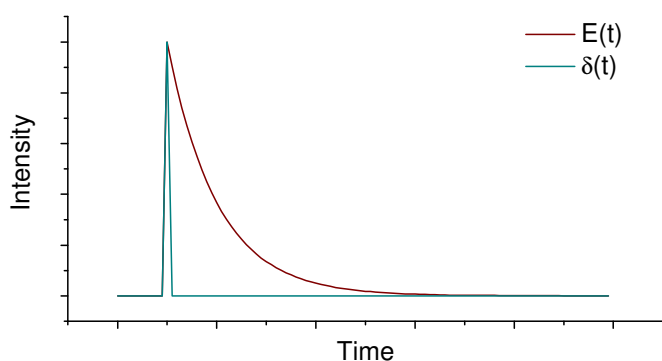


Figure 2.1

Narrow pulse excitation $\delta(t)$
and system pulse response
 $E(t)$

In practice the luminescence response read out (i.e. the signal that we actually measure) has to be written as the convolution of the real excitation signal (which is not a δ function in general sense) with the pulse response function of the luminescent system:

$$S(t) = \int_{-\infty}^{\infty} E(t-t') \cdot I(t') dt' \quad (2.1)$$

where $I(t)$ is the excitation pulse function, $E(t)$ is the luminescent material pulse response function as a convolution kernel, and $S(t)$ is the signal detected with the measurement setup.

2.1. Time Correlated Single Photon Counting

In practice the luminescence signal should be accumulated over several excitation pulses to determine the statistics of photons emission. The time correlated single photon counting (TCSPC) [106, 107] is known to be the most accurate and sensitive technique of luminescence decay estimation. It is based on single photon capturing within a timeframe after the excitation pulse passed and measuring the time between the excitation pulse and photon detection. As far as the probability of photon capturing at time t is directly related with the photoluminescence intensity $S(t)$, the perfect reconstruction of photoluminescence emitting signal is possible by gathering of statistics on emitted photons captured.

The Figure 2.2 depicts the basic TCSPC implementation scheme. The `start` signal triggers the excitation source and also launches the high-frequency oscillator for time measurement. When a photon is captured, the oscillator is stopped (`stop` signal). Thus, the number of oscillations can be directly converted to the time passed between `start` and `stop` signal by using, for example, a simple counter.

The TCSPC allows PL response signal sampling even in picoseconds scale. Unfortunately, the time of integration is very long to implement this method in real-time measurement systems, which is our goal.

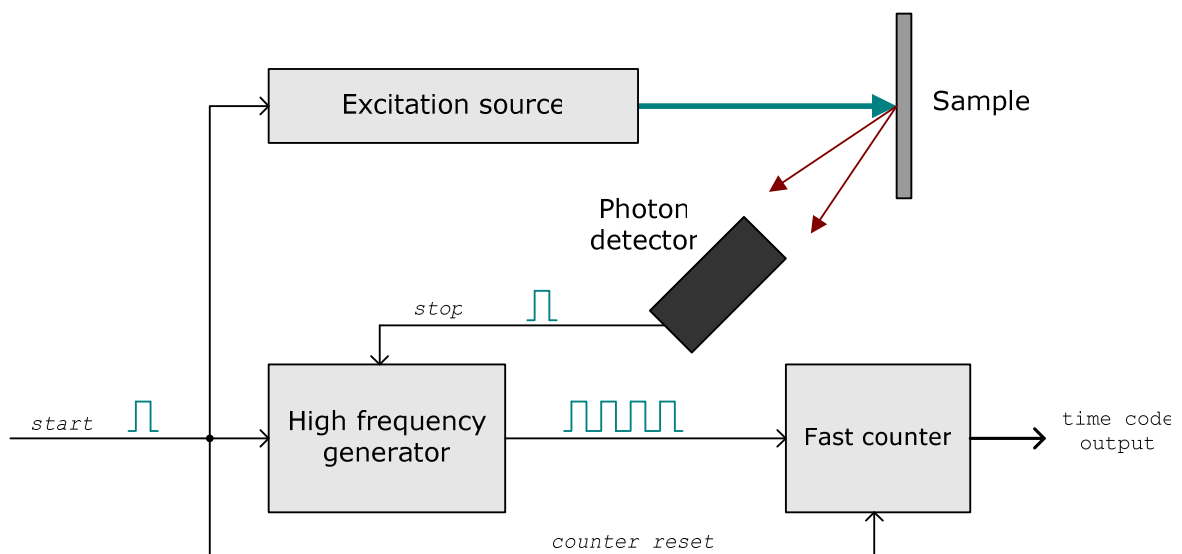


Figure 2.2 TCSPC implementation scheme

Concerning the porous Si S-band decay, the TCSPC could be implemented. But the problem is that it takes too much time to accumulate the necessary quantity of timeframes for decay curve reconstruction. The total PL extinction time of porous Si S-band is near 200 μs at room temperature and can reach several ms at low temperatures [108]. So the excitation pulses repetition rate can not exceed the value of several kHz (5 kHz for 200 μs decay). For a precise lifetime estimation, we should accumulate statistics on the capture of several millions photons, that lead to several tens minutes of integration. This limitation definitely does not allow building a real-time sensing system which tends to monitor relatively fast processes causing luminescence decay time changes.

A slight modification of TCSPC technique is proposed below that allows bypassing the limitation of such a long integration time.

2.2. Multiple Photons Counting

In TCSPC (Figure 2.2) we do not actually count photons but pulses coming from the high frequency oscillator. The detection of a photon triggers the stopping of the oscillator and the counter holds the number of pulses (time slices Δt) passed between the *start* signal and photon detection (*stop* signal).

The first assumption we can make is that there is no reason to stop photon counting after the first photon capturing is detected. The principle of multiple photon counting consists in continuing counting the photons coming from the sample during the defined timeframe. This allows to capture all photons coming from the excited sample and thus to obtain a reliable decay curve with less excitation pulses repetitions. In such a manner, the lifetime estimation for long decay time luminescent materials can be reduced to the value of minutes. The modified scheme is presented in (Figure 2.3).

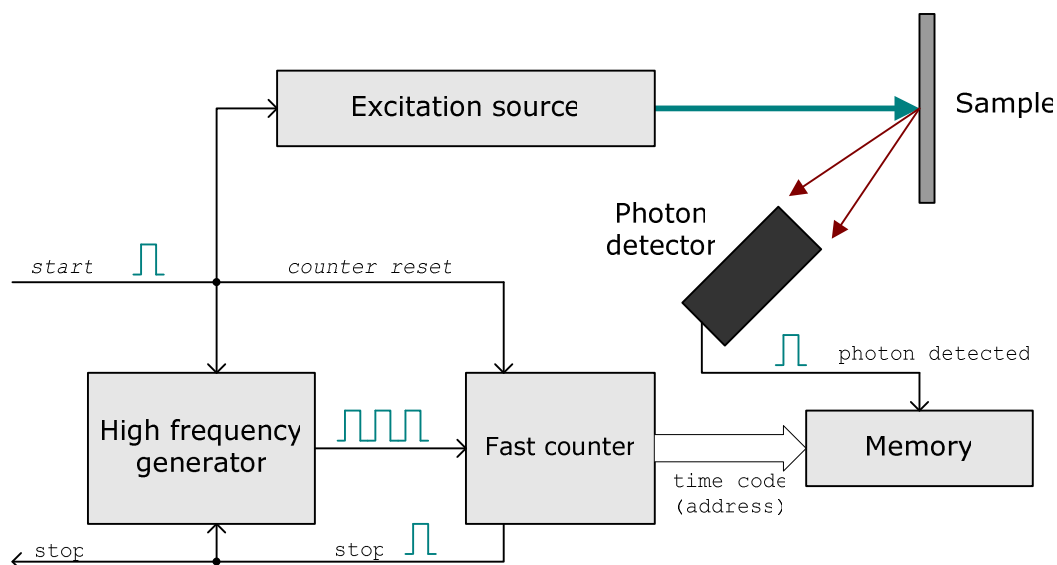


Figure 2.3 Multiple photon counting implementation scheme

For the scheme presented, after a single excitation pulse (triggered by `start` signal) passed and when the counting is finished (`stop` signal received from counter), the memory will hold a set of logical values, each element of this set will answer the question whether a photon was detected during corresponding time slice or not (time slice obviously corresponds to the period of pulses generated by the high frequency oscillator). Figure 2.4 represents the content of the memory after a single excitation passed. Obviously, integration over several excitations allows reconstructing a PL decay waveform.

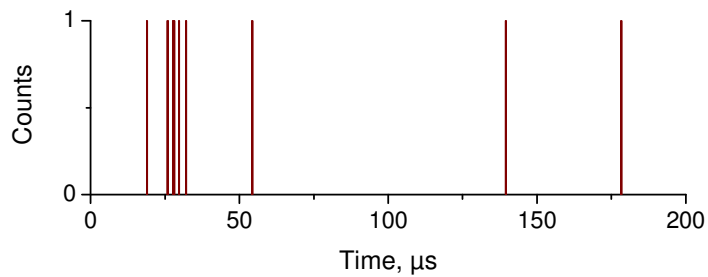


Figure 2.4 Photons detected after a single excitation pulse (9 photons detected within 200 μ s)

It is clear that the scheme represented in Figure 2.3 allows reconstructing of the decay waveform much faster as it counts all photons coming after the excitation pulse and not only the first one, as it is in TCSPC technique. However, a high frequency counting is still required. This forces to use a high frequency generator and counter to count the memory address as well as a roomy and very fast memory bank. Decreasing the counting frequency will finally lead to the situation when during a single time slice Δt , we will receive two or more pulses from photon detector. If several photon pulses are counted as a single one, the reconstruction of the PL decay signal waveform will not be possible, and the estimated lifetime value will be rather far from the real one.

In this case, using a separate counter for photon pulses can be proposed to solve this problem (actually replacing photons detector by photon counter). So, the modified scheme of multiple photons counter is presented in Figure 2.5. In this implementation, each memory cell holds the number of pulses coming from photons counter. At the beginning of each time slot, the photon counter should be reset. This is accomplished by taking the output pulses from the generator as a reset signal source. It should be mentioned, that photons counter, referred as ‘Fast counter’ in Figure 2.5 should be rather fast to separate two consecutive photon pulses. Usually this counter is hosted on a counter boards coming with photons detector (photon counting boards).

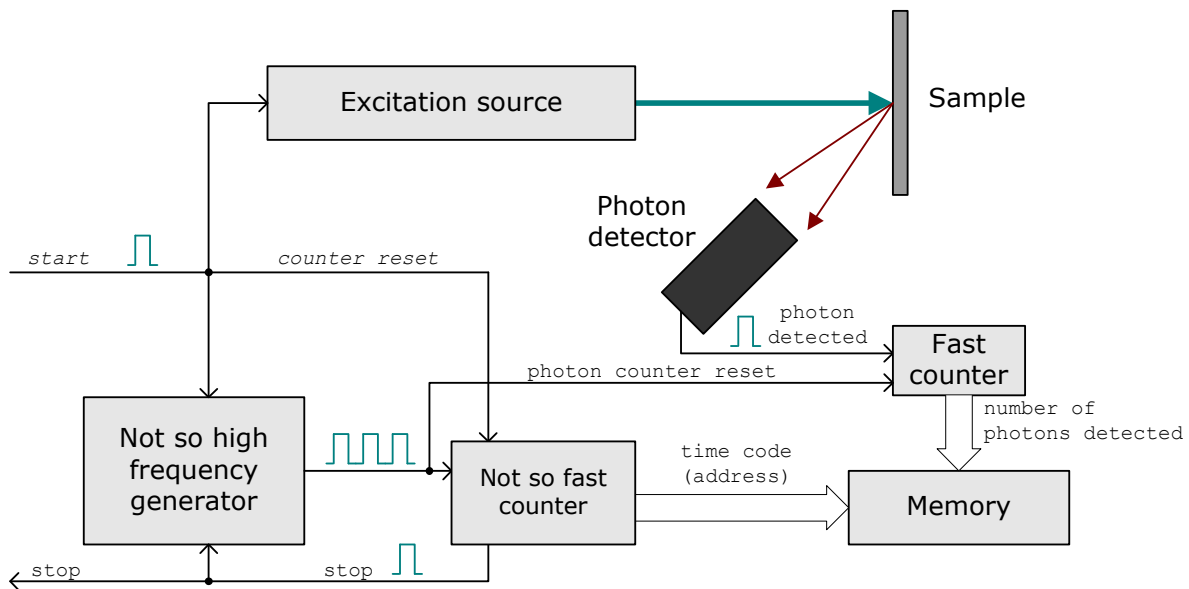


Figure 2.5 Multiple photons counting with a wide time slot

The scheme represented on Figure 2.5 works very well for porous Si luminescence detection as it is rather slow process. For the microseconds decay scale, there is no need to perform the counting with very short (ns) time slots as for fast decay fluorophores, so even a microsecond time slot is quite enough. With such a wide time slot, the situation with several photons detected during a single time slot becomes very probable. The (Figure 2.6) represents the memory content after a single excitation pulse passed and further counting with 200 ns time slice. As one can see, even the situation with 4 photons coming during these 200 ns is quite possible for high PL intensities.

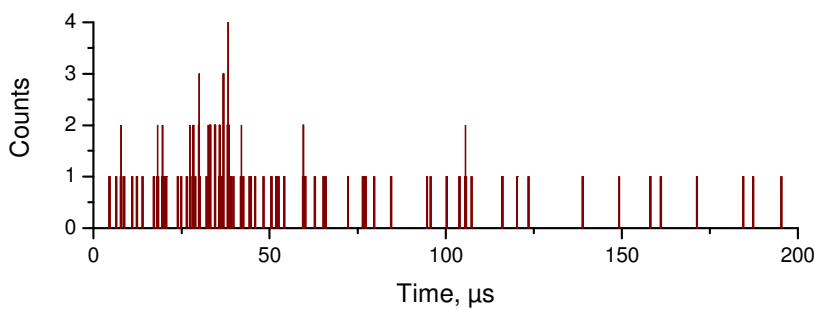


Figure 2.6

Photons detected after a single excitation pulse, time slot $\Delta t = 200$ ns

The PL decay estimation techniques based on photon counting allows near perfect decay waveform reconstruction. In this case the difference between the measured decay curve and the real one can only be caused by a non-ideal (not a δ function) excitation pulse, formula (2.1). But knowing the shape of the excitation pulse $E(t)$, the inverse deconvolution can be performed to obtain the real decay waveform. The proposed measurement scheme allows obtaining the decay curve of PL signal in several seconds. This is quite acceptable for

PL monitoring of fast processes and constructing of real-time measurement system. The method described in Figure 2.5 will be used in chapter 3.

2.3. Analog Mode of Photoluminescence Detection

Photon counting is a very sensitive method of PL signal detection. However, it works well only for rather low intensities. High PL intensity will cause a large quantity of photons being captured by the photomultiplier detector which will not be taken by the photon counter discriminator [109] because of the photomultiplier saturation. This will be manifested in the decrease of signal obtained while increasing of the actual PL intensity. Additional optical filters can be used to suppress high PL signal coming to the photon detector. Also it is possible to use not so sensitive detectors as photon counters to fetch the PL signal, like simple photomultiplier tubes with analog output or even fast photodiodes. In this case, an efficient PL decay signal can be obtained even with a single excitation pulse. The Figure 2.7 represents a PL decay measurement implementation using an analog detector.

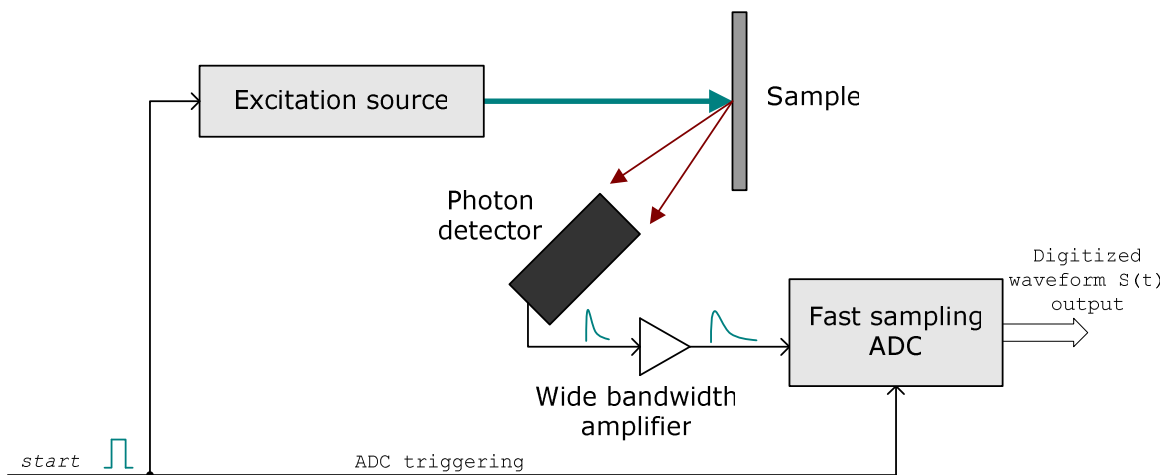


Figure 2.7 PL decay measurement with analog detector

For the measurement method presented here a perfect decay waveform reconstruction is possible only by deconvolution of the amplified output signal with the excitation source pulse response functions. It should be noticed that the influence of analog part of this detection scheme can change the decay waveform dramatically, so for the precise lifetime estimation, a further deconvolution operation is required. To make a deconvolution operation possible an amplifier with a wide bandwidth (several hundreds MHz for microsecond decay detection) should be used as well as a fast sampling ADC (with 1 MHz sample rate and higher, depending on PL decay time).

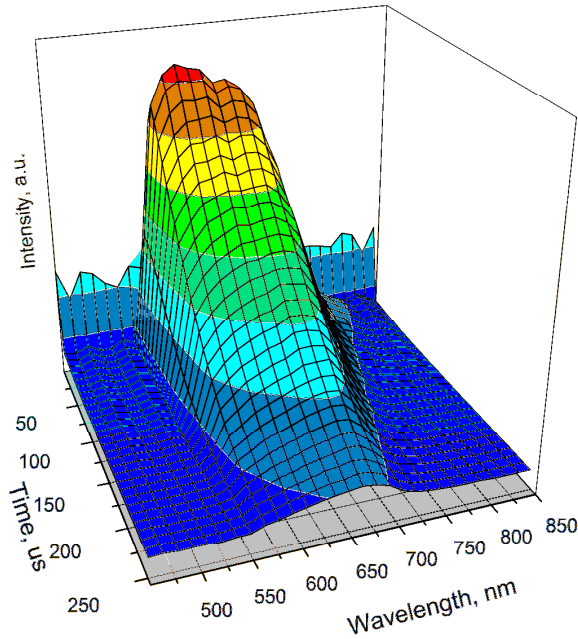


Figure 2.8

Porous silicon
photoluminescence spectrum
decay.

The described measurement scheme (Figure 2.7) was implemented in our work to obtain the whole spectrum decay of porous silicon samples (Figure 2.8). The method is very fast and allows wavelength/time spectrum scanning to be implemented in several minutes.

3. Frequency Domain Measurement

To avoid the use of high frequency devices (like wide bandwidth amplifiers and fast sampling ADC), a transposition from the time domain to the frequency domain measurement can be proposed. One can consider a luminescent sample as a system which takes an excitation signal on input and produces a PL response signal on output. By passing a $\delta(t)$ function to the input of this system we will get the system pulse response (i.e. a PL decay signal) on the output. In this case, the luminescent sample behavior is described by the pulse response function defined in the time domain. But the same behavior can be described by the system frequency response in the frequency domain. A frequency response is related to the pulse response by the Fourier transformation:

$$I(\omega) = \int_0^{\infty} I(t) \cdot e^{j\omega t} dt \quad (2.2)$$

Where $I(t)$ is a system pulse response, $I(\omega)$ is a system frequency response, and $j = \sqrt{-1}$. Assume that PL decay can be well described by a single exponential decay (in general case this is not true, since porous Si samples can manifest multiexponential PL decay [110]):

$$I(t) = I_0 \cdot e^{-\frac{t}{\tau}} \quad (2.3)$$

In this case $I(\omega)$ can be calculated as follows:

$$I(\omega) = \int_0^{\infty} I_0 \cdot e^{-\frac{t}{\tau}} \cdot e^{j\omega t} dt = \frac{I_0}{\frac{1}{\tau} - j\omega} \quad (2.4)$$

The further transformation and normalizing condition $I(\omega = 0) = 1$ will give:

$$|I(\omega)| = \frac{1}{\sqrt{1 + \tau^2 \omega^2}}, \quad (2.5)$$

$$\phi(\omega) = \arctan\left(\frac{1}{\tau\omega}\right)$$

Where $|I(\omega)|$ is a frequency response amplitude, $\phi(\omega)$ is its corresponding phase. The functions $|I(\omega)|$ and $\phi(\omega)$ define the frequency characteristics of the luminescent system. The dependence of $|I(\omega)|$ for different values of PL lifetime τ is represented in the Figure 2.9.

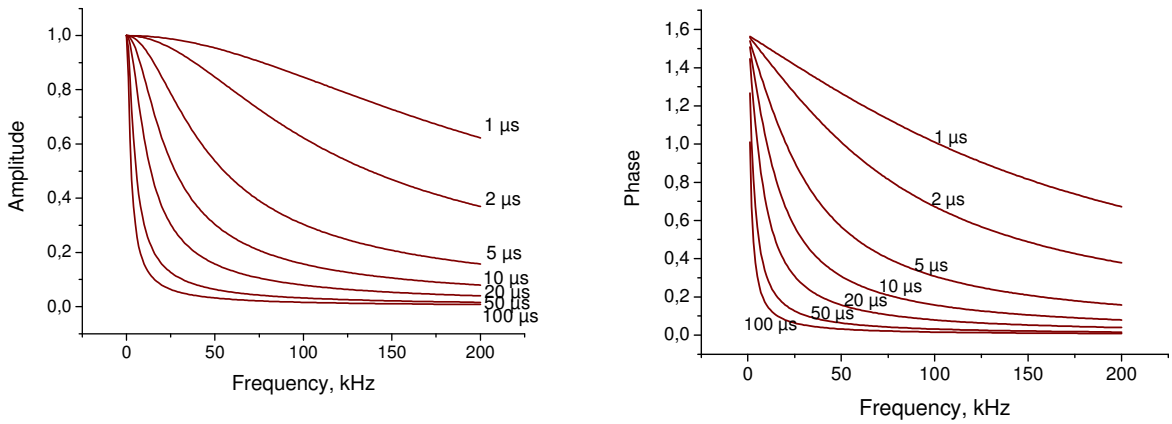


Figure 2.9 Frequency response amplitude and phase calculated for different PL decay times

The curve $|I(\omega)|$ can easily be obtained experimentally by modulating the PL excitation light source. The time domain PL decay $I(t)$ can further be calculated as an inverse Fourier transformation of $|I(\omega)|$. In the particular case of porous silicon, the S-band decay is rather slow (several tens microseconds). So, the excitation modulation frequencies can be limited to several hundreds of kHz. With such low modulation frequencies a simple electrically modulated blue LED can be used as the PL excitation source. The implementation of the frequency domain PL decay measurement scheme is presented in Figure 2.10. This method is very sensitive and has a high SNR. The PL decay can be easily obtained even in the condition of background illumination, as far as a selective amplifier will pass the modulated signal only.

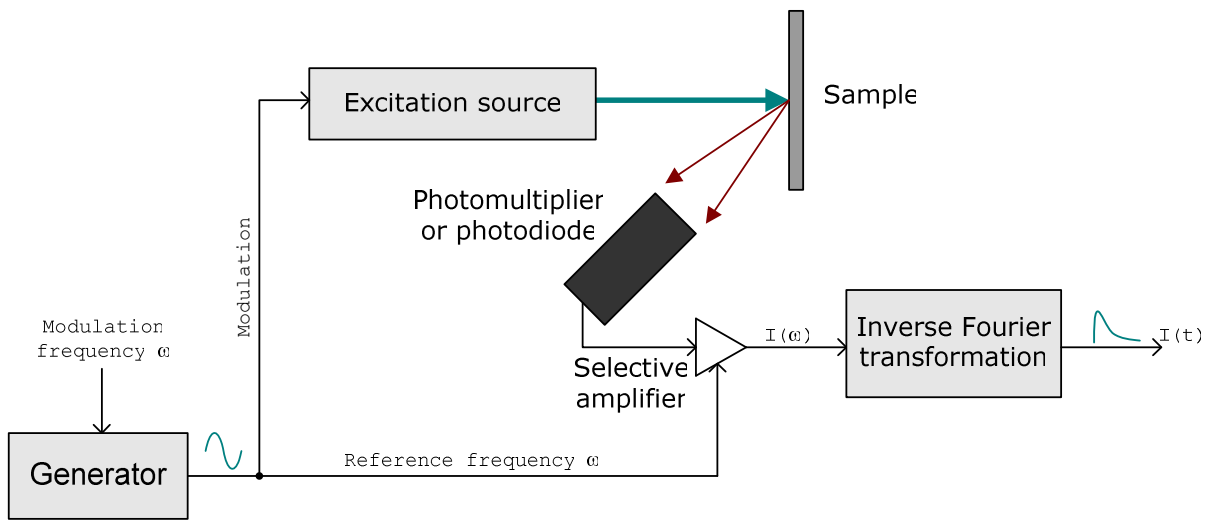


Figure 2.10 Frequency domain PL decay measurement technique scheme

The frequency domain PL decay measurement scheme implemented allows theoretically a perfect reconstruction of the decay waveform. This can be accomplished with a high frequency signal sampling to perform the inverse Fourier transformation as accurate as possible. In practice a perfect PL decay curve reconstruction is not required to estimate the decay lifetime. Several frequencies will be quite enough to make a decision. The Figure 2.11 presents the amplitude of an experimental porous silicon sample PL frequency response measured using six modulation frequencies.

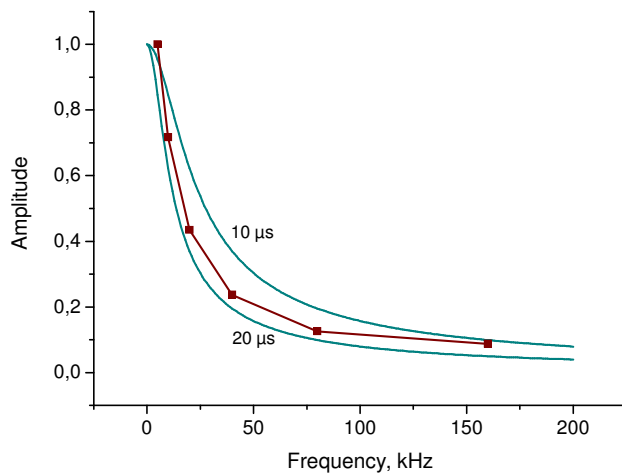


Figure 2.11

Porous silicon sample PL decay ($\tau \approx 15 \mu\text{s}$) measured in frequency domain (line with markers) between two theoretically calculated curves for $\tau = 10 \mu\text{s}$ and $\tau = 20 \mu\text{s}$

The value of lifetime can be well estimated by the experimental data fitting according to the formula (2.5). Along with the amplitude measurement, which is dependent on the PL lifetime and on the PL intensity I_0 , the measurement of the phase can be as well performed. As one can see the phase is dependent only on decay lifetime τ .

4. Comparison between the different methods

The TCSPC method is a very powerful technique of PL decay waveform estimation. However it is not acceptable for real-time PL measurement systems which require a wide dynamic range (in the sense of PL intensity and decay time) and fast data acquisition. Several modifications over classical TCSPC technique have been proposed to implement photon counting to obtain slow (nanosecond-microsecond scale) PL decay curves during a reasonable time of measurement. Anyhow the solution based on the frequency domain measurement is more preferable when PL decay waveform is not required, but just a decay time value.

All the PL decay measurement methods described were tested on porous silicon samples to measure its S-band decay. The advantages and drawbacks of each method are summarized in the following table (Table 2.1).

Table 2.1 PL decay measurement techniques comparison

Measurement technique	Complexity of realization	Time performance	PL intensity, dynamic range	Perfect decay signal reconstruction
Time correlated single photon counting	complex	very slow	low intensities, narrow dynamic range of τ	possible
Multiple photons counting	complex	slow	low intensities, narrow dynamic range of τ	possible
Multiple photons counting with a wide time slot	medium complexity	slow	low intensities, narrow dynamic range of τ	possible
PL analog detection	simple	very fast	high intensities, wide dynamic range of τ	with deconvolution
Frequency domain measurement	medium complexity	fast	Wide dynamic range of intensity and τ	with inverse Fourier transformation

As one can see, the methods based on photon counting have rather low performance but are indispensable for measuring low PL intensities. The analog detection method as well as frequency domain one is very fast and well applicable in real-time measurement systems but can't work with low PL intensities. The combination of several methods described can also be implemented in final measurement system to cover wide intensity ranges and decay times. Particularly in our further research work (chapters 3) on porous silicon

photoluminescence, the method of multiple photons counting with a wide time slot was chosen.

5. PL lifetime measurement setup

The measurement setup presented in this work was designed to investigate porous silicon PL decay for further experimentations and development of sensing systems using porous silicon as an optical transducer. This setup is based on multiple photons counting scheme (Figure 2.5) with wide time slot (this means that several photons can be captured during this time window). It uses a fixed time window of 200 ns (which actually can be changed by firmware modification) to fetch the data from the counter and a memory array to keep the data for up to 1000 time slots. This allows monitoring up to 200 μ s of signal decay. For accurate decay signal fetching an additional delay line was added (using programmable delay line AD9501), but for porous Si S-band luminescence decay such a fast signal fetching is not really required.

As an excitation source, a simple blue LED (395 nm of emission maximum) was used. The emission spectrum of the LED is presented in (Figure 2.12). An excitation module assembled on NE555 popular timer provides a fixed excitation pulse shape with defined duration. In our experiments the output of NE555 timer was used to flash a blue LED used for porous silicon luminescence excitation. The duration of excitation pulse was approximately 50 μ s with amplitude of 10 V.

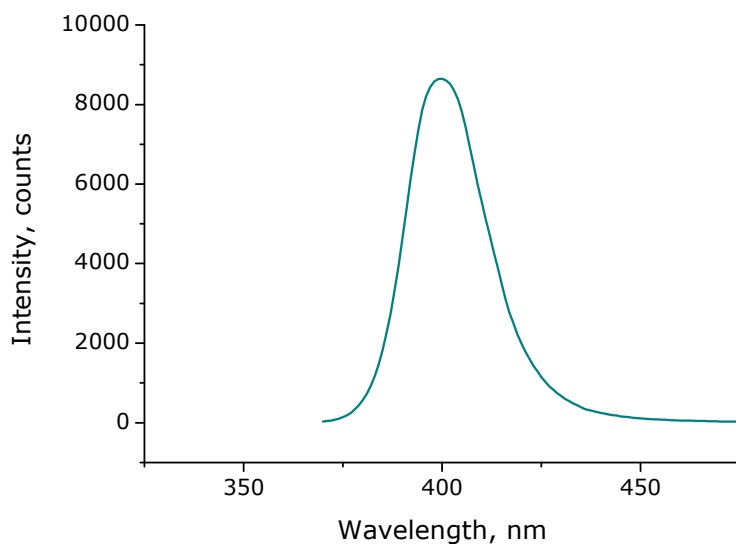


Figure 2.12

Excitation LED spectrum
(λ_{\max} =395 nm).

For the PL detection, a photomultiplier HAMAMATSU H7360-03 was used. This device has a TTL output so it can be directly connected to TTL counter. The photomultiplier was coupled with an optical band-pass filter (XF3076 from Omega Optical) to pick out the

interesting part of the PL spectrum. The transmission spectrum of the filter is presented in Figure 2.13.

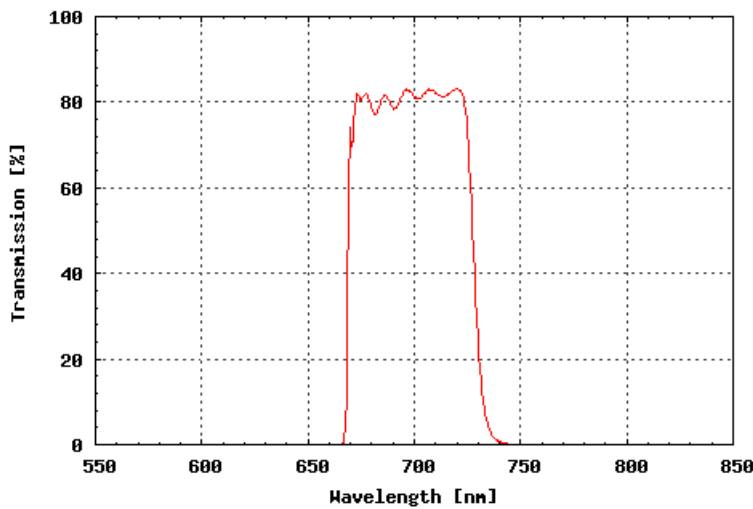


Figure 2.13
XF3076 band-pass filter transmission spectrum.

As a heart of the counting board, a 8-bits ATMEL ATmega16 microcontroller (MCU) was used (Figure 2.14).

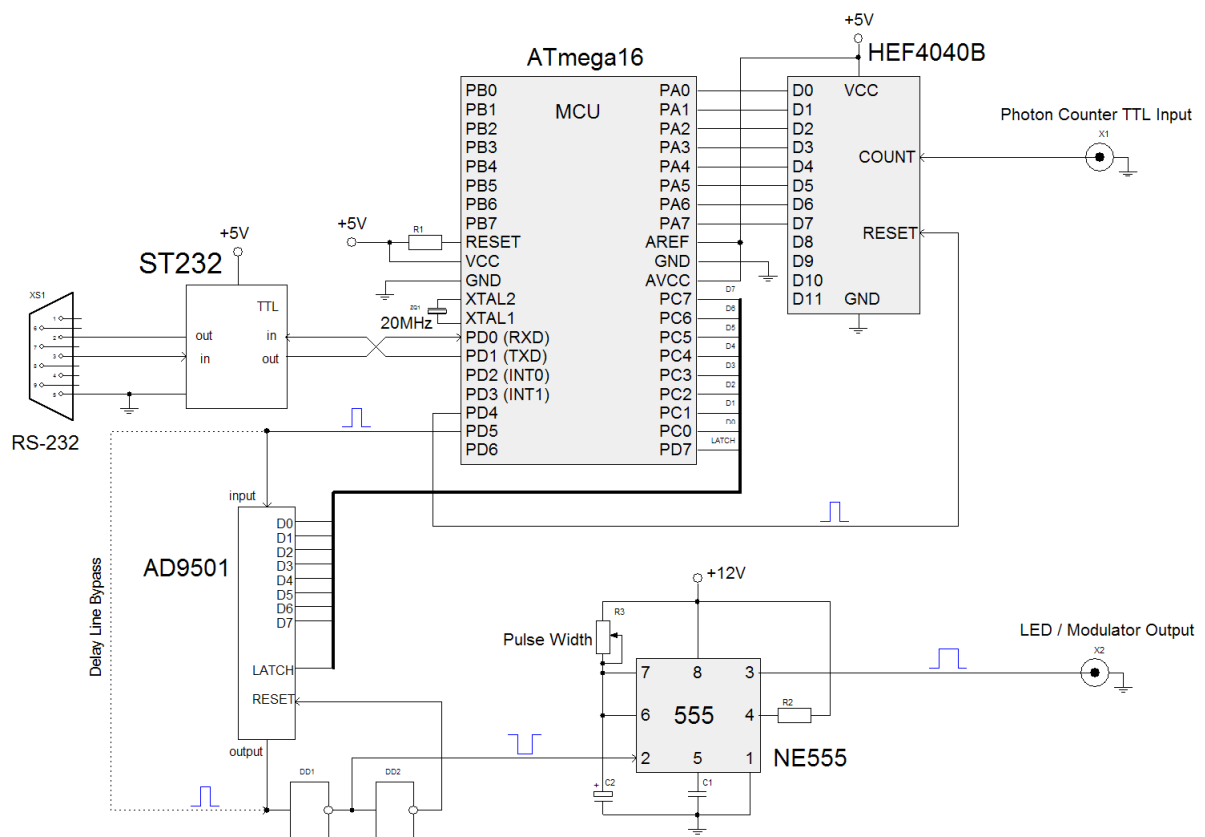


Figure 2.14 Photon counting and integration board circuit schematic

The MCU controls the photons counting process: launching measurement by sending a trigger pulse to LED excitation module, accumulating photon counts from the photomultiplier into internal memory, and communicating with desktop PC over the RS-232 link to pass the data

and receive control commands. The MCU clock frequency is 20 MHz and is stabilized by an external quartz crystal (MCU was overclocked to gain the performance on counting). This frequency actually limits the shortest possible time slot for counts fetching from the hardware counter to the memory of MCU. This is accomplished by sequent execution of two MCU instructions: read data from the port A (Figure 2.14) and save data in the internal memory while incrementing memory address by one. These instructions take two MCU cycles each (50 ns for 20 MHz clock). That is why the shortest possible time window is 200 ns for this schema.

It should be mentioned that there is no counter clear pulses sent during the whole measurement cycle (i.e. 200 μ s). The counter is cleared only once just after the excitation pulse was sent. This trick tends to save some MCU cycles to reach the maximal performance. In such way, we do not get actually a real decay waveform but time integration of it. The following figure (Figure 2.15) represents such a signal obtained after 20000 accumulating cycles with the help of the counting board described.

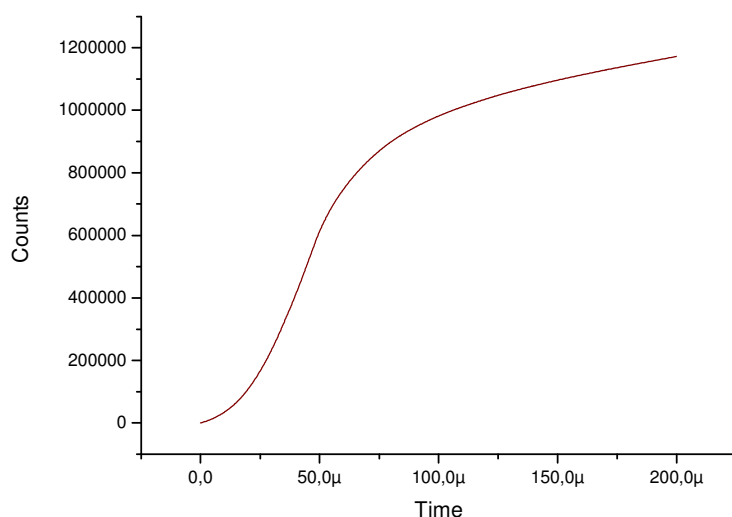


Figure 2.15

Integrated decay signal of porous silicon photoluminescence

The real decay signal can be obtained by differentiating this curve. The result of differentiation will correspond to the distribution of photon appearing probability within particular time window (i.e. PL decay). Here is the result (Figure 2.16) of differentiation of the curve in Figure 2.15.

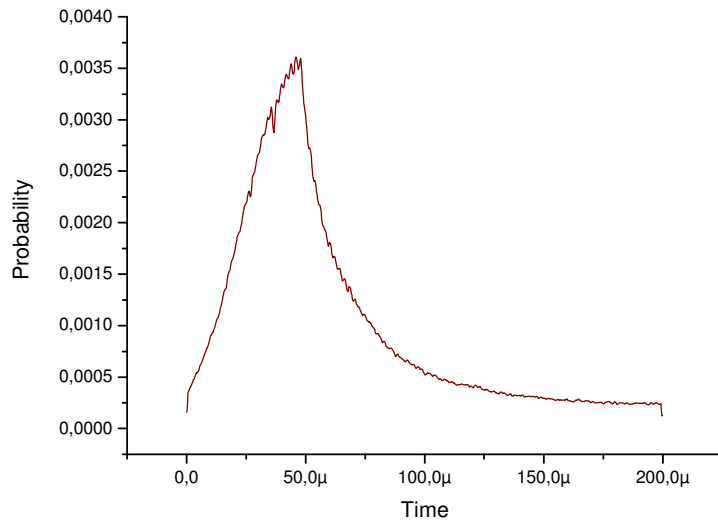


Figure 2.16

Photoluminescence decay curve (distribution of photon capturing probability) calculated as derivative of the curve represented in (Figure 2.15)

6. Conclusion

In this chapter we have described the classical PL lifetime measurement techniques and proposed some modifications to adapt them easily to porous silicon photoluminescence detection. Trying different approaches we have developed the automated PL measurement setup that allows fast acquisition of PL (S-band) decay curve for the porous silicon samples that we want to study in our further research.

Third Chapter

Influence of pH Solution on Photoluminescence of Porous Silicon

The radiative lifetime of as-prepared and modified layers of porous silicon were studied in liquid solutions with different pH. It was observed that porous Si photoluminescence (PL) intensity and decay lifetime strongly depend on pH value. This phenomenon is explained by competition of the following processes: UV-induced hydrogen desorption, hydrogen adsorption from the buffer solution, and porous silicon oxidation. Taking advantage of this phenomenon, a pH change sensor can be proposed. Porous Si layer degradation can be decreased somehow by protective PEDOT layer.

The material of this chapter is published in [111].

1. Introduction

Porous silicon became a new promising optoelectronic material since the first observation of its efficient photoluminescence (PL) at room temperature. Currently the stabilization of the porous silicon is an important problem in order to create efficient sensor systems using its properties. Porous Si degradation by etching in aggressive environments (such as strong acids and bases) [112] and oxidation in open air or in aqueous solutions [113] are the most objectionable processes leading to porous silicon electrical (increase of resistivity) and optical (PL irreversible quenching) degradation [81, 114, 115]. Many works are dedicated to the stabilization of porous Si layer applying different treatment methods [102]. These include chemical treatment [74, 77, 116], mechanical protection by polymers

[117], or preliminary treatments [64, 68, 118] in order to stabilize the near-surface layer of porous silicon.

In this part of the thesis, the influence of pH buffer solutions on porous silicon photoluminescence was studied. To stabilize the surface of porous silicon and reduce somehow the PL degradation, a poly-3,4-ethylenedioxythiophene (PEDOT) polymer coating was used. As a result of the investigation of pH-dependent PL intensity and/or decay lifetime, a pH sensitive sensor is suggested.

2. Samples and Experiment

Porous Silicon samples were prepared using routine anodization process by applying a constant anodic current to p-doped silicon slabs ($\sim 10 \Omega\cdot\text{cm}$) with (100) crystallographic orientation. The etching was carried out in an etching solution consisting of hydrofluoric acid (48%):ethanol = 1:1 (vol.) using the cell described in chapter 1. Porosity of the samples obtained was estimated to be near 60%. Porous silicon layer thickness was approximately $1 \mu\text{m}$. Some samples were covered by PEDOT polymer by spin coating, to protect the porous silicon surface from degradation in aqueous solutions.

Porous silicon photoluminescence spectra were investigated using a time-resolved spectrometry carried out at room temperature. The samples PL was excited with a pulse nitrogen laser ($\lambda=337 \text{ nm}$, FWHM=8 ns, power in pulse 20 kW) or with blue LED ($\lambda=395 \text{ nm}$), powered in pulse mode. The proper band of PL emission was selected by a monochromator (MS2004, SOLAR T II). The signal was registered by a photomultiplier (HAMAMATSU C6270) used in analog mode or photon counting photomultiplier (HAMAMATSU H7360-03) used in multiple photons counting mode with time slot of 200 ns (as described in chapter 2). The prepared samples manifested a visible luminescence with a maximal intensity at 650-750 nm band (Figure 3.1) which corresponds to the S-band of PL [3].

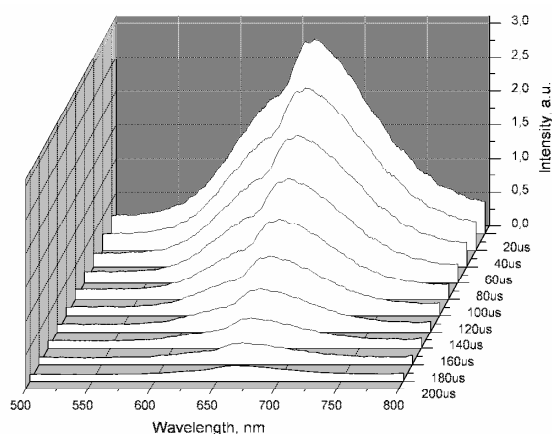


Figure 3.1

Transient PL spectra of porous silicon measured in analog mode (without deconvolution). Please, refer the chapter 2 for the measurement method description.

To study the pH influence on the PL of porous silicon, we prepared several buffer solutions with different pH values. We used a multi-component ‘polymix’ buffer with the following composition: 2.5 mM Tris, 2.5 mM citric acid, 2.5 mM sodium tetraborate, 2.5 mM potassium phosphate. The level of pH was adjusted with 1 M HCl or 1 M NaOH solutions in order to obtain the expected pH value. The buffer capacity was stable over a wide range of pH (from 5 to 9) [119]*. In the 2.2—3.6 range of pH, we applied an acidic 0.1 M buffer composed of glycine and HCl. The desired level of pH was adjusted by 1 M HCl.

It was found, that the PL spectra shapes for homogeneous porous silicon layers were not greatly affected by different pH buffers, so only integral intensity and lifetime at maximum emission wavelength were studied. In this way, the measurement setup for pH influence investigation was simplified and compacted. The monochromator was replaced by a band-pass filter to pick out the interesting spectral range (670—730 nm). The porous silicon sample was placed in a flow-through cell with a window providing PL excitation and registration (Figure 3.2).

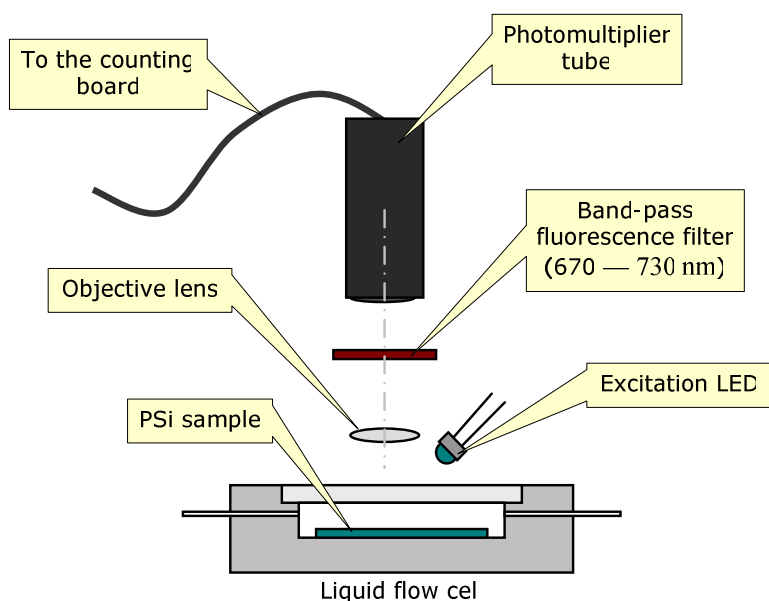


Figure 3.2
Setup for PL intensity and decay time measurement

3. Photoluminescence Measurement

Porous silicon photoluminescence intensity appeared to be very sensitive to the pH value of the solution passed through the flow cell (Figure 3.3). PL appears to be more intense in acid environment while immersion into basic solutions leads to fast PL quenching. The exponential law of S-band decay is observed only at late time of decay. For early time it reveals more complex multiexponential behavior. Thus, the proper parameter of decay lifetime τ (as in the function $\sim e^{-\frac{t}{\tau}}$) can be introduced for the longtime tail of PL decay curve.

* This buffer is usually used to study the influence of pH on the ISFET responses, (especially enzyme-modified ISFETs).

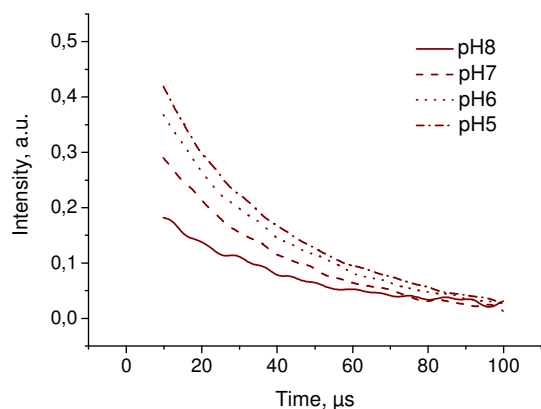


Figure 3.3

Longtime tail of PL decays of as-prepared porous Si in several pH buffers

Cyclic change of buffer in the flow cell leads to adequate change of porous Si PL intensity and decay lifetime (Figure 3.4).

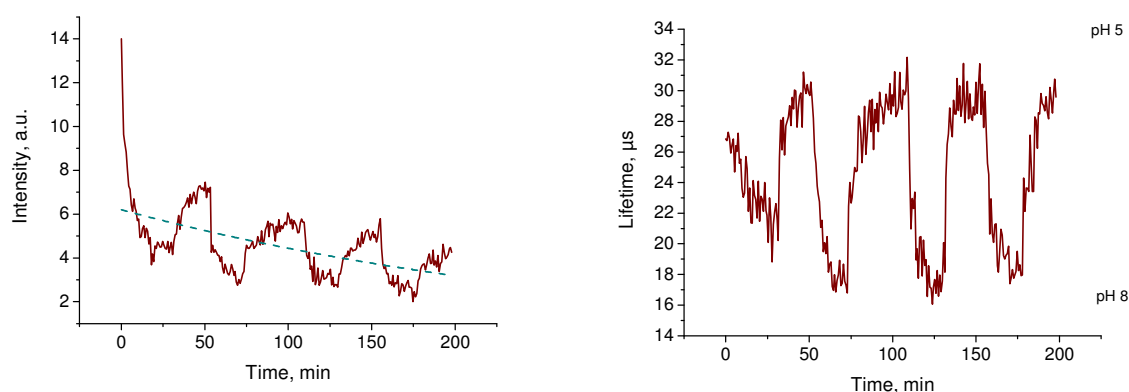


Figure 3.4 PL intensity and PL decay time for as-prepared porous silicon cyclically exposed to buffer solutions of pH=8 (low PL intensity and decay time), and pH=5 (high PL intensity and decay time). PL quenching time ~300 min (dashed curve)

PL intensity quenching was observed when the samples were exposed to different pH buffers. One can notice (Figure 3.4), that degradation of PL lifetime is almost not observed. However the noise level of measured lifetime value increases with decrease of PL intensity.

The PL degradation of porous Si placed in pH buffer can be explained by partial oxidation of the material in aqueous solutions (as far as all buffers consist of more than 90% of water). It is known, that porous Si being immersed in water begins to oxidize, that leads to the increase of porous Si surface wettability [120]. The presence of silicon oxide bonds in this case can be easily monitored with FTIR spectroscopy. Porous Si oxidation leads to PL degradation [81]. Furthermore, a permanent UV illumination of porous Si sample immersed in aqueous solution leads to even stronger PL quenching (Figure 3.5). This phenomenon is

well described by UV-induced hydrogen effusion from porous Si and defect generation in near-surface region of porous Si [120, 121] due to the photooxidation process [83].

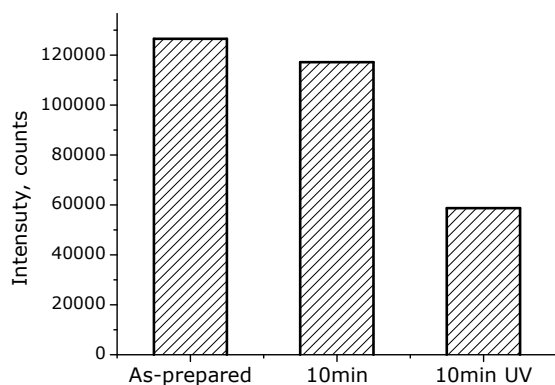


Figure 3.5

PL intensity of as-prepared porous Si sample. The sample was treated for 10 min in pH=6 buffer in the dark, and treated for 10 min in pH=6 buffer while permanent UV (400 nm LED) illumination

A photooxidation process also takes place while the sample is directly exposed to the UV illumination [8]. The UV irradiation leads to an increase in the intensity of Si—O stretching bands and the H—Si—O₃ deformation and stretching bands in IR absorption. The decrease in intensity of these four bands after etching in HF indicates the formation of an oxide layer under UV illumination. Its appearance is also accompanied by a reduction in the intensity of all Si—H bands (664, 906, 2087, 2106, and 2140 cm⁻¹). Figure 3.6 shows the increase of oxide bands and the decrease of Si—H_n bonds upon UV illumination of the porous Si layer.

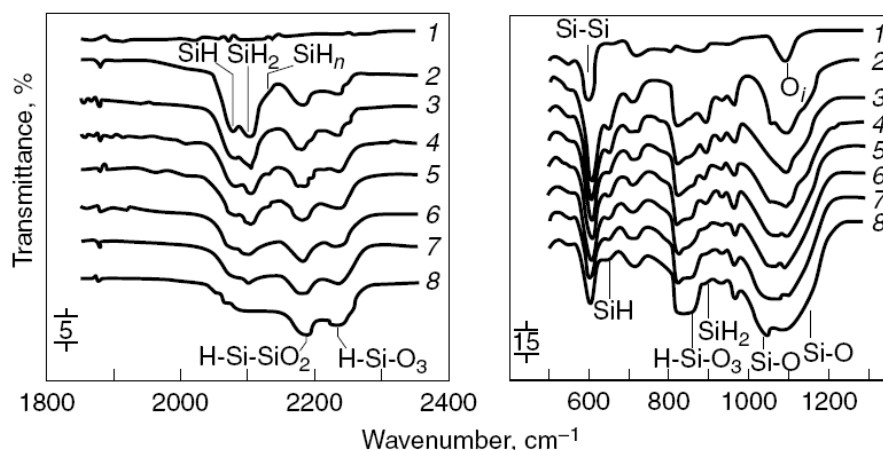


Figure 3.6 IR normal-incidence transmission spectra of (1) Si-substrate and (2—8) porous Si samples upon UV illumination for various times: (2) 0, (3) 10, (4) 20, (5) 30, (6) 40, (7) 60, and (8) 100 minutes.

After the removal from the alkaline solution, the measured PL intensity and decay time recover when the sample is exposed to acid buffers (pH < 7.4), which can be explained by silicon-hydrogen bands restoration in the acid buffer solution. Thus, several processes take

place simultaneously: hydrogen effusion caused by UV illumination of porous Si sample, hydrogen adsorption from the buffer solution, oxidation in water solution and under UV illumination. Obviously, a detailed equilibrium of these processes leads to a definite value of PL intensity and decay time. However, if a constant degradation of porous Si layer takes place due to oxidation process in every buffer solution, the supplementary porous Si etching occurs only in basic solutions.

4. Sensor protection by PEDOT layer

Semipermeable polymers, such as PEDOT seems to be applicable for stabilizing of porous Si [117] preventing somehow porous Si layer oxidation and etching and allowing at the same time free access of ions (H^+ in our case) to the surface. Covering the samples by PEDOT polymer in order to protect the porous surface, decreases somehow the degradation of PL intensity (Figure 3.7), but the sample degrades nevertheless while being treated in solution for several hours. Thin polymer layers can not protect the surface against aggressive environment (acids or bases) for a long time, and thick polymer layers are not permeable enough to ensure sufficient sensitivity of porous Si based sensor.

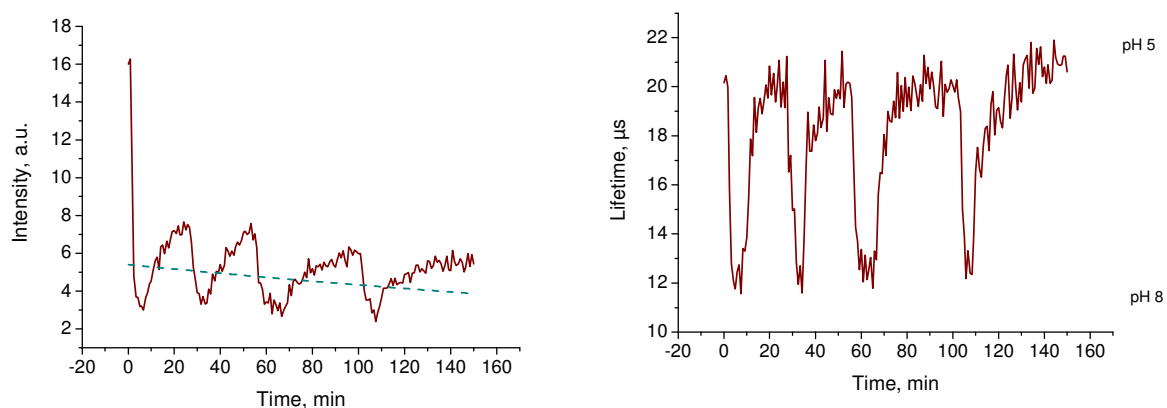


Figure 3.7 PL intensity and PL decay time for PEDOT covered porous Si cyclically exposed to buffer solutions of pH=8 (low PL intensity and decay time), and pH=5 (high PL intensity and decay time). PL quenching time ~450 min (dashed curve)

5. Comparison with other sensors

In contrast to known pH-sensible porous Si sensors based on the field effect [97-99, 122], PL measurements allows to perform a contact-free monitoring. An average sensitivity (signal change ΔI or $\Delta \tau$ to absolute signal value I or τ ratio) of the pH sensor proposed is showed in the Table 3.1. This shows that field effect based sensors [97-99, 122], which have $\Delta I/I \sim 0.6 - 1.2$, are still more efficient than our PL based porous Si sensor.

Table 3.1 Comparing sensing capabilities of as-prepared and PEDOT covered samples

Sample	PL intensity $\Delta I/I$ ($\Delta pH=1$)	PL lifetime $\Delta\tau/\tau$ ($\Delta pH=1$)	PL quenching time, min
As-prepared	0.1	0.22	300
PEDOT covered	0.17	0.22	450

The following figure represents the response of porous Si PL intensity on pH level random changes (Figure 3.8) for our pH sensing system. The nonreversible degradation of PL is observed during the whole measurement process (even for the samples, covered by polymer).

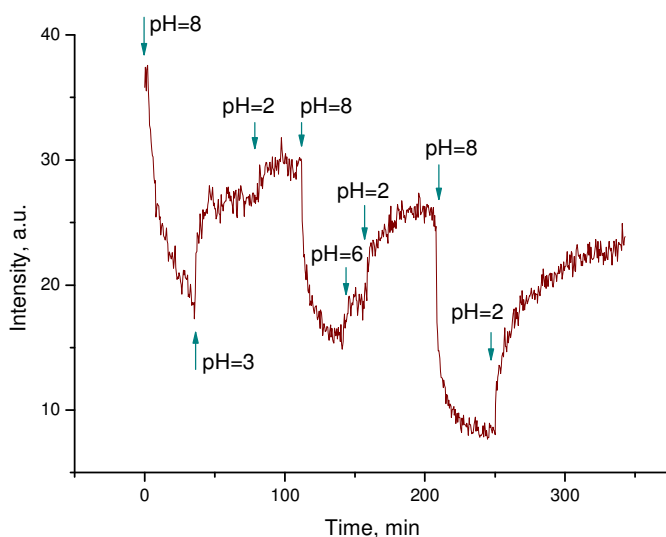


Figure 3.8

PL intensity of porous Si sample exposed to different buffer solutions (the arrows show the moments of buffer change).

6. Conclusions

Porous silicon photoluminescence is very sensitive to the pH level of buffer solutions. Changes of pH value lead to corresponding changes in PL intensity and decay time. High PL intensity and long decay time correspond to low pH (acids) while low PL intensity and short decays correspond to high pH (bases). This phenomenon is well explained by competition of hydrogen effusion-adsorption and oxidation processes while UV illumination. The degradation of PL takes place for all pH buffers due to the porous Si oxidation in aqueous solution under UV illumination. Porous Si layer degradation (etching) is observed while the samples are being placed in alkaline solution ($pH > 7.4$). Using PEDOT as protective layer allows slowing down the degradation process but can't protect the sensor surface for durable time.

We have showed that PL lifetime measurement seems to be more preferable in comparison with PL intensity measurement as far as there is no lifetime signal degradation observed. Moreover the lifetime value of porous Si PL is not influenced by the optical losses in the tested solution and the optical system itself. However, low PL intensities do not allow obtaining an adequate accuracy of PL lifetime estimation that leads to low SNR value.

Fourth Chapter

Porous Silicon Substrates with Incorporated Catalytic Metal Nanoparticles for Sensors Application

In this chapter the formation of porous silicon by stain etching is considered. Incorporation of catalytic metals, such as Pt, Ag, and Ni was implemented directly during the etching process. Having catalytic metal particles inside pores of porous silicon can present an interest in research and development of porous silicon based sensors.

The introduction of metals during the formation of porous silicon layer can be applied to dope the porous layers, to create semiconductor matrixes with metal nanoclusters in pores and form sensors structures with electrical transducers (Schottky contact, FET, Ohmic resistor). This was first demonstrated for the case of Ag [123-125]. The modification of PS by catalytic metal as Pt, Pd, Ni, and Ag could lead to the reduction of the time as well as temperature during redox-oxide reactions.

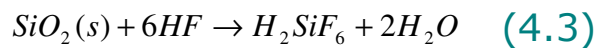
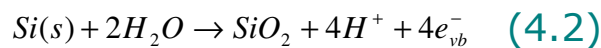
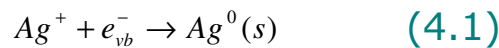
1. Mechanism of silicon etching at metal doping

The chemical (stain) Si etching in the mode of porosification is determined by the conditions of the transport of the fluoride ions to the reaction zone and silicon surface reactivity. The fluoride ions concentration near silicon surface depends on the bulk concentration of hydrofluoric acid. The HF and H_2F_2 complexes dominate in the water solution of HF at $pH < 2$, HF_2^- ions dominate at $2 < pH < 5$ and F^- ions dominate at $pH > 6$

[126]. The porous formation in Si is effective in the diluted HF acid. The successive porous Si layer growth is provided by the presence of insignificant amount of nitric acid or other oxidant in the etch solution. The production of the surface oxide stipulates the absorbed F⁻ ions and subsequent intensification of silicon etching. The concentration of HNO₃ is selected such a manner that the speed of SiO₂ oxide formation is considerably less than the speed of the production of the H₂SiF₆ insoluble complex [127].

The working principle of electroless deposition of metal is a galvanic displacement reaction. It means that the reduction of metal ions (cathodic process) and oxidation of silicon atoms (anodic process) occur simultaneously at the Si surface. The HF acid stipulates the opportunity of metal deposition with the direct substitution of Si atoms on the substrate. The anodic and cathodic processes take place simultaneously and the charge exchange is realized through the substrate. The Si surface is released from the oxide in the presence of fluoride-hydrogen combination and the cathodic metal deposition is realized with the simultaneous renewal of oxidant. The Si surface in the HF solution becomes hydrophobic that promotes the Ag ion adsorption. The deposited metal ions form nucleation centers during the etching process, which result in the porous Si layer formation with metal nanoclusters inside the pores. They are the centers of the charge exchange and they initiate the chemical deposition without the initial activation of the Si surface.

In the case of electroless deposition of Ag on Si slab from HF+HNO₃+AgNO₃ solution, the energy levels of Ag⁺/Ag system lie well below the Si valence band [128]. Surface Si atoms are oxidized (anodic reaction, (4.2)) and supply the electrons for the Ag⁺ reduction (cathodic reaction, (4.1)). Besides, anodic reaction includes the etching of silicon dioxides (4.3):



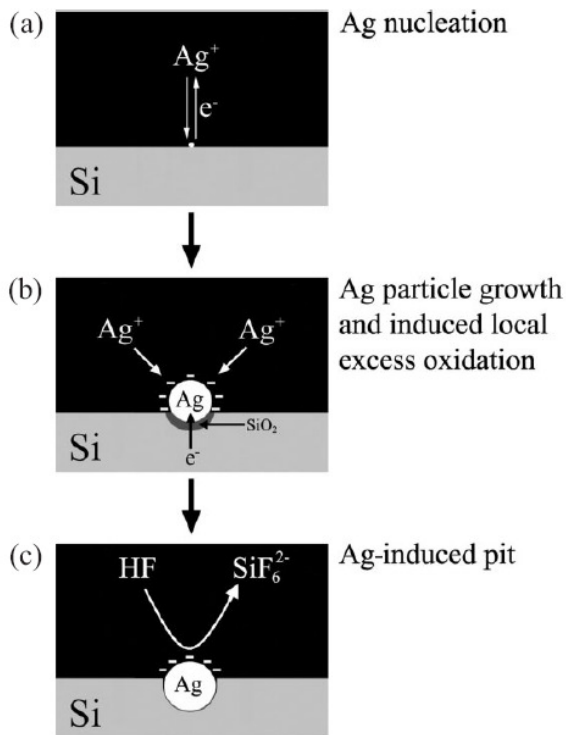


Figure 4.1

Mechanism of electroless Ag deposition on Si in HF/AgNO₃ solution [125].

These chemical reactions explain the silicon etching process, however, do not explain the process of Ag nucleation. According to [125, 128] in the initial stage of silver deposition, Ag⁺ ions in the vicinity of the Si surface capture electrons from the valence band of Si, and are deposited in the form of metallic Ag nuclei on a nanoscopic scale. The electron exchange between Ag⁺ ions and Si is more likely to take place at kinks, steps and other defects. As the Ag nuclei adhering to the Si surface are more electronegative than Si, these metallic Ag nuclei strongly attract electrons from Si and become negatively charged. These Ag nuclei serve to catalyze the subsequent reduction of Ag ions and facilitate Si oxidation. Therefore, other Ag⁺ ions coming close to Si surface preferentially get electrons from the Ag nuclei and are deposited around them. Thus, the Ag nuclei grow into larger areas as more Ag ions are deposited. Simultaneously, because the Si underneath the Ag particles releases as many electrons as are required by Ag ions to be reduced, excess local oxidation occurs, and SiO₂ is produced underneath these Ag nanoparticles. Shallow pits would immediately form under the Ag nanoparticles, due to the etching of SiO₂ by the diluted HF solution. Thus, the Ag nanoparticles trapped in these pits do not move horizontally. With longer immersion times in the HF/AgNO₃/HNO₃ solution, the Ag particles that do not enter the pits would grow into branched silver dendrites or metallic island on the surface (Figure 4.1).

2. Samples preparation

Electrochemical growing of porous silicon layers with metal nanoclusters is a problematic process since porous silicon formation is an anodic process and metal deposition is a cathodic process on the silicon electrode. Therefore we used only the stain chemical porous silicon formation. The metal introduction into pores is easier realized by mixtures based on hydrofluoric and nitric acids. We tried to incorporate three different metals: Ag (as in [123-125]), and for the first time to our knowledge, Pt and Ni.

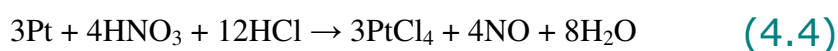
2.1. Ag incorporation

Substrates of n- and p- Si (100) with resistance of 1—10 $\Omega \cdot \text{cm}$ and thickness of 300 μm are used for Ag doping. The chemical formation of the porous silicon layer and simultaneous Ag deposition is provided in the solution: HF(48%): HNO₃(70%) : AgNO₃(1%) = 150:1:40 during 20 — 40 s. The characteristics of such samples have been compared with reference ones, with porous silicon layer formed by treatment in (HF:HNO₃:H₂O = 150:1:40) electrolyte without AgNO₃.

2.2. Pt incorporation

Boron doped ($N_p = 2\text{—}3 \cdot 10^{15} \text{ cm}^{-3}$) silicon slabs of (100) crystalline orientation, with 300 μm thickness were used as substrates for doping by Pt. The native silicon oxide was removed in aqueous solution HF:H₂O = 1:4 before the metal deposition. Then the silicon surfaces were treated with the solution, containing Pt and HF, prepared from the dissolution of sodium chloroplatinate. This solution was obtained by the following way [127]:

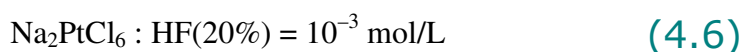
- 1) Making of chloroplatinum by Pt dissolution in a mixture of HNO₃ and HCl:



- 2) Sodium chloroplatinum production:



- 3) Preparation of solution for Pt deposition



All solutions were prepared from ultra pure grade reagents and bi-deionized water. The time of treatment ranged from 1 to 60 minutes. Immediately after the removal of the native oxide, the substrates were immersed in the solution gently stirred and held vertically. After Pt deposition, all substrates were rinsed in bi-deionized water.

2.3. Ni incorporation

Ni deposition during the porous silicon formation was performed by stain etching of p-doped Si (100) with resistance of $10\ \Omega\cdot\text{cm}$ in the following solution: $\text{HF}(48\%):\text{HNO}_3(70%):\text{Ni}(\text{NO}_3)_2(1\%) = 150:1:50$ during 1—2 minutes.

For some samples, we tried first to form porous silicon with preliminary etching in $\text{HF}(48%):\text{HNO}_3(70%)=150:1$ solution for 1 minute, and then we incorporated Ni by addition of $\text{Ni}(\text{NO}_3)_2(1\%)$ solution while continuing the etching process for another 1 minute.

3. Characterization methods

The morphological characterization of the deposited substrates were carried out by SEM. Chemical analysis of surface was performed by Auger Electron Spectroscopy (AES) with Ar^+ ion sputtering (09-IOS-10), IR-spectroscopy (IKS-29) and X-ray diffraction. Porous silicon photoluminescence spectra were investigated using time-resolved spectrometry carried out at room temperature.

Standard methods of I-V and C-V (1 MHz) measurements were used for electrical characterization of elaborated structures. For this, a $0.1\text{—}0.2\ \mu\text{m}$ layer of Pt was deposited thermally at $10^{-5}\ \text{Pa}$ to form mesa-structures of 1 mm diameter. A Pt ohmic contact on rear side of Si wafer was formed by thermal deposition.

3.1. Characterization of porous Si(Ag)-Si

In the $\text{AgNO}_3+\text{H}_2\text{O}$ solution, the silver is not precipitated on the Si slab. The morphology of the PS surface after Ag chemical precipitation in $\text{HF}+\text{HNO}_3+\text{AgNO}_3$ is characterized by the presence of the nanoclusters of semispherical shape. They correspond to the silver nucleation centers (Figure 4.2). The rise of the deposition time leads to the growth of the silver nucleation centers and increase of the surface-roughness. The time of chemical silicon treatment for the formation of the pore depth $d=1\text{—}2\ \mu\text{m}$ is 30—60 sec. At larger time treatment, the silver is deposited as continuous layer. AES results of the Si surface are presented in Figure 4.3. As shown, the increase of the treatment time stipulates the growth of the depth penetration of Ag atoms into the substrate. The concentration of oxygen in the Si bulk is insignificant and does practically not depend on the treatment time.

The detail morphological study and AES observation show that Ag nanoparticles gradually sink into the bulk of silicon. The sinking behavior of the Ag nanoparticles is clearly observed in a TEM analysis. Si nanoparticles with diameters of 5—120 nm are presented.

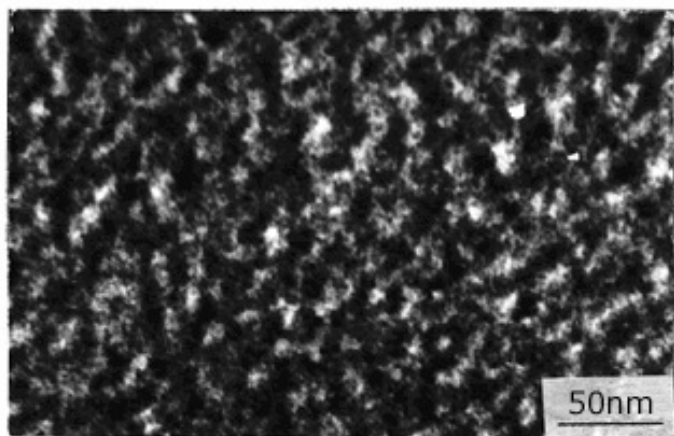


Figure 4.2

SEM observations of silver modified porous silicon.

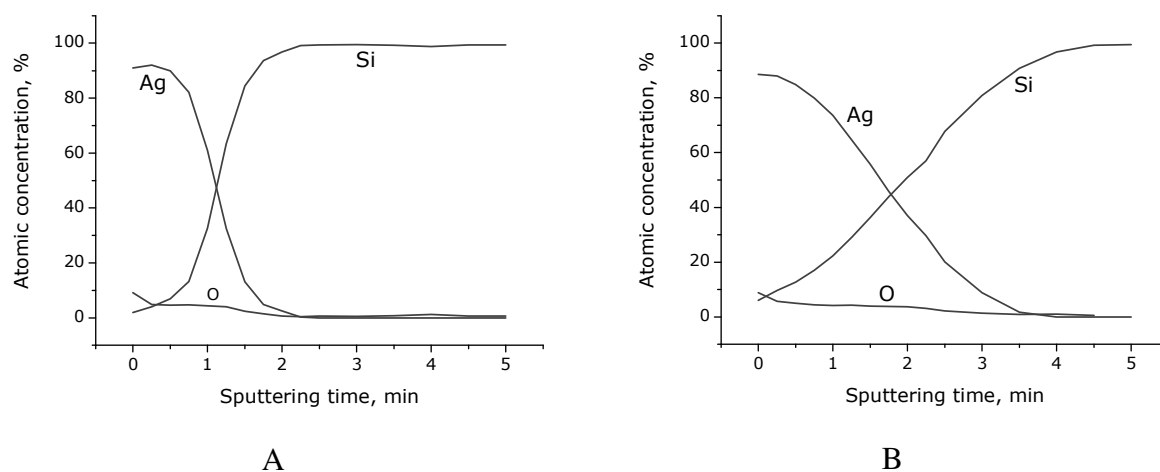


Figure 4.3 Atomic concentration of Ag, Si, O versus sputtering time. Porous Si(Ag) was formed for 20 s (A), and 40 s (B).

3.2. Characterization of porous Si(Pt)-Si

The treatment in the mentioned solution results in the Pt nucleation on Si surface. SEM images show grains of the semi-sphere shape that is related to Pt nuclei (Figure 4.4). Pt ions act as oxidizing agent of Si. Fluorine species act as complexing agent of Si oxidation products. During the treatment, the concentration of soluble metal ions decreases and, simultaneously, the Si wafer is etched. The process of nuclei generation expands during the treatment, causing the increase of surface roughness. After of 30—60 min treatment, the nuclei grains have a typical dimension up to 100 nm. In contrast, the surface exhibits irregularities of nanometer-range size on the etching in the diluted solution of HF (20%) without Pt salt.

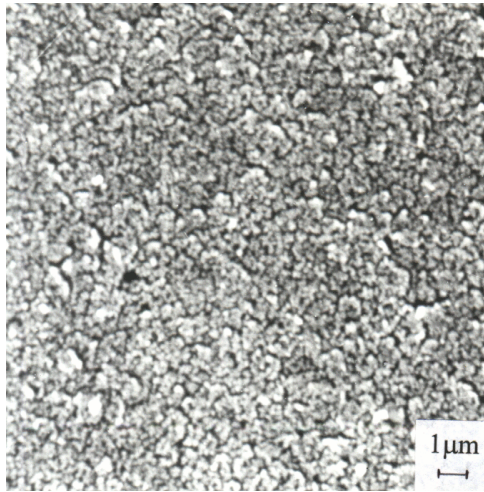
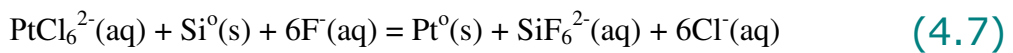


Figure 4.4

SEM of Si surface after 60 min of the electrolytic deposition of Pt.

The deposition process is presented as the following:



In other words, the Pt deposition process can be considered as two half-cell electrochemical reactions: the cathodic Pt reduction and anodic Si oxidation processes occur simultaneously on Si surface and exchange the charge carriers via the Si substrate. Fluorine ions in solution not only prevent the creation of the silicon oxide, but dissolve the Si skeleton to soluble complex of SiF_6^{2-} (4.7).

The formation of Pt nuclei is correlated to the Si etching process in the surrounding regions. Silicon etching and metal deposition is initiated on surface defects (scratches, impurity contamination, Si steps, etc.). The Auger electron spectroscopy (AES) profile of Pt, O and Si atoms near the treated surface is presented in Figure 4.5. The increase of treatment time improves the penetration of Pt into Si substrate.

IR absorption spectra show that the as-treated surface is covered by hydrogen species, having the very weak IR absorption peaks in $2000\text{--}2200\text{ cm}^{-1}$ range. These species can modify the chemical reactivity of Pt/Si surface.

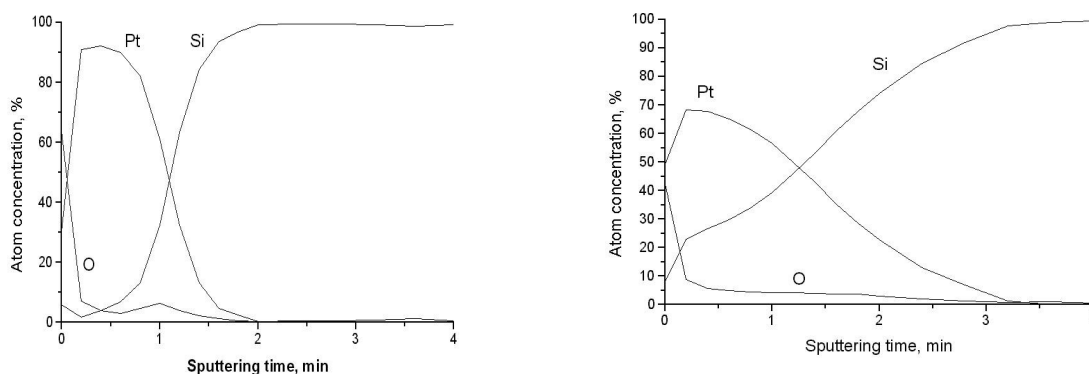


Figure 4.5 Atomic concentration of Pt, O, Si at 30 (a) and 60 (b) min treatment. The sputtering velocity is $\sim 100\text{nm/min}$.

The chemical deposition of Pt from HF solutions forms a dielectric layer on Si substrate with a thickness up to hundred of nanometers. The deposition process is accompanied by the formation of Pt nuclei that accelerate the selective Si etching. At large deposition times in HF solution the saturation of Si surface with hydrogen is observed which limits the chemical reactivity of the surface. Pt covers compactly the Si surface. The 3–60 min chemical treatment allows to form the potential barrier of Schottky type on developed Si surface. From the analysis of I-V and C-V characteristics, the main parameters of interface dielectric layer and Schottky barrier were defined.

3.3. Characterization of porous Si(Ni)-Si

Samples prepared without metal nanoparticles manifest a visible luminescence with a maximal intensity at 650–725 nm band (Figure 4.6) which corresponds to S-band [129, 130]. The PL of porous silicon with Pt and Ag nanoparticles was much less pronounced due to increasing nonradiative Schokley-Read-Hall recombination, and become degraded very quickly. So, we focused our work on porous Si(Ni).

The samples with Ni nanoparticles display the same PL spectra as porous silicon formed by routine electrochemical or chemical etching (Figure 4.6). However, the intensity of porous silicon samples formed in $\text{HF}+\text{HNO}_3+\text{Ni}(\text{NO}_3)_2$ or in $\text{HF}+\text{HNO}_3$ followed by etching in $\text{HF}+\text{HNO}_3+\text{Ni}(\text{NO}_3)_2$ shows much less intensity than “pure” stain etched porous silicon samples. Moreover, the intensity of samples with Ni nanoparticles very quickly degrades under UV irradiations in the first few minutes (Figure 4.6). The storage of the stain etched samples in ambient atmosphere leads also to strong PL degradation independently from the presence of metal nanoparticles (Figure 4.7).

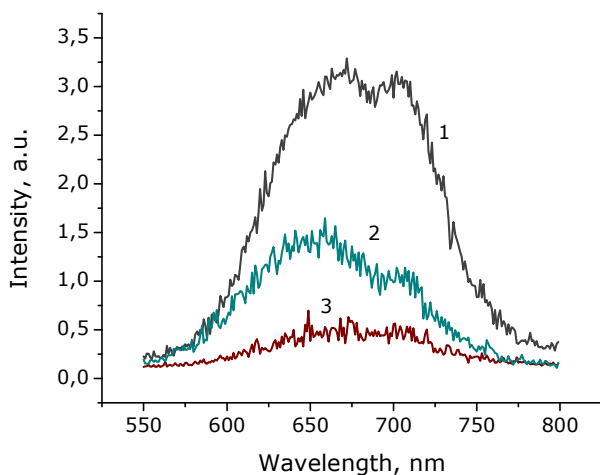


Figure 4.6

The PL of PS prepared in the following solutions: HF+HNO₃ (1), HF+HNO₃+Ni(NO₃)₂ (2), HF+HNO₃, followed by in HF+HNO₃+Ni(NO₃)₂ (3) after 10 min since beginning of UV illumination.

Intensity and lifetime measured for porous silicon with and without Ni deposition display a dependence on pH of buffer solutions, but in different extent (Figure 4.7 and Figure 4.8). For both types of samples, a constant degradation of porous Si layer takes place due to oxidation process and porous Si etching in basic solutions.

In the PL spectra, the channels of fast non-radiative recombination conditional by nonsaturated broken bonds on Si surface can be passivated by ions of hydrogen, oxygen and hydroxyl groups. The passivation by metal is possible as well [130]. The role of metals can be manifested in the saturation of broken bonds and activation of oxidation processes that should increase the intensity of S-band of PL. It is known that the broken Si bonds are the drain for fast diffusive atoms of transient metals (Au, Ag, Pt, Pd, Ni, Cu) and gettering centers for oxygen that is collected on defects and creates the oxygen precipitations [131]. From the other hands, our DLTS data (chapter 5 of this thesis) [132, 133] show that the quantum confinement effects in porous silicon can create quasi continuous localized states in band gap that act as electron or hole traps. These traps increase the nonradiative Schokley-Read-Hall recombination. The observed states display the quasi continuous spectrum having the activation energy from 0.032 to 0.4 eV (from thermally stimulated luminescence [134]). The observed fast PL degradation of porous silicon at the metal (Pt, Ni, Ag) doping gives the evidence of the preference of increasing of Schokley-Read-Hall recombination in comparison with passivation effect. Nevertheless, the difference in behavior of porous silicon PL with and without metal nanoparticles can be applied to create the matrix of gas or bio-sensors.

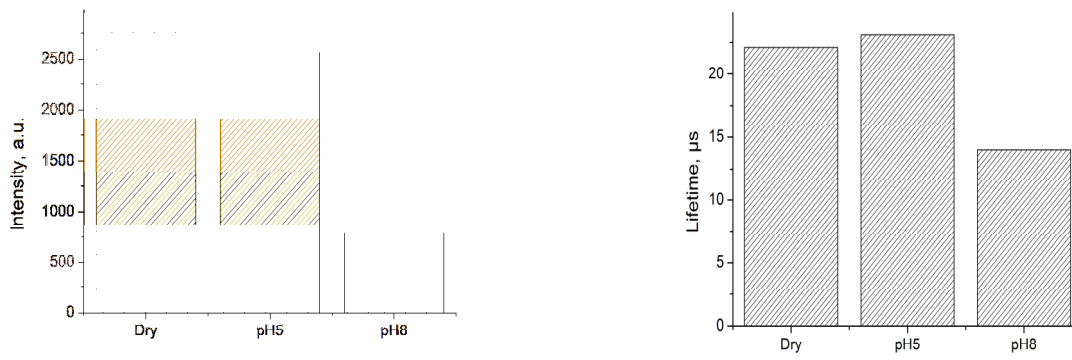


Figure 4.7 Intensity and lifetime measured for porous silicon with Ni deposition

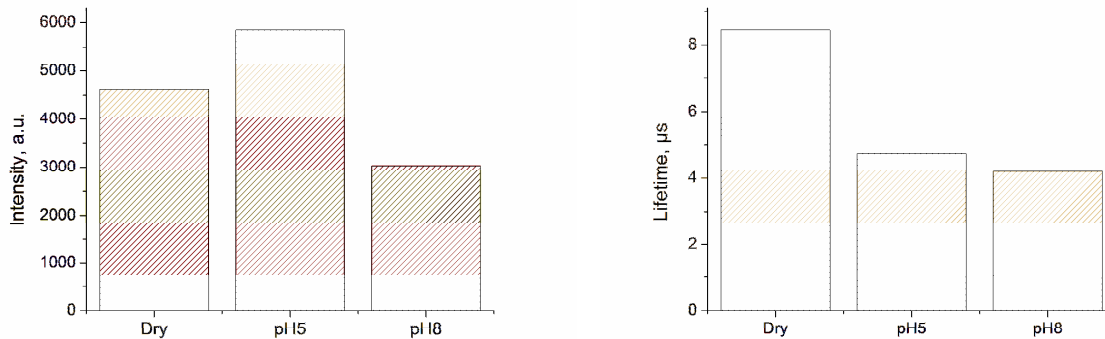


Figure 4.8 HF:HNO₃ etched porous silicon treated in different buffer solutions

4. Characterization and analysis of Pt-p-Si structures

4.1. C-V characterization

The C-V characteristics of contact Pt-p-Si structures display a behavior typical for metal-semiconductor potential barrier having an interface dielectric layer (Figure 4.9, A) [120]. In the region of high forward applied voltages ($eV \gg e\phi_b$), the capacity of the structure does not depend on the applied voltage and is determined by the capacity of the interface dielectric layer C_1 between the metal and the silicon. The longer electroless Pt deposition, the less of total capacity, and C_1 as well is observed. At the long-continued deposition ($t > 30$ min) the total capacity is defined by the capacity of the dielectric layer. Thus, the C-V curves change from a Schottky-type (when C^{-2} is a linear function of V) to a dielectric layer-type (the capacity slightly depends on applied voltage).

The total capacity consists of the series connected capacities: the capacity of a

Schottky barrier $C_2 = \sqrt{\left(\frac{e\epsilon_0\epsilon_2N_p}{2(e\phi_0 - eV_2)}\right)} \cdot S$ and the capacity of dielectric layer $C_1 = \frac{\epsilon_0\epsilon_1S}{d}$,

here ϵ_1 and ϵ_2 are of dielectric constants of interface layer and Si, N_p is doping level in Si, $e\phi_0$ is potential barriers, V_2 is the voltage drop on space charge region of Si, d is the thickness of interface layer, S is the surface area.

Such approach permits to determine the potential barrier height $e\phi_b = e\phi_0 + E_f$ knowing the total capacity C_0 at $V=0$ and the capacity of interfacial layer C_1 [135]:

$$\phi_0 = \frac{1}{2}\epsilon_0\epsilon_2N_pS^2(C_0^{-1} - C_1^{-1})^2 \quad (4.10)$$

Knowing the value of Fermi energy of 0.2 eV for studied Si slab and experimental values of capacity C_0 and C_1 , we can calculate the potential barrier $e\phi_b$, which fully lies in the range of 0.26—0.3 eV. For contact structures before treatment or for the short time electroless deposition, the substrate doping level in the space charge region is defined from the slope of $C^{-2} = f(V)$ curve, and is equal $N_p=3.10^{15} \text{ cm}^{-3}$ (Figure 4.9, B, curve 1). After long time electroless deposition, the dependence $C^{-2} = f(V)$ is not fitted by linear approximation, which shows the inhomogeneous distribution of doping impurities in the surface layer.

4.2. I-V characterization

The I-V curves of the elaborated structures also exhibit a typical behavior of metal-semiconductor type Schottky contact that has a dielectric interface layer (Figure 4.10). The ideality factor β lies in the range of 1.3—1.5 at small forward V . The increase of the time of electroless deposition ensures the decrease of both forward and reverse currents. Moreover, the dependence of $\ln I = f(V)$ for all forward applied voltages is not fitted by linear approximation. It indicates the dominant role of interface layer for current transport. The calculation of series specific resistivity of interface layer from I-V curve at large applied voltage gives a value of 10^2 — $10^3 \text{ } \Omega \cdot \text{cm}$. The value of potential barrier defined from temperature dependence of saturation current I_s can be written as $\phi_b = (kT/e)\ln(\hat{A}T^2S/I_s)$ [136] and equals to 0.25—0.28 eV coinciding with that calculated from C-V data.

4.3. Dielectric constant and thickness estimation

The analytic expressions for β and C_1 can be applied to determine the dielectric constant and thickness of the interface layer [136]:

$$\epsilon_0 \epsilon_1 = (e / \beta k T) (e C_1 / \pi S)^{1/2} \quad (4.11)$$

$$d = (e / \beta k T) (e S / \pi C_1)^{1/2} \quad (4.12)$$

The results are presented in Figure 4.11 and Figure 4.12. At short time of treatment the interface grows linearly, further this dependence is described by a $d \sim t^{1/2}$ law typical for diffusion processes. To compare, Figure 4.5 shows the depth of Pt penetration into substrate obtained from AES data. The value of dielectric constant ϵ_1 , which is averaged along the entire dielectric layer, was calculated from AES data [136] and presented in Figure 4.12. One of the reason of small value of ϵ_1 comparing with Si substrate, is due to the porosity of the interfacial layer. If the porous layer is considered as mixture of Si and air, then $\epsilon_{PS} = (1-P)\epsilon_{Si} + P\epsilon_{air}$. The alteration of ϵ_{PS} in the range of 8—5 changes the porosity within 0.33—0.62.

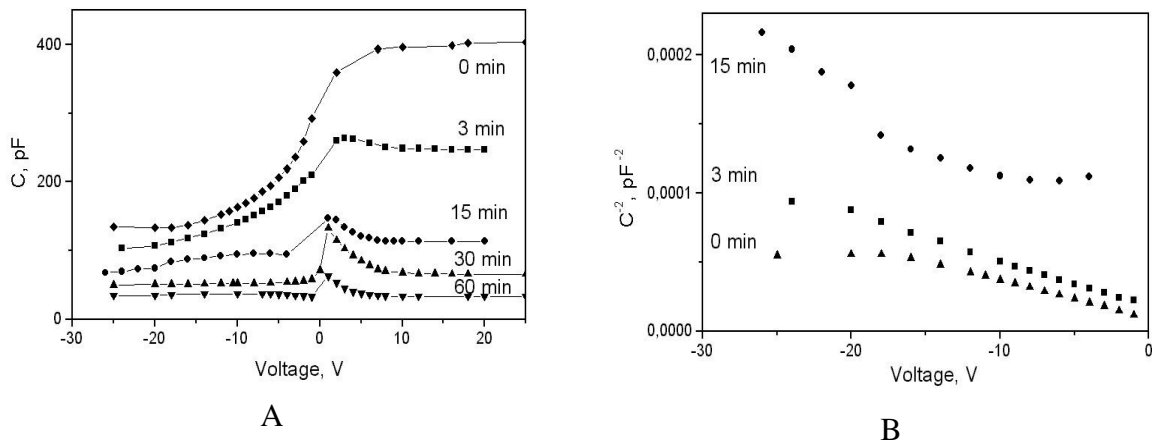


Figure 4.9 The C-V curves of contact structures Pt/Si at different times of electroless deposition.

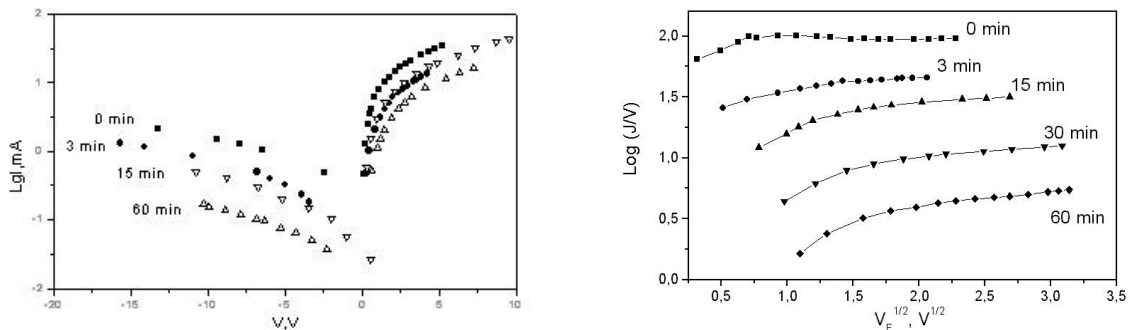


Figure 4.10 The I-V curves of Pt-Si structures versus time of electroless deposition

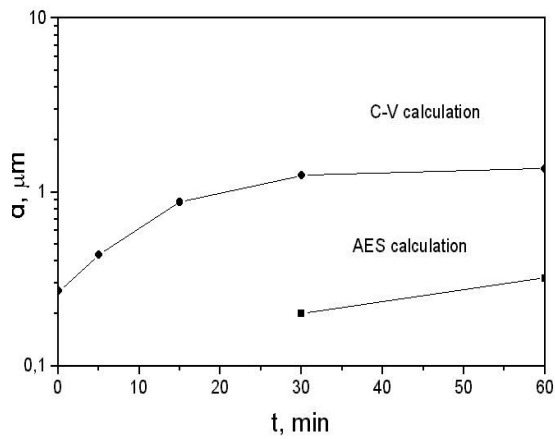


Figure 4.11

The thickness of dielectric layer versus time of electroless deposition.

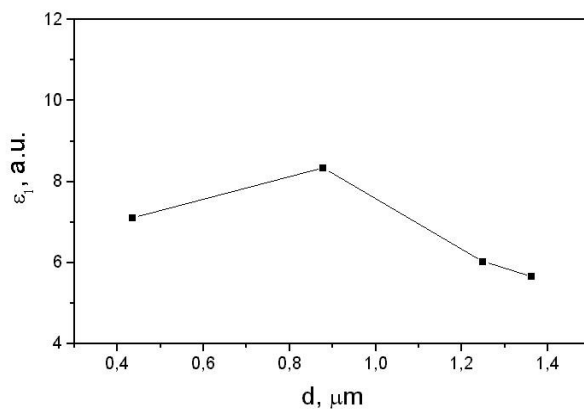


Figure 4.12

The dielectric constant of interface layer as function of layer thickness for Pt-Si structure.

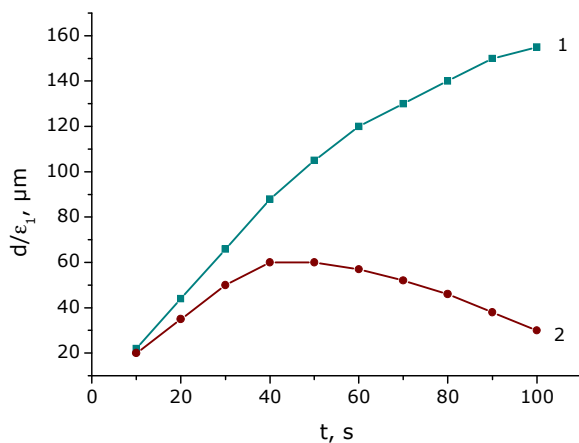


Figure 4.13

The change of dielectric layer thickness with the time of chemical treatment: without AgNO_3 (1), with AgNO_3 (2).

The results of the determination of the intermediate dielectric layer thickness at metal-semiconductor interface in the Ag-PS-pSi structures using capacitance-voltage measurements are presented in Figure 4.13. The porous silicon thickness increases after chemical treatment in the solution without AgNO_3 . The initial linear growth is slowed at the increase of the duration of the chemical treatment and it approaches to the dependence typical for diffusion processes: $d \sim t^{1/2}$. The presence of AgNO_3 in the solution leads to the decrease of

the effective thickness of the intermediate dielectric layer at the growth of treatment time that is stipulated by the increasing penetration of Ag atoms into the porous silicon layer.

5. Conclusion and perspectives

We have been successful in incorporating Ag, Pt and Ni. The introduction of these metals into the pores is easily combined with the chemical formation of porous silicon, in particular, by stain etching with hydrofluoric and nitric acids. We have determined the concentration profile for the Ag and Pt deposition. Regarding possible future application of these structures for sensors we can note that only porous Si with Ni manifests PL but with high degradation towards UV irradiation. Porous Si with Pt shows more promising behavior for implementation in electrical sensors as it was demonstrated I-V and C-V measurements.

One potential application of this work could be the detection of DNA by Surface Enhanced Raman Scattering (SERS) technique [137], which is a non-labeling technique.

Overcharging of Porous Silicon Localized States at Gas Adsorption

The behavior of localized states in Pt / nano- or mesoporous Si / p-Si heterojunctions is studied by Deep Level Transient Spectroscopy (DLTS) in vacuum and different atmospheres: ambient air, Ar, N₂, CO₂, O₂. Complex DLTS spectra of both signs related to electron and holes traps in porous Si are detected. The intensity of DLTS peaks and activation energy is shown to be dependent on the morphology of the porous layers and also on ambient atmosphere in which measurements were carried out. The shift of the activation energy with the increase of the applied reverse voltage is interpreted from the point of view of a spatially inhomogeneous distribution of localized states in the porous layer. The cyclic transformation of DLTS spectra is observed for consecutive measurements in vacuum and ambient atmosphere. Oxygen adsorption (at partial pressure of a few mbar) results in strong passivation of deep traps in mesoporous Si.

The material of this chapter is published in [132].

1. Introduction

Elaboration of electronic devices based on porous Si requires a thorough knowledge of energy parameters of the localized states in the porous layers. The Deep Level Transient Spectroscopy (DLTS) is a useful tool to analyze the parameters of deep traps in semiconductor structures as well as the dynamics of charge carriers emission-capture processes. This method has been successfully applied to the study of quantum wells [138], quantum dots [139], multilayer heterojunctions [140], etc. Nevertheless, there are not so many

works devoted to the DLTS of nanocrystalline and porous Si [133, 141], since there are some difficulties in the interpretation of complex relaxation spectra of nanocrystalline semiconductors with quasi-continued sub-bands of localized states in the energetic gap [134, 142].

In this work we present the study of the DLTS spectra of Pd/Si heterojunction with nanoporous and mesoporous Si interfaces in different ambient gases (CO₂, N₂, Ar, and O₂). The effects of molecule adsorption/desorption on localized states in porous Si are interpreted by the analysis of DLTS curves (peak intensities and activation energies). Our main objective of this study is to find the influence of gas adsorption on the porous Si localized states concentration and emission properties.

2. Principle of DLTS

DLTS is a high frequency (MHz range) junction capacitance measurement technique that uses the capacitance of a p-n junction or a Schottky barrier to monitor the charge state of the traps. By the proper choice of experimental parameters, DLTS allows to measure the thermal emission rate, the activation energy, the concentration profile, and the capture rate of each trap [143-145]. The presence of each trap is indicated by a positive or negative peak on a flat baseline plotted as a function of temperature. The height of the peak on this plot corresponds to the traps concentration. The sign of the capacitance change depends on whether the electron occupation of the trap had been increased or decreased by the injection pulse. An increase in trapped minority carriers causes an increase in the junction capacitance. The deep level traps charge-discharge process for the case of p-doped silicon can be illustrated as followed (Figure 5.1):

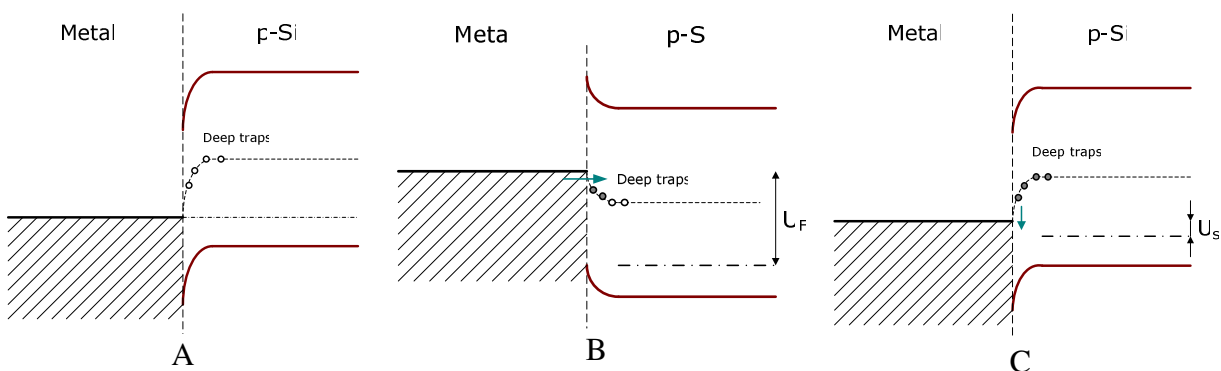


Figure 5.1 Metal-(p-doped) semiconductor contact.
 A. Schottky barrier with no external bias;
 B. Strong positive bias (traps charging);
 C. Small positive bias (traps discharge).

At the contact of the metal with the semiconductor, a Schottky barrier is formed (Figure 5.1, A). The application of a strong forward bias leads to the filling of deep levels

with charge carriers (Figure 5.1, B), which is manifested in the increase of the barriers capacitance. Further application of weak forward or inverse biasing (Figure 5.1, C) leads to the gradual deep levels discharge, and so to the decrease of the barrier capacitance. The discharge rate is defined by the deep level energy, as well as by the semiconductor temperature.

In the DLTS method considered, the overcharging of single deep level in energy band gap is described by an exponential law as follows:

$$N_i^+(t) = N_i \left[1 - e^{-\frac{t}{\tau}} \right] \quad (5.1)$$

where $\tau = (N_v \gamma_p)^{-1} e^{\frac{E_i + E_v}{kT}}$ for p-type semiconductor, N_i and N_i^+ are the concentrations of charge carriers on the deep level before and after their releasing; N_v is the density of states in v -band; γ_p is the coefficient of hole capture; E_i is the activation energy; E_v is the top of the v -band.

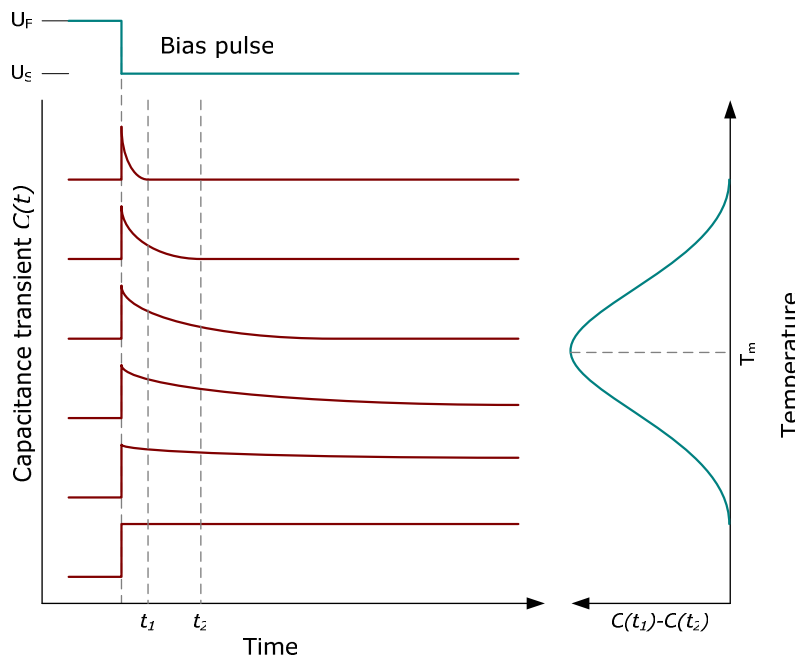


Figure 5.2

The barrier capacitance transient $C(t)$ measured at fixed discriminator times t_1 and t_2 as a function of temperature (DLTS spectrum).

A discriminator is used to record the capacitance transients. The signals from different deep levels are selected by the discriminator which sets the rate of the charge carriers emission and trapping by separating the capacitance relaxation with fixed τ . The discriminator measures the relaxation signal in the different fixed times t_1 and t_2 . It gives the output signal in $C(t_1) - C(t_2)$ format (Figure 5.2). The latter is maximal when the time constant τ equals to $(t_1 - t_2) / \ln(t_2 / t_1)$. During the heating of the sample, the high temperature peak T_m arises on the curve of $C(t_1) - C(t_2)$ versus temperature for deeper level E_i . The peak corresponds to the temperature at which the capacitance relaxation is characterized by the time constant τ .

$$\ln(\tau \cdot T_m^{-2}) = -\ln(\sigma_p b_p) + \frac{E_i + E_v}{kT_m} \quad (5.2)$$

where T_m is the temperature of the DLTS maximum; σ_p is the cross-section of hole capture; b_p is the coefficient. The equation (5.2) represents the straight line (Arrhenius plot) of a function $\ln(\tau \cdot T_m^{-2}) = f(1/T_m)$ with slope amounts to the energy position E_i . The intersection of Arrhenius plot with Y - axis is the cross-section of the charge carrier capture.

3. Experimental

Layers of nanoporous and mesoporous Si have been formed on boron-doped p-Si (100) (resistivity is $10 \Omega \cdot \text{cm}$) and p^+ -Si (100) (resistivity is $5\text{--}10 \text{ m}\Omega \cdot \text{cm}$), respectively. The porous layers were grown by anodization process in a solution of 48w.%HF:C₂H₅OH in proportion of 1:2. Current density was 20 mA/cm^2 (to form nanoporous Si) and 100 mA/cm^2 (to form mesoporous Si). The thickness of the nanoporous and mesoporous Si layers is $100\text{--}150 \text{ nm}$ and $2\text{--}3 \mu\text{m}$, respectively. As-prepared nanoporous layers manifest typical red-orange photoluminescence at room temperature while being excited by UV lamp.

Barrier structures of 1 mm in diameter were formed by deposition of non-transparent Pd layer through a metal mask on the porous Si surface in high vacuum at 200°C . Metal deposition at this temperature provokes partial hydrogen desorption from as-prepared porous Si layers. This is clearly manifested by the photoluminescence quenching of nanoporous Si. However, the following DLTS measurements, performed within $100\text{--}450 \text{ K}$ temperature range, does not revealed the significant change of electrical properties. The metal film covering produces the built-in potential in heterojunction (which is required for transient capacity technique) and prevents porous silicon surface oxidation during exposition in O₂ or ambient atmosphere. An ohmic contact on the rear side of the substrates was created through electrochemical deposition of a thick Ni film. The electroluminescence of finished heterojunctions was not observed.

The structure was placed in a liquid nitrogen cryostat connected to a gas supply system. A depletion region width in barrier structure at the presence of a steady reverse bias is defined. A rectangular pulse of forward bias $U_F \geq 0 \text{ V}$ results in the depletion region narrowing, and the junction capacitance increases when majority carriers are trapped. The pulse of reverse bias U_S leads to decrease of capacity below its initial value (the depletion width and barrier capacitance defined by the amount of charge inside the space charge region) and observe the exponential capacity decay by thermal emptying of traps filled by the majority carrier pulse.

The peak magnitude of the measured sample capacitance reaches 300 pF, the minimum of the measured capacitance relaxation is 10^{-4} pF that corresponds to the maximum of sensitivity of $dC/C = 3 \cdot 10^{-7}$. It allows evaluating of deep levels concentration beginning from 10^8 cm^{-3} at the presence of 10^{14} cm^{-3} shallow levels.

For the structures elaborated, we determined the optimal parameters of DLTS spectra observation: 1) the emission windows are selected in 23 — 10000 μs range; 2) the temperature alters from 70 to 450 K; 3) $U_F=0$ — 1.0 V, the larger U_F , the bigger DLTS signal is observed up to the saturation at $U_F > 1.0$ V when the total filling of electronic traps occurs; 4) $U_S = 0.2$ — 2.5 V.

4. Experimental results

First of all it was observed that Pd/p-Si barrier structures do not show any detectable relaxation signal, while the Pd / porous Si / p-Si structures manifest complex DLTS spectra for both nano- and mesoporous Si interfaces. In the case of nanoporous Si interface, these spectra can be fitted by at least two Gaussian curves with activation energy E_1 и E_2 (Figure 5.3).

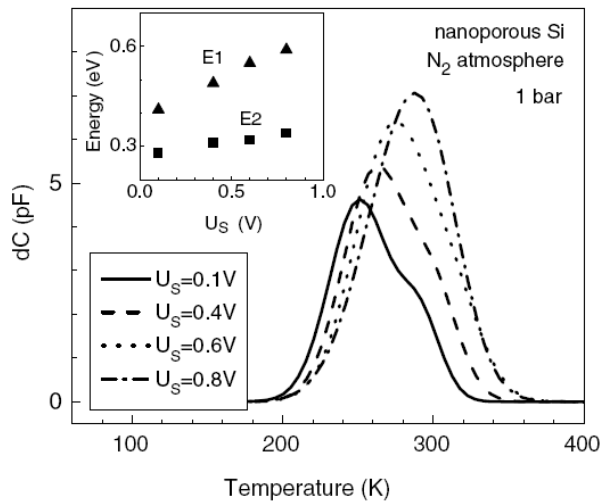


Figure 5.3

The DLTS spectra of nanoporous silicon at different reverse voltages in N_2 atmosphere. The inset shows the dependence of activation energies on U_S .

As it was noted in [133], the shape and intensity of DLTS curves depends strongly on nanoporous Si thickness. For example, for thinner nanoporous Si layers dried in N_2 atmosphere, additional peaks of negative sign are observed [133]. For the investigated samples, the additional peak of negative sign was less pronounced and not observed for all samples. It is well known, that the sign of the capacity relaxation value depends on the type of captured carriers and material conductivity type [144]. In the figures presented, the positive DLTS peak corresponds to holes traps and the negative one to electrons traps associated with porous Si.

The measured capacity is governed by the applied reverse bias since the increase of U_S leads to a widening of space charge region in the semiconductor and the increase of total charge on the detected traps (Figure 5.3). Moreover, the activation energy, defined by (5.2), for nanoporous Si in N_2 increases with U_S growth. So, the values of E_1 and E_2 amount to 0.42 and 0.28 eV, respectively, at $U_S = 0.1$ V and to 0.59 and 0.34 eV, respectively, at $U_S = 0.8$ V (Figure 5.3, the inset). The peak intensity from deeper trap grows faster with reverse voltage applied.

The positive DLTS peaks of mesoporous Si in vacuum, inert gas or at small oxygen pressure are observed too and can be fitted, at least, by one Gaussian with activation energy that depends on U_S : $E_1=0.62$ eV ($U_S=0.2$ V) and 0.8 eV ($U_S=2.5$ V). At $U_S > 1.0$ V, the peak of negative sign is arisen in spectra, which related to electron traps in porous Si (Figure 5.4). Intensity of this peak increases too with U_S growth.

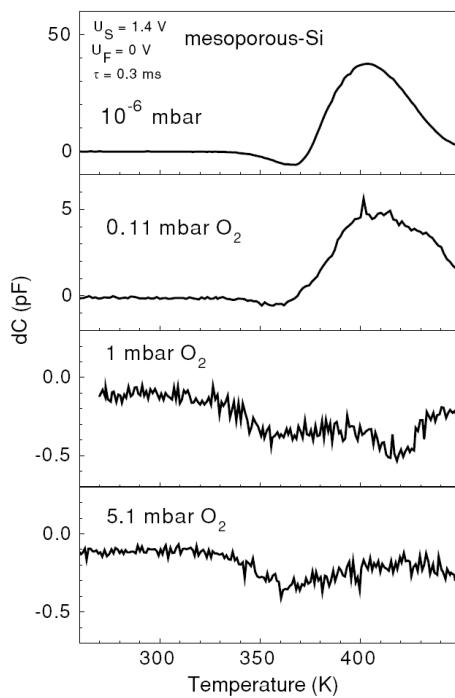


Figure 5.4

DLTS spectra of mesoporous silicon at several oxygen partial pressures.

Figure 5.5 represents DLTS spectra in different atmospheres. As can be seen, the DLTS curves of nanoporous Si are narrowed and shifted to higher temperatures in atmosphere of CO_2 , Ar and O_2 compared to vacuum conditions.

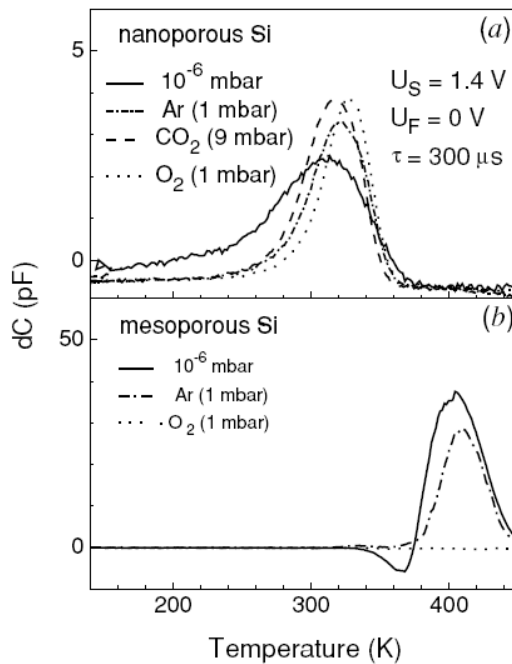


Figure 5.5

DLTS spectra of nanoporous and mesoporous silicon in vacuum (10^{-6} mbar), Ar (1.1 mbar), CO₂ (9.1 mbar) and O₂ (1 mbar).

The same result in shifting of DLTS peak to higher temperature is observed after supplementary annealing at 450 K in vacuum conditions (Figure 5.6). Firstly, after keeping in ambient air during 10 min, the sample was measured in vacuum (Figure 5.6, curve 1), hold in vacuum during 10 min at 450 K and was measured once again in 200—450 K temperature range (Figure 5.6, curve 2). The coincidence of DLTS curves are observed at cycling of these measuring conditions (Figure 4, curves 3 and 4).

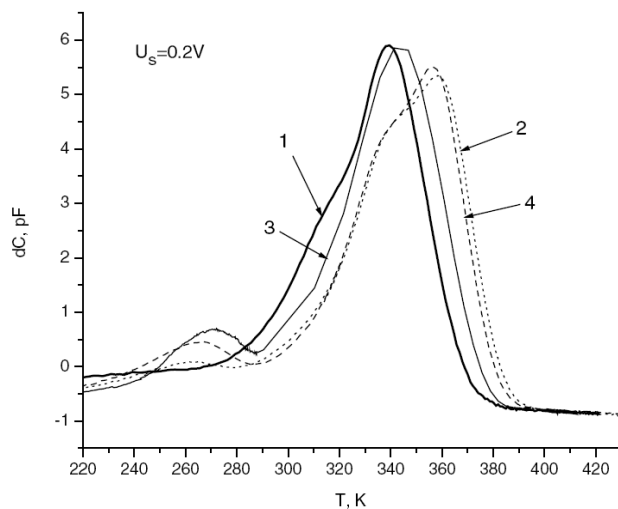


Figure 5.6

The transformation of DLTS spectrum of nanoporous silicon at the subsequent change of gas atmospheres: 1, 3 — measurement in vacuum after 10 minutes of keeping the sample in ambient air; 2, 4 — measurement in vacuum after 10 minutes of annealing at 450 K.

The behavior of DLTS curves of mesoporous Si in different atmospheres is similar to nanocrystalline Si. It should be mentioned the special case of oxygen atmosphere. At oxygen pressure of 0.1 mbar, the DLTS spectrum is similar to one in vacuum of 10^{-6} mbar. At partial oxygen pressure of 1 mbar, the positive peak fully disappeared and only negative two peaks are reiterated. At partial oxygen pressure of 5 mbar, the high temperature negative peak from deeper trap is suppressed (Figure 5.4).

5. Discussion

The important problem related to the interpretation of results stated above, is that the capacitance relaxation model, based on single deep trap approximation (5.1), roughly describes the behavior of complex porous Si spectra. However, the intensities of DLTS peaks and activation energies are defined with acceptable accuracy and give useful information about deep traps behavior of porous Si in gas atmosphere. The second point is the space attachment of deep traps in porous Si. Generally, they may exist on a huge internal surface of porous layers and in the interfaces between the porous Si layers and Pd film or Si substrate. Since no DLTS signals have been observed for the Pd/Si junction, the detected deep traps are related to the existence of porous Si, namely.

Following the results of the previous work [134], we assumed that the deep traps are distributed in a broad sub-band of energy gap of porous Si. Under such approximation, the activation energy should be changed with applied reverse bias according to deep traps filling. In the model of nanoporous Si/Si heterojunction with varying band gap of the nanoporous layer, the increase of U_S leads to the widening of the depletion region in p-Si as well as the growth of the voltage drop on the nanoporous Si layer. This means that the deeper traps inside the nanoporous layer are involved into the relaxation process as well as the surface states at the porous Si/ Si interface. Then the shift of the activation energy with increasing U_S can be also interpreted from the point of view of a spatially inhomogeneous distribution of deep traps in the nanoporous layer.

In order to explain the influence of different gas atmospheres on the DLTS spectra, the possible adsorption-desorption processes on the nanocrystalline surface should be considered. For example, porous layers effectively adsorb molecules of water, CO_2 and others while being exposed to the ambient atmosphere for a long time [17]. Adsorption of polar molecules supplies supplementary charges on the surface of Si nanoparticles that is compensated by charged acceptors or donor states inside the of porous Si layers. The formation of double charge layers creates a supplementary reverse shift, i.e. the behavior of the relaxation curve at adsorption is similar as in the case of U_S applying. For example, considering nondissociative water adsorption, the DLTS spectrum shifts to higher temperatures in humid air in comparison with the samples under vacuum condition [146].

On the other hand, the adsorption equilibrium for different kinds of molecules also depends on other molecules in the surrounding atmosphere (competition for adsorption places). The adsorption of Ar, CO_2 and O_2 molecules leads to the elimination of the part of deep traps with energy E_1 from the recharging process. It is very curious that the acceptor-type deep traps in mesoporous Si layers can be completely excluded from relaxation process at the

adsorption of acceptor type molecules of oxygen. This effect of strong passivation of deep traps of mesoporous Si in oxygen atmosphere is observed if partial pressure of oxygen is about few mbar. The observed processes are reversible since the oxidation of porous Si under metal covering can be neglected. This effect has a good correlation with photovoltage transient data that show the possibilities of the sign change of PV signal of mesoporous Si in oxygen atmosphere [147].

6. Conclusion

The existence of developed structures of holes and electrons traps in energy gap of porous Si is justified by DLTS spectra. The charge exchange between absorbed molecules and localized traps in porous silicon depends strongly on the nature of the adsorbed molecules and the morphology of porous layer, which can be useful for the elaboration of selective chemical and bio- sensors. The DLTS data obtained supply additional information about electronic traps in porous silicon that could be also responsible for porous silicon PL quenching.

Sixth Chapter

Application of Eddy Current Method for Silicon / Porous Silicon Conductivity Monitoring

In this chapter we describe the implementation of eddy current conductometry for porous silicon conductivity monitoring. For the first time this is applied to the measurement of free-standing mesoporous Si electrical conductivity for the contactless sensing of NO₂ gas. The method consists in the recording of induced eddy current at high frequency (30 MHz). Regardless of certain difficulties that we faced in this work, this method manifests interesting opportunities and perspectives.

The material of this chapter was published in [148].

1. Introduction

As it was pointed in the first chapter of this thesis, porous silicon reveals high increase of electrical conductivity in the atmosphere of NO or NO₂ gases and some solvents comparing with an ambient humidity air [67, 70, 149]. This effect is explained by holes injection into porous Si layers full depleted by the charge carriers. This allows to create a sensitive gas sensor especially for NO and NO₂ gases. As far as nitrogen dioxide (NO₂) is a toxic pollutant, the development of such sensors is well justified.

The easiest way to monitor the conductivity of porous Si is to apply a constant voltage to the sample and to measure the corresponding current changes. This approach requires the formation of ohmic contacts in the porous Si layer that should manifest reliability

and stability during aggressive environmental gas operations. Usually, two geometries are used in this case (Figure 6.1):

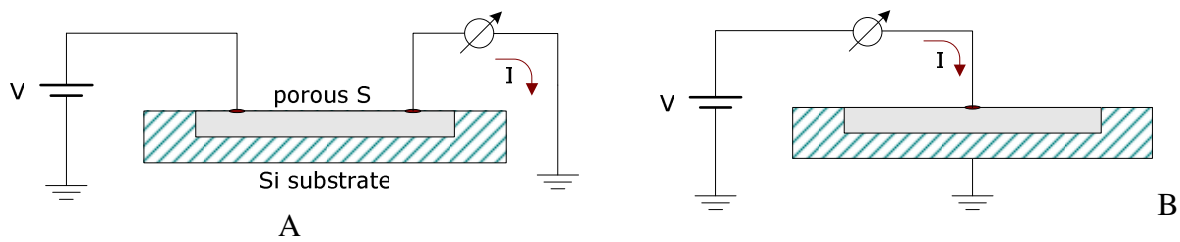


Figure 6.1 Basic circuit configurations for measuring the conductivity of porous Si layer.

The first circuit (Figure 6.1, A) imposes some difficulties in the measurement as far as the silicon substrate shunts the resistivity of the porous Si layer. In this case the monocrystalline silicon substrate should be as thin as possible (compared to the porous Si layer thickness) and should have a rather high resistivity. The second circuit configuration (Figure 6.1, B) is used most often. In this case, the bulk silicon resistance is connected in series circuit with the porous Si layer resistance. So, the Si substrate conductivity should be as high as possible (usually highly doped wafers are used) to assure a good contact first of all, as well as to easily monitor the porous Si conductivity changes on the background of bulk Si conductivity. Therefore we have been interested in developing of conductivity sensors without electrical contacts.

1.1. Eddy currents

Eddy currents (also known as Foucault currents) were discovered by Léon Foucault in 1851. The eddy currents appear when a moving (or changing) magnetic field intersects a conductor. This causes a circular flow of charge carriers (electrons) within the conductor.

Obviously, eddy currents create losses through the Joule heating of the conductive material placed in the changing magnetic flux. So, eddy currents are mostly considered as a negative phenomenon that leads to energy losses. That is why in electromagnetic devices (such as transformers), low conductivity ferrites or a set of thin sheets of magnetic material are used as a core to reduce the eddy current. The loss of useful energy is not always undesirable. For example, eddy currents are used in some practical applications, such as electromagnetic braking systems, induction cookers and nondestructive testing [150]. As far as energy losses caused by eddy current flow are related directly to the conductivity of the material, measuring these losses can be used to estimate this conductivity. This method of conductivity measurement was implemented on metals and semiconductors as well [151]. The

advantage of eddy current conductivity measurement is the possibility to carry out a contactless testing.

In this work we tried to implement contactless eddy current method to control the porous Si sample conductivity change influenced by NO₂ gas adsorption. This means that the sensitive element (porous silicon) can be absolutely isolated from the measurement system by any non-conductive containment.

1.2. Eddy current based conductivity measurement

According to the Faraday's law of induction, the change of magnetic flux leads to the formation of a corresponding changing electric field that can be written by Maxwell equation (6.1):

$$\nabla \times \vec{E} = -\frac{\partial \vec{B}}{\partial t} \quad (6.1)$$

where \vec{E} is the electric field, \vec{B} is the magnetic induction. The electric field causes a current flow if occurred in conductive material. This can be written by generalized Ohm's law (6.2):

$$\vec{j} = \sigma \vec{E} \quad (6.2)$$

where \vec{j} is the current density, σ is the material conductivity.

Actually this \vec{j} is our eddy current induced in the conductive matter by varying magnetic flux. Obviously, the frequency of \vec{j} changes will be the same as for the magnetic field. Eddy current flowing will lead to magnetic field occurrence according to the Ampere's circuital law that can be written by another Maxwell's equation (6.3):

$$\nabla \times \vec{H} = \vec{j} \quad (6.3)$$

This magnetic field \vec{H} will actually resist to the changes of induction \vec{B} . This concurrence leads to the fact that eddy current density will decrease in the depth of the conductive material. This phenomenon is well known as skin effect [152, 153]. The eddy current density in an indefinitely thick plane conductor decreases exponentially with depth z from the surface (6.4):

$$J = J_s \cdot e^{-\frac{z}{\delta}} \quad (6.4)$$

where J_s is a current density at the surface. The value of δ is called skin depth and is defined as follows (6.5):

$$\delta = \sqrt{\frac{2}{\sigma\mu\omega}} \quad (6.5)$$

where μ is the absolute magnetic permeability of conductor, ω is the angular frequency of the magnetic flux change. Such eddy current behavior allows carrying out analysis (conductivity measurement, defectoscopy, etc.) through the sample thickness by varying the induced field frequency [150].

An electric current (eddy current in our case) flowing through a conductive material leads to heat release according to the Joule's first law. Thus, power dissipation in conductor caused by Joule heating can be written as followed (6.6):

$$P_{eddy} = -\frac{dE}{dt} = \int_V \frac{1}{\sigma} \vec{j}^2 dV = \int_V \sigma \vec{E}^2 dV \quad (6.6)$$

where $P_{eddy} = -\frac{dE}{dt}$ is the energy dissipation, V is the volume of integration (actually, the volume where eddy current occurs).

The energy losses caused by eddy current flow can be estimated from the change of Q-factor of inductor's oscillating circuit [154]. According to the definition (6.7):

$$Q = \frac{\omega_0 E_0}{P} = \frac{\omega_0 E_0}{P_{eddy} + P_0} \quad (6.7)$$

where Q is the oscillating circuit Q-factor, ω_0 is the circuit resonance frequency, E_0 is the energy stored in the circuit, P_{eddy} is the energy loss caused by eddy current flow, P_0 is the energy losses caused by other dissipation processes in the oscillating circuit. Thus for the fixed frequency ω_0 , we can write (6.8):

$$\frac{1}{Q} = \frac{1}{Q_0} + \frac{1}{Q_{eddy}} = \frac{1}{Q_0} + \frac{\int_V \sigma \vec{E}^2 dV}{\omega_0 E_0} \quad (6.8)$$

Assuming that we have a homogeneous conductor, so the conductivity σ is just the same for the whole volume of integration, we can finally obtain:

$$\frac{1}{Q} = \frac{1}{Q_0} + \alpha \cdot \sigma \quad (6.9)$$

where α is some constant defined for the particular frequency ω_0 and the conductor geometry (as far as it influences the integration (6.6) region).

2. Eddy current based conductometer

Before implementing the measurement of Q-factor of the LC-circuit with a conductive sample placed nearby, we should make some assumptions. First of all as far as we

are going to work with silicon samples, we will neglect its magnetic properties. So, for the equation (6.5) the value μ will be considered as permeability of free space: $\mu_0 = 4\pi \cdot 10^{-7} \text{ H/m}$. As far as the parameter α of equation (6.9) can depend on the conductivity itself, due to the exponential decay of eddy current density in the depth of the sample, the skin depth δ value should be comparable with the sample depth so that the eddy current density can be considered almost constant in the sample bulk. The inducing magnetic flux should be either homogeneous within the conductor or be absorbed entirely by the sample. So the inducing coil should be either much larger than the sample or much smaller than it. If we do not guarantee these assumptions fulfillment, the resulting measurements will depend on the shape of the sample, its position, and orientation against the inducing coil.

To carry out the experiment a special eddy current detector was designed. This detector includes a 30 MHz high frequency Colpitts oscillator, amplitude detector and differential amplifier (Figure 6.2).

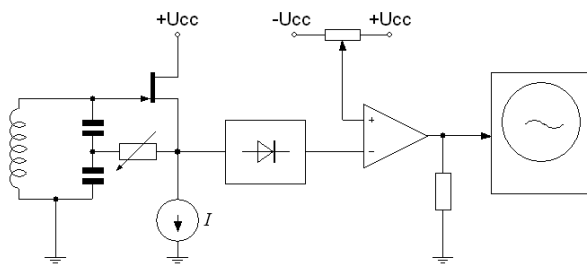


Figure 6.2
Eddy current detector

The LC-circuit of the oscillator was used as the inductor to cause the eddy current flow in the testing sample. The dissipation of energy due to eddy currents in the sample bulk results in the decrease of the Q-factor of the LC-circuit. Due to these losses, the amplitude of generated signal will decrease up to zero if the Q-factor is not high enough to sustain the oscillations in the circuit. The generated signal after detection, biasing and amplification can be monitored by oscilloscope or sampled by ADC. To achieve a higher sensitivity, the generator (Figure 6.2) can be adjusted to operate in oscillation suppression mode by varying the regenerative feedback. In this mode even minor changes of the LC-circuit Q-factor can cause significant changes in the amplitude of the generated waveform.

The inductors coil design was chosen in such manner that the coil dimensions were larger than the typical sample size. This coil had approximately 30 turns of 1.0 mm in diameter copper wire (Figure 6.3).

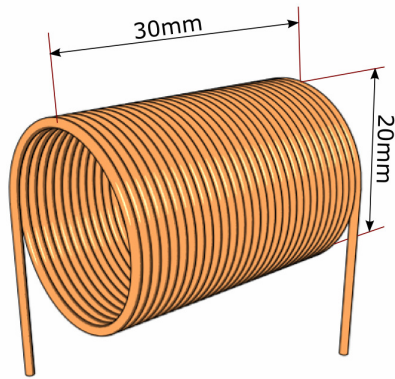


Figure 6.3

Eddy current conductometer inductor coil design view.

Thus, the testing silicon samples can be placed directly inside the coil. As far as the magnetic flux density inside the coil is not uniform, the sample position can have an influence on the output signal of the conductometer. To test the sensitivity repartition, we performed a scan inside the inducting coil with a small piece of conductor. The axial and radial scans of our coil are presented by the following curves (Figure 6.4):

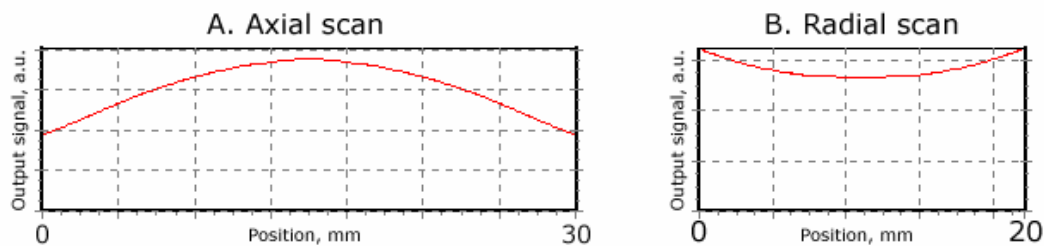


Figure 6.4 Experimental scan of eddy current conductometer sensitivity inside the inducting coil.

The coil scan shows that the most homogeneous area of the sensitivity distribution is in the centermost part of the inducting coil, so the testing sample should be placed in that position. The following figure represents the result of linearity test implemented by placing an increasing number of identical silicon pieces inside the conductometer coil (Figure 6.5). In such manner, we actually vary the number of free carriers that participates to the eddy currents flow which results in an increase of the conductometer output signal.

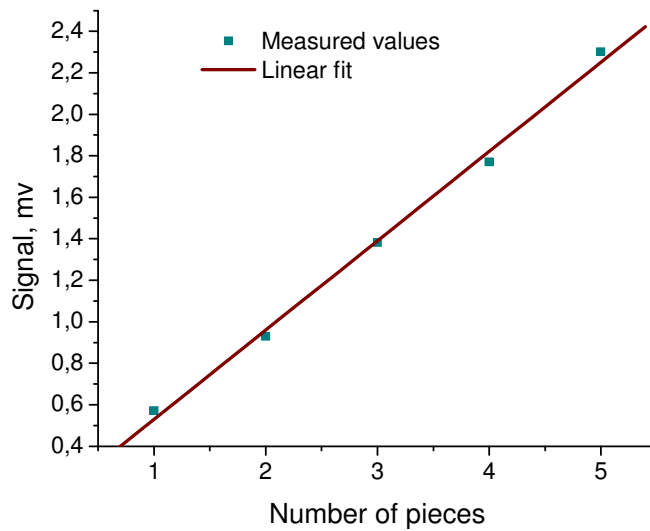


Figure 6.5

Eddy current conductometer output signal versus the number of identical silicon samples placed inside the inducting coil.

3. Detection of NO₂

Finally we tried to detect the change of porous Si conductivity in the presence of NO₂ gas. As sensitive element, we used a thin free-standing mesa-porous Si film formed by electrochemical etching of p⁺-Si (0.01 Ω·cm) in HF-based solution. The free standing film was used in order to eliminate the bulk silicon conductivity. This free-standing film was placed into an air-tight glass cell. The cell itself was placed inside the conductometer oscillator coil (Figure 6.6).

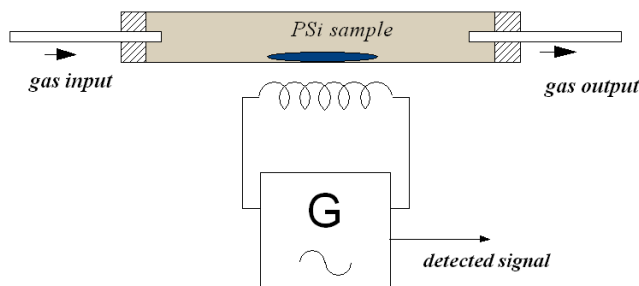


Figure 6.6

Experimental setup for porous Si conductivity changes monitoring during NO₂ injection.

The injected NO₂ gas was obtained by the chemical reaction of nitrogen acid with copper and a further reaction with air in another glass tube. By watching the eddy current conductometer output signal, we tried to determine the change of sample conductivity during the gas injection. The typical response curve is represented in (Figure 6.7).

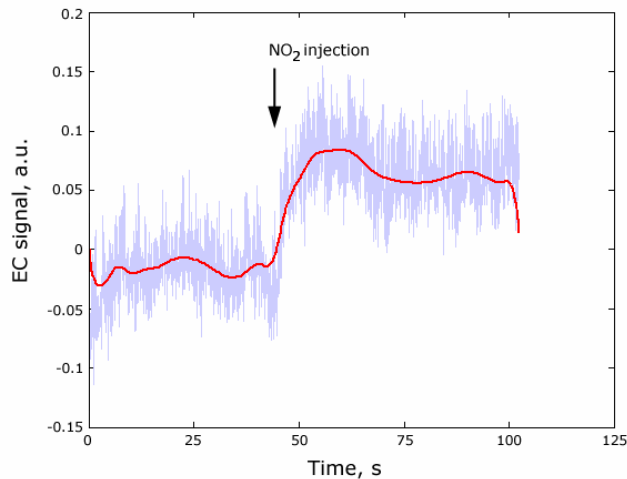


Figure 6.7

Eddy current detector typical output signal (the real signal and filtered one) at the moment of NO₂ gas injection (maximal gas saturation).

So, it was possible to detect the presence of air combined with NO₂. Due to the way that we used to produce NO₂ gas, we could not perform sensitivity analysis. During the experiment we faced some problems. First of all, as far as porous Si conductivity is very low (even in presence of NO₂ environment), the eddy current conductometer had to be adjusted on maximal sensitivity. This resulted in an enormous noise on the output of the conductometer, as far as the inducing generator works in the mode of oscillation suppression, which is very sensitive to the changes of LC-circuit Q-factor, and also very unstable. The other problem is the conductometer response on any conductive material places nearby the coil. Even the human's body movements around the detector can influence the output signal, so all manipulations should be performed very carefully.

4. Conclusion

As a conclusion, it should be mentioned that eddy current testing allows detecting porous silicon conductivity changes. We succeeded to detect the porous Si conductivity change during NO₂ gas injection, however this experiment was performed for the saturated gas atmosphere, that does not actually allows to plan a sensing system working according to this method of detection. As a perspective, to improve the stability and sensitivity of the measurement scheme, several improvements can be proposed. First of all, porous Si film should be made as thick as possible to introduce more carriers influenced to eddy current. To avoid the detector response on surrounded conductors, a differential measurement scheme could be implemented. Moving to even higher frequencies is also an option, to improve the eddy currents localization in the sample bulk. Additionally, the eddy current conductometer developed in our work allows to measure the conductivity of crystalline silicon (since it has much higher conductivity in comparison with porous Si), as well as Si conductivity changes caused by the heating of the samples or excitation by radioactive β -source.

Seventh Chapter

Porous Silicon Localization for Implementation in Matrix Biosensors

The search for appropriate substrates and methods of surface DNA functionalisation is one of the important tasks in the field of semiconductor biosensors. In this work, we develop a method of light-assisted porous silicon etching in order to localize porous silicon spots on silicon substrate for matrix fluorophore-labeled DNA sensors implementation. Different methods of porous spots localization proposed are considered for n- and p-type Si substrates under the condition of supplementary illumination. The tuning of the porous profile via the application of a lateral electric field is suggested and experimentally proved. The material of this chapter is published in [155].

1. Introduction

It is well known that the immobilization of DNA strands and the detection of DNA hybridization still remain important problems under current consideration for DNA chips biomedical implementation. Porous silicon is currently considered as a promising substrate for biosensors fabrication mainly because of its developed surface, which can be enormously large (several hundreds of m^2 per cm^3) compared to the plane one [25]. This fact attracts steadfast attention to increase the concentration of immobilized probes. For biochips with macroscopic spots (several mm^2) biochips based on the fluorescent-labeling technique, the usage of porous silicon substrates allows increase of the read-out signal by factor 5 – 10 [156].

The development of new sensing methods [80, 157] can be based on visible photoluminescence and refractive index modulation of porous layers. Waveguiding structures, Bragg and rugate mirrors, and microcavities allow building of highly sensitive optical sensing system [93, 158]. Interference phenomenon (as applying to the routine spectroscopy or ellipsometry) on porous silicon layers is a very sensible optical method for the biomolecular interaction processes monitoring [84, 159]. Impedance and potentiometric measurements are also well applicable to porous silicon structures [97, 160].

There is a need to localize porous spots on the substrate surface in order to define the sensitive areas in matrix sensor. Different aspects of porous silicon localization, such as modified lithographic methods and local ions incorporation were mentioned in the first chapter of this thesis. In this work we propose a light-assisted porous silicon etching in order to localize porous silicon regions on n-doped and p-doped silicon substrates. The main motivation for such approach is to avoid the photolithographic step as well as to tune the porous profile.

2. Principle of porous silicon localization

2.1. Electrochemical etching of silicon

As far as for the moment, an exact mechanism of porous silicon formation by the anodization process is still under all-round discussion, there are several models giving an attempt to describe the phenomenon as it was mentioned in chapter 1. Nevertheless, all admitted models point to the leading role of holes in porous silicon formation. Thus, in moderate doped n-type silicon the concentration of minority charge carriers is insufficient for etching process, the supplementary excitation (e.g., illumination) is necessary to produce the holes. Generated electrons and holes are effectively separated by built-in potential [161] arising at n-Si/electrolyte interface (Figure 7.1) and nonequilibrium holes drift towards the surface [29]. Anyway n-doped silicon remains unetched in HF-based solution if there is no illumination.

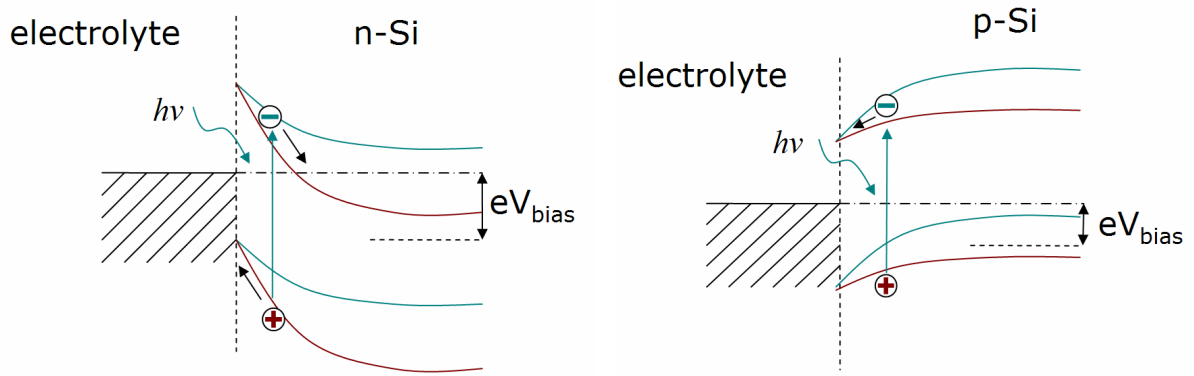


Figure 7.1 Energy bands bending in electrolyte-silicon interface at supplementary illumination: without applied voltage bias (dash) and with applied voltage bias V_{bias} (solid, positive potential is applied to Si substrate) for n- and p-doped silicon respectively.

For p-type silicon the equilibrium holes participate in etching process. However, one can notice that the behavior of surface energy band can lead to the depletion of holes near the surface. Regarding p-Si/electrolyte interface, an additional voltage bias (with positive potential applied to Si substrate) is necessary to supply the surface by nonequilibrium holes (Figure 7.1). Here, as apparent from energy band bending, it is easier for electrons to reach the surface, while for holes, an additional electric field is necessary to drift against electric field of built-in potential. This phenomenon was used to block the electrochemical silicon etching of moderate doped p-silicon.

As far as light can assist n-type silicon etching and block the etching of p-type one, this fact can be taken into consideration to perform a localized porous silicon etching without involving a complex lithographic methods.

2.2. Porous silicon localization for p-Si

Assume that we have a p-doped silicon wafer with one of its side uniformly illuminated by strongly absorbing light (Figure 7.2). For the p-doped silicon, a concentration of minority charge carriers (electrons) generated by illumination is distributed along the shaded part of the sample as follows (steady-state condition) [135]:

$$n(x) = n_{p0} + G \cdot \tau_n \cdot e^{-x/L_n} \quad (7.1)$$

where G is the optical generation rate, τ_n the lifetime of minority charge carriers, L_n is the minority charge carriers diffusion length.

G in its turn is defined as follows:

$$G = \frac{\eta \cdot P / h\nu}{d} \quad (7.2)$$

where η determines the effective quantum efficiency of photogeneration (number of carriers produced by a single photon absorption), P is the power of illumination per unit area, $h\nu$ is the photon energy, $d \sim 1/\alpha$ is the depth of light absorption, with an absorption coefficient α . For a short-wave illumination, the light is absorbed in a surface layer: at $\alpha=10^5\text{--}10^6\text{ cm}^{-1}$, the value of d falls in the range 1—10 μm .

As far as silicon etch rate V in general case is determined by the holes concentration near the surface, the produced porous silicon depth distribution will follow the distribution of this concentration near the surface:

$$V(x) \sim [p_{p0} - n_p(x)] \quad (7.3)$$

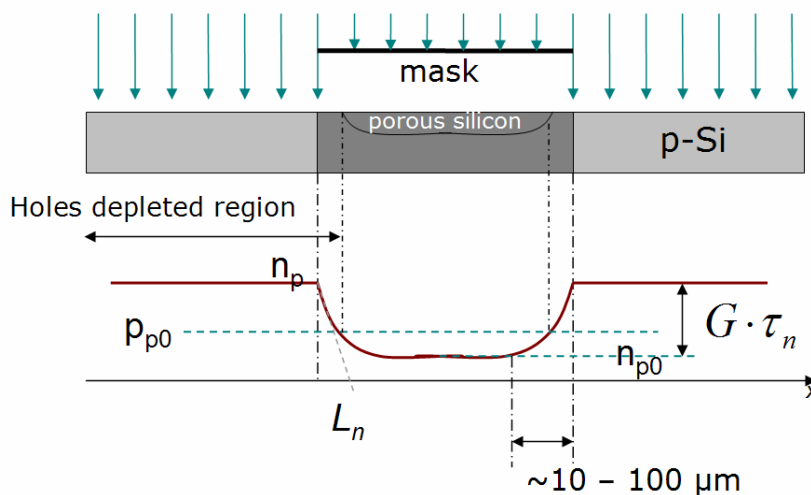


Figure 7.2

Porous area formation in a shaded region of p-doped silicon. The curve below shows the minor carriers (electrons) concentration near the surface of the sample.

Thus, the etching process is developed in the shade region under the mask for which the inequality $p_{p0} > n_p(x)$ is in progress. Even assuming that the etching rate in the Si substrate is independent of crystallographic orientation (isotropy etching), an under-etching effect takes place for p-Si due to the generated electrons diffusion from the illuminated part of the sample towards the shaded one (Figure 7.2).

2.3. Porous silicon localization for n-Si

For the n-doped silicon, similar thoughts give the inverse result: porous silicon is formed on the illuminated surface while the shaded one remains unetched. An overetching takes place in this case (Figure 7.3).

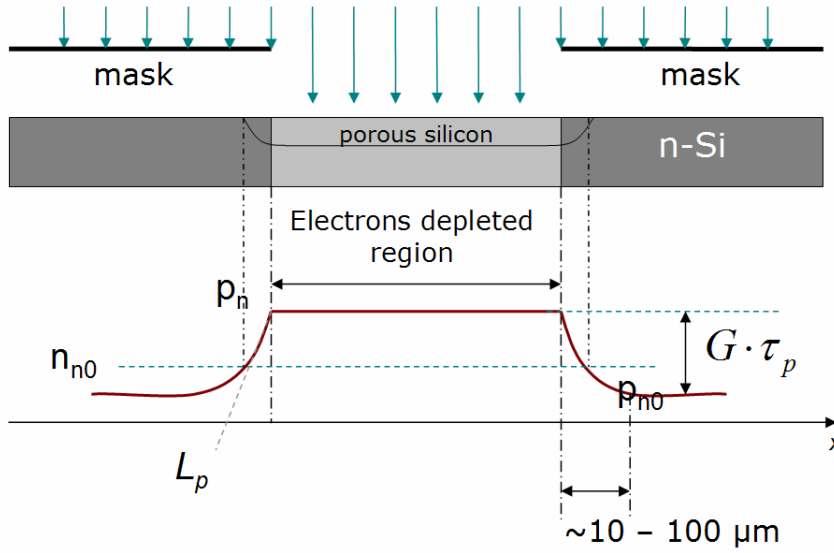


Figure 7.3

Porous area formation on the illuminated region of n-doped silicon.

The resolution of the silicon surface patterning method described here is limited by the diffusion of minor carriers, and has a value of several tens of microns. Moreover, the borders of the porous silicon area formed are not quite sharp in depth. This artifact could be reduced with a help of superficial carriers drift.

2.4. Impact of electric field

Minor carriers surface concentration can be varied by the application of a supplementary surface lateral electric field. This can lead to the edge tailing of etched area profile caused by the carriers drift along the applied field direction. Minor carriers excess density caused by the drift can be described by the following expression (7.4) [135]:

$$\Delta p = \Delta p_0 \cdot e^{-x/L} \quad (7.4)$$

where L is a drift length which results in the length of etched profile tailing:

$$L = \tau \cdot \mu \cdot E \quad (7.5)$$

where τ is the minor charge carriers lifetime, μ is the minor charge carriers mobility, E is the applied electric field. The etched profile tailing along surface is about the length of drift. Taking into consideration that $\mu_p = 450 \text{ cm}^2/\text{V}\cdot\text{s}$, and that in n-Si, for a diffusion length $L_p = 100 \mu\text{m}$, the hole life time is $\tau = 8 \mu\text{s}$, the shift of etched profile tailing $L \sim L_p$ is reached at relatively small values of electric field $\sim 3 \text{ V/cm}$. The effect should depend on electric field direction. We assume that such method allow tuning the profile of pore growth.

3. Experimental

For experimental investigation, p-type and n-type (100) silicon wafers were used. The resistivity of the wafers was about $10 \Omega\cdot\text{cm}$. The silicon samples were cleaned in ultrasonic bath with acetone and ethanol followed by rinsing in deionized water. For the

etching solution HF (48%) was used with ethanol in volumetric proportion 1:1. Each sample was anodized during 2 minutes with a constant current of 20 mA/cm^2 . The samples etching was assisted by illumination via a mask using a mask aligner to produce on the surface an array of porous spots of 1 mm in diameter. As a light source, a YAG laser ($\lambda=532 \text{ nm}$, $P=2.5 \text{ mW/cm}^2$) and a mercury lamp ($P=1.5 \text{ mW/cm}^2$) were used (Figure 7.4). After the etching, the samples were washed in ethanol then rinsed in deionized water and dried under a stream of nitrogen.

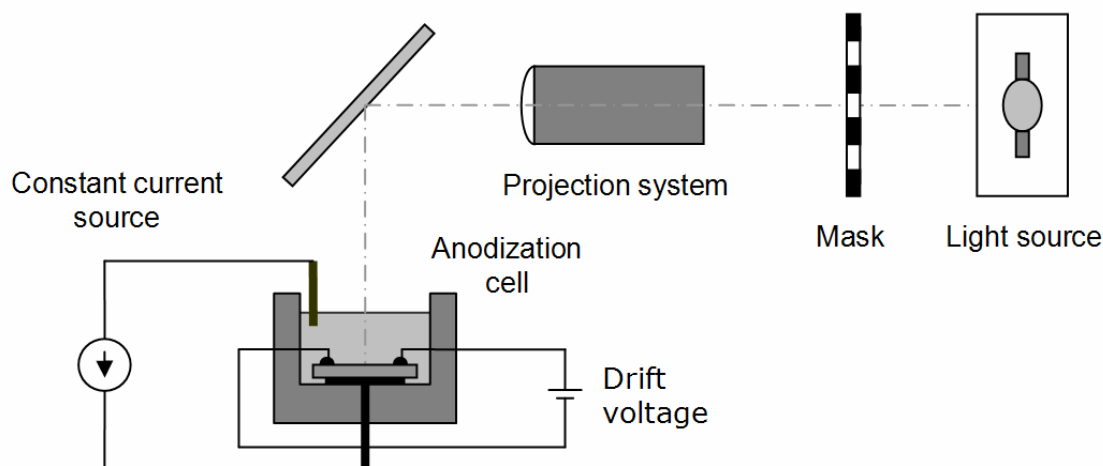


Figure 7.4 Porous silicon local light-assisted anodization setup. Drift voltage was used only during the investigation of lateral electric field impact on localized porous silicon profile.

For observing a field effect value, n-type (100) silicon wafer was used. The etching process was assisted by YAG laser illumination and application of a surface field of 100 V/cm during 30 seconds in the same etching solution (Figure 7.4). This sample was also exposed to the same cleaning procedures.

The prepared samples were investigated using a WYKO surface optical profilometer. For this purpose, a layer of porous silicon was first removed by immersion in 30% KOH water solution for several seconds. The porosity of the samples was estimated by contact angle measurements.

4. Results and discussion

4.1. Profile measurement

A general view of porous Si spots on silicon surface is presented in Figure 7.5. This sample is an array of porous spots ($\sim 1 \text{ mm}$ in diameter, 500 nm in depth), after immersion in the KOH solution in order to etch porous silicon (thus, a small cavities formed in the places of porous spots) to perform the following investigation with the optical profilometer.

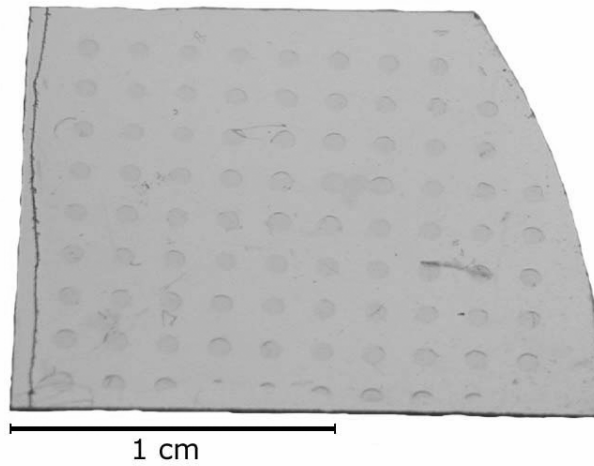


Figure 7.5

Photo of porous silicon array after immersion in KOH solution (p-doped Si substrate).

As it was predicted above, there is an “overetching” on the n-doped samples (porous spots are a little bit larger (~1.4mm in diameter) than aperture in the mask) and an “underetching” on the p-doped samples (porous spots are a little bit smaller (~0.8 mm) than shade of the mask) (Figure 7.6).

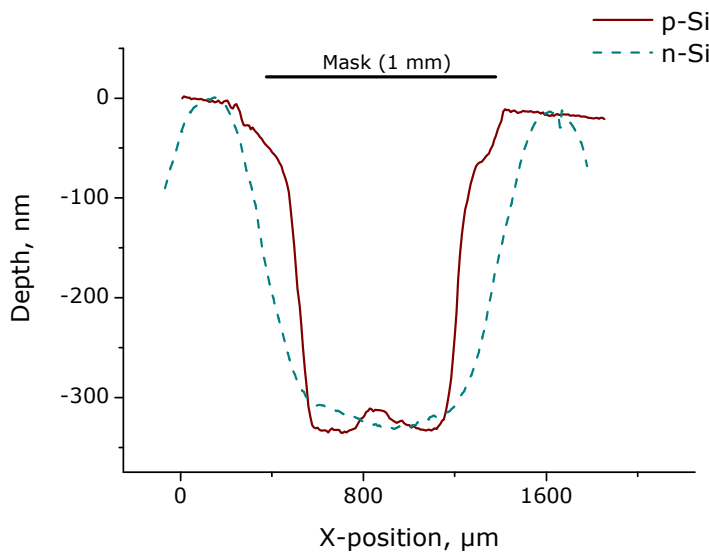


Figure 7.6

Porous spot profile n- and p-doped silicon samples. A slight height increase at the center of porous spot for p-Si is explained by the laser diffraction on the mask.

These deviations are well correlated with the intensity of illumination, so the effect is well explained by minority carriers diffusion process. The diffusion also explains the inhomogeneity (~10—80 μm) of the porous silicon profile near the etching boundary. We found that the field effect also has an influence on porous silicon profile tailing along the surface field applied (Figure 7.7). This leads to the porous silicon profile displacement of about 100 μm along the field applied.

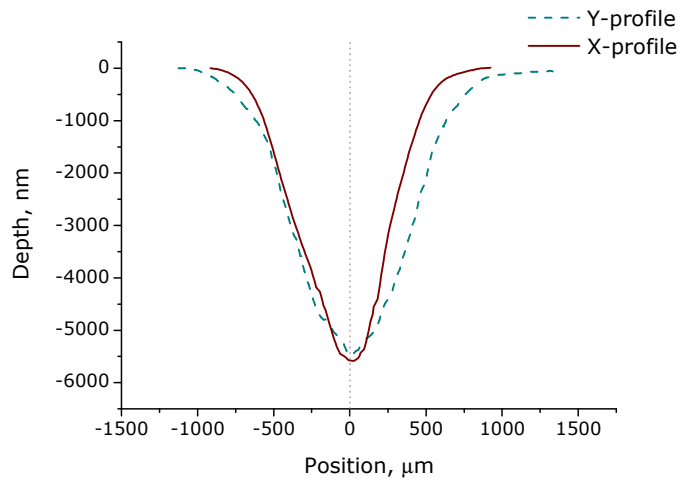


Figure 7.7

Typical porous spot profile of n-doped silicon etched while additional surface field is applied, which provokes etched profile displacement along the field direction (X-profile). No profile tailing is observed for the orthogonal direction (Y-profile).

At the same time, the profile of porous spot remains symmetrical in the orthogonal direction and copies the laser field distribution (Figure 7.7). (For a Gaussian laser this effect is described in [29]).

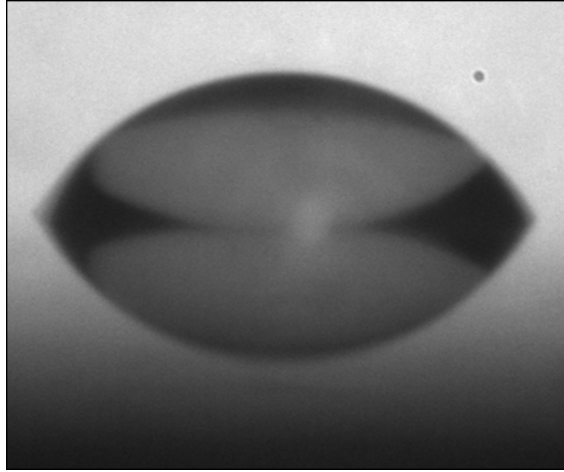
4.2. Local porosity estimation from contact angle measurement

The surface of porous Si manifests hydrophobic properties just after formation. Since porous Si has a tendency towards oxidation while being placed on open air or in aqueous environment, its hydrophobic properties switch to hydrophilic. Assuming that porous Si layer is a homogeneous set of pillars, one can estimate the porosity by a simple contact angle measurement of water drops on the porous Si surface. Indeed, according to the Cassie and Baxter's formula [162], taking into consideration that the drop only contact the top of the pillars, the contact angle can be calculated as following (7.6):

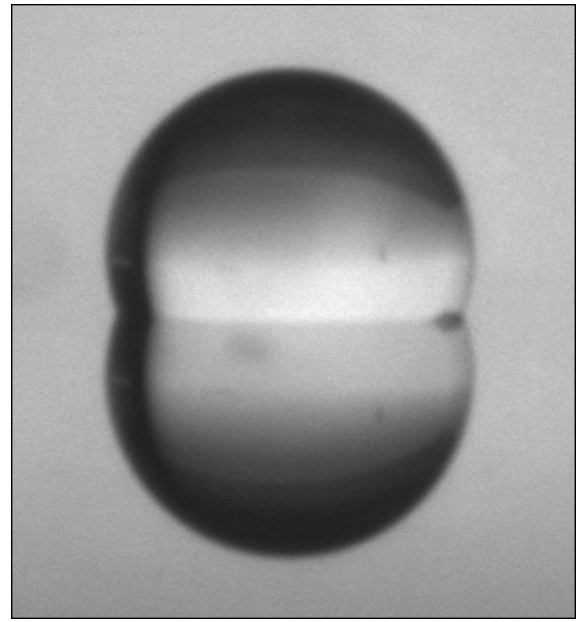
$$\cos \theta_r = f \cdot \cos \theta_s - (1 - f) \quad (7.6)$$

where θ_r is the contact angle of the porous (rough) surface, θ_s is that on a smooth surface of the same type, and f is a fraction of the surface contacted by the drop. For a homogeneous porous Si layer the value of $(1 - f)$ is actually the sample's porosity.

The following images represent a view of a drop of water on silicon and porous silicon areas of the same Si wafer. Figure 7.8 was obtained immediately after the etching and cleaning procedures to avoid the surface oxidation.



Silicon surface, $\theta = 59^\circ$



Porous Si surface, $\theta = 112^\circ$

Figure 7.8 Drops of water on the cleaned surface of silicon and on the surface of localized porous Si just after the preparation.

According to (7.6), the porosity of the sample can be estimated as (7.7):

$$P = \frac{\cos \theta_s - \cos \theta_r}{1 + \cos \theta_s} \quad (7.7)$$

For the sample represented in Figure 7.8, the calculation gives:

$$P = \frac{\cos 59^\circ - \cos 112^\circ}{1 + \cos 59^\circ} \approx 60\% \quad (7.8)$$

This method cannot provide an exact value of porosity but was used in our experiments for fast estimation of the prepared samples porosity.

4.3. Optical measurement

Thus, a proposed porous silicon localization method can be implemented in low precision porous localization applications like low-concentration matrix porous silicon biosensors fabrication. To prove this statement, an array of porous spots (8 by 8 spots of 1 mm in diameter with 1 mm step between the spots) was fabricated on p-doped silicon using the localization technique described. We considered this sample as a support of hypothetical matrix bio-sensor that uses CY3 fluorophore marker. According to [163] the thickness of the porous layer should be adjusted in order to provide an effective reflection for the fluorophore emission. Thus, the optical thickness of the porous spots should be adjusted to form interference reflectors for CY3 fluorophore ($\lambda_{\text{excitation}}=532 \text{ nm}$, $\lambda_{\text{emission}}=562 \text{ nm}$). The final structure that we want to obtain is represented in Figure 7.9.

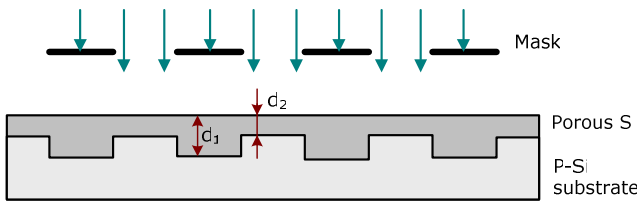


Figure 7.9

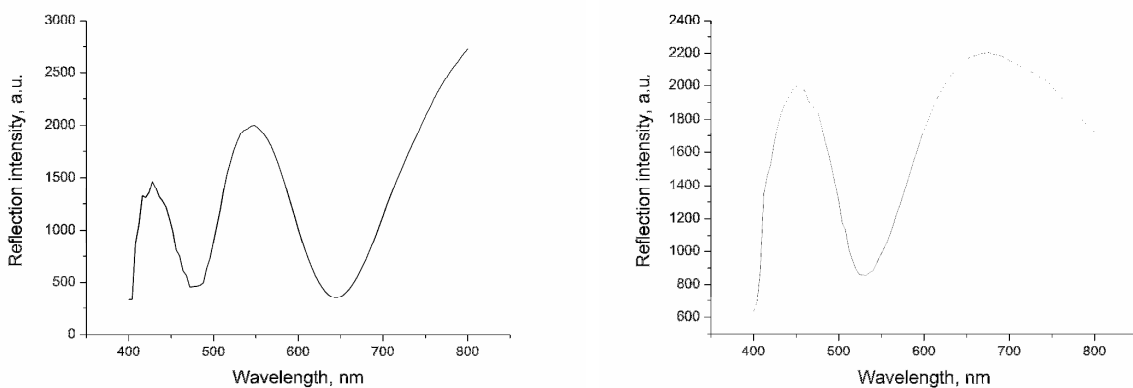
A sample with localized porous Si spots of different thickness d_1 and d_2 .

The intensity of illumination was adjusted experimentally in such manner for not to block the porous silicon formation outside the spots completely. Thus, porous silicon was formed on the whole sample surface (according to the Figure 7.9). However, the thickness of the porous Si layer outside the spots was made thinner, in order to suppress the reflection from outside of the spots. Using the effect of illumination, we actually slowed down the etching process of the illuminated part of the sample. To conform to our needs, the thicknesses of porous layer should meet the following conditions:

$$\begin{aligned}
 d_1 n &= \lambda_m k, \text{ for positive interference} \\
 d_2 n &= \lambda_m \left(k + \frac{1}{2}\right), \text{ for negative interference} \\
 k &\in \mathbb{N}
 \end{aligned}
 \tag{7.9}$$

where n is the refractive index of the porous layer (we assume, that it is the same for the whole layer), λ_m is the wavelength of interest, which can be somewhere between $\lambda_{\text{excitation}}$ and $\lambda_{\text{emission}}$ of fluorophore for a good compromise between sample excitation and fluorescence signal collecting. These conditions correspond to positive and negative interference for the normally induced light.

The reflection spectra of the final fabricated sample manifest the desirable interference fringes for localized thick (Figure 7.10, A) and thin (Figure 7.10, B) porous areas.



A

B

Figure 7.10

Reflection spectra for porous silicon sample:

A — on the localized spots

B — outside of localized spots

After covering of the whole surface of the sample by the CY3 fluorophore solution and the drying procedure, a fluorescence image (Figure 7.11) was scanned with an instrument, developed in our laboratory.

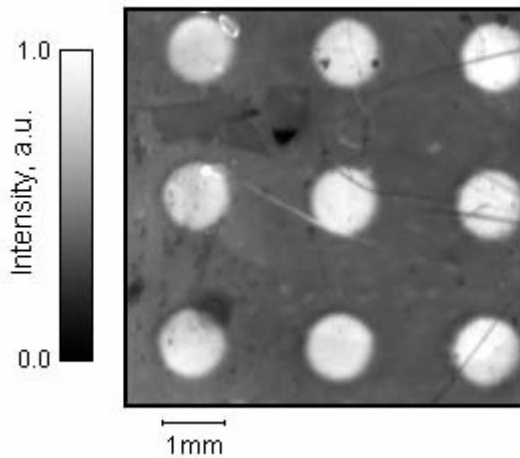


Figure 7.11

Fluorescence map on the surface of p-type silicon sample with localized porous spots. The whole sample surface is covered by CY3 fluorophore. However, the signal intensity is significant in the region of the spots.

The fluorescence map profile (Figure 7.12) shows that, due to the correct adjustment of porous Si layers thickness, we can gain the signal intensity more than tree times in the specified area (localized spots in our case).

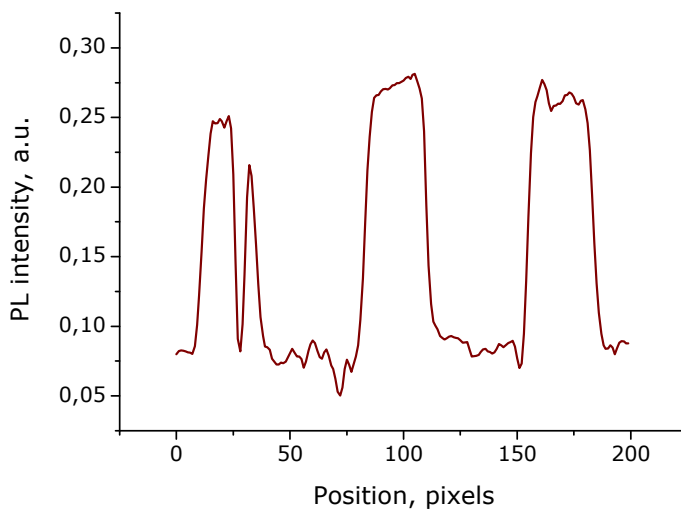


Figure 7.12

Fluorescence scan (Figure 7.11) profile over 3 localized spots.

As far as during PL scan the sample was excited by a green laser source ($\lambda=532$ nm), the porous Si layer does not manifest any photoluminescence, and thus does not have any influence on the scanned PL image.

5. Conclusion

We can claim that the proposed method of porous silicon localization seems to be well applicable when a high spatial resolution is not required. The highest resolution that we could achieve, is limited by the minor carriers diffusion length (~ 100 μm). Except for the addition of a lighting setup the general procedure of porous silicon formation rests unchanged

(anodization process). This means that it is still possible to control porous silicon growth speed and porosity by varying the anodization current and the properties of the etching solution, like in routine anodization process. In such way, we managed to set the anodization parameters to produce an array of localized porous spots with defined porosity and thickness. These porous spots acted like interference reflectors to improve fluorophore-labeled DNA molecules detection.

Eighth Chapter

Electrical Discharge Machining of Silicon

This chapter concerns the implementation of micro electrical discharge machining (μ EDM) for silicon machining. Our initial goal was to produce porous silicon. However, the ideas and realizations described are rather general and can be implemented to the machining of any conductive materials: crystalline silicon (doped or not), SiC and stainless steel for example. The work covers different aspects of μ EDM process: micro-electrodes fabrication, spark pulses generation (EDM power supply), discharge stabilization methods, and machining control techniques. A short perspective on nano EDM is included.

1. Introduction

In this chapter we will consider techniques, which are rarely used for machining in the world of Microtechnology. Traditionally in the mechanical industry, the removal of material is performed in general by milling. Micro-milling is drawing the attention of the scientific community for MEMS or microfluidic applications [164], but recently nano-milling, based on scratching with AFM tip, is started to demonstrate interesting achievements [165]. Our goal, in this section, is to consider another machining technique which is important in the mechanical industry and may follow the same way from meso- to micro- and nano-scale: electrical discharge machining (EDM), sometimes also referred as spark machining or spark eroding.

EDM is considered as the most widely used non traditional method of material removing [166, 167]. Firstly proposed by B. R. Lazarenko and N. J. Lazarenko in 1943 [168], EDM became an important process because it does not involve a mechanical contact between the tool and the part to be machined. Even extremely hard parts can be machined as long as they are electrically conductive (metals, semiconductors, conductive ceramics). The idea of EDM is based on the fact that electrical discharges (sparks) between two conductive electrodes placed in immediate proximity to each other lead to the electrodes destruction (particularly fusion and evaporation) as far as the temperatures of the materials close to the discharge gap region become very high at the value of 8000—12000°C [166, 169]. EDM works usually in liquid dielectric environment (deionized water, oil or kerosene), which role is to cool down the tool and wash out the waste (debris) of machined workpiece [166]. Obviously, the rate of material destruction is related with the energy passed in the discharge as well as with the material properties of the electrodes (fusion temperature, hardness, etc.) and the nature of the dielectric. Depending on these factors, the machining rate can be characterized by a parameter named material remove ratio (MRR), which is introduced to denote the volume of material removed by single erosion pulse (spark) passed. As far as both electrodes are influenced by a spark, the tool electrode should be chosen with a low MRR value, and the other one (the part to be machined or workpiece) should have a relatively high MRR [170-175].

Although EDM principles are quite simple, this technique allows complex 3D machining that is not accessible (or hardly realizable) by any other machining techniques. In some applications, EDM has replaced traditional machining processes, such as the milling of hard steels or conductive ceramics. Since EDM does not introduce mechanical stresses during machining, it provides an additional advantage in the manufacture of delicate objects. According to the standards in the mechanical industry, good finishing surface state ($R_a \sim 0.1\text{—}0.8\ \mu\text{m}$) as well as a good machining precision and resolution can be achieved with commercial equipment [176, 177]. For the smallest features size, industrial EDM remains at the level of holes of 100—200 μm in diameter. This fact is mainly explained by difficulties of microelectrodes fabrication (as far as they wear) [170], and electrical micro-sparks controlling [178].

1.1. Spark discharge and erosion

EDM of conductive parts in a dielectric medium is an electro-thermal material removal process. Surprisingly little is known on the physics underlying the erosion process [179-181]. Applying of a certain DC voltage across the gap between electrode and workpiece

generates an electric field (Figure 8.1, a). At the first moment, the tool electrode and the workpiece are isolated by the dielectric working fluid or gas, so no current flows. For a strong electric field (several kV/cm), impact ionization can occur at this stage (theoretically a single ionized molecule of dielectric can be accelerated by the electric field leading to the avalanche process) that results in formation of a conductive bridge (streamer) between electrode and workpiece (Figure 8.1, b).

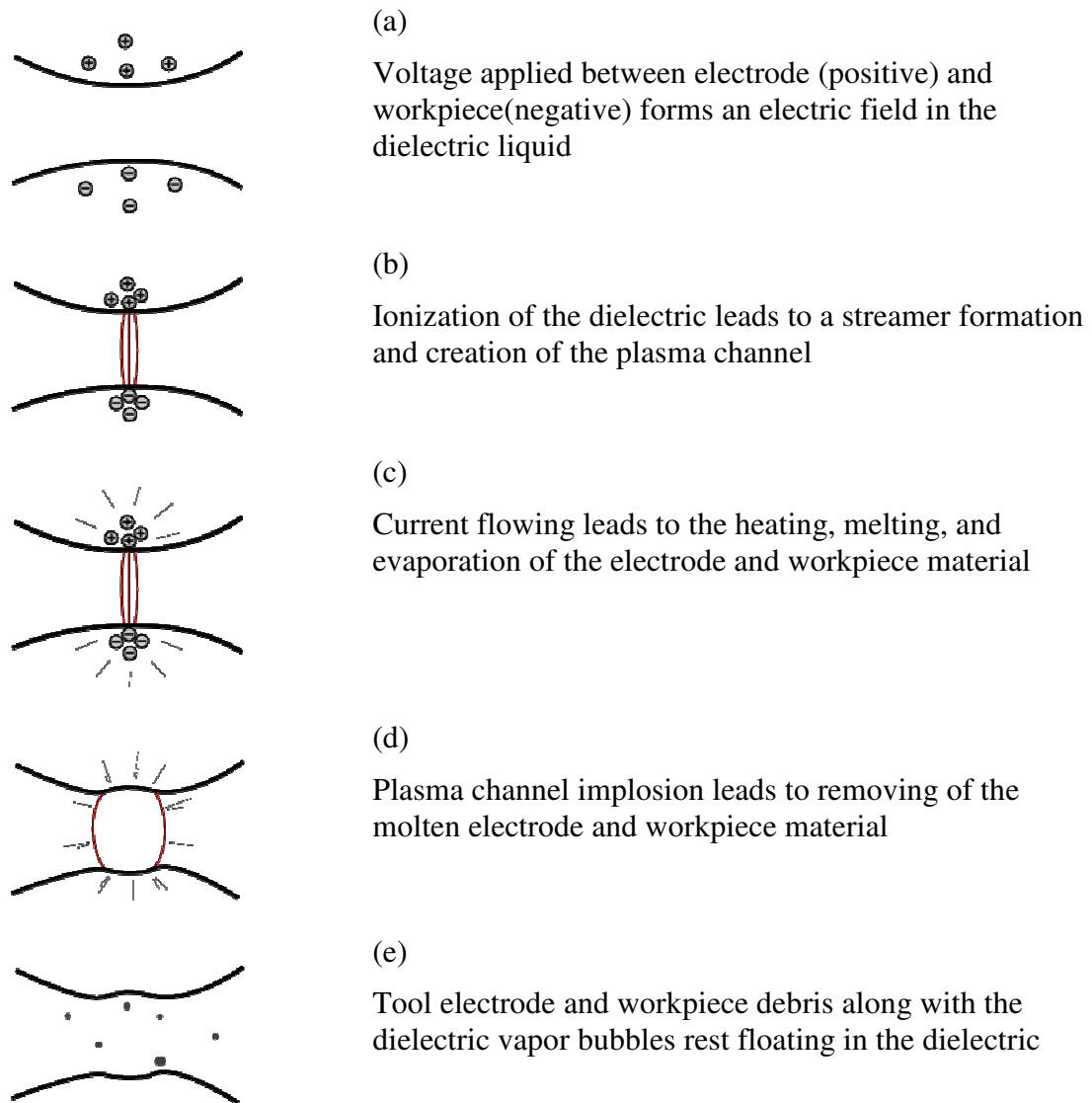


Figure 8.1 EDM discharge process [180]

The streamer is filled with plasma, which consists of dielectric ionized molecules and also ions of both electrodes (tool and workpiece) which evaporate intensively during the discharge (Figure 8.1, c). The expansion of streamer channel leads to the formation of a blast wave which can be heard as a crackling. The development of the discharge channel finally leads to a current break and the surrounding environment cools down the discharge channel (Figure 8.1, d). Finally, the residual vapor bubbles and workpiece (and tool as well) debris rest floating in dielectric (Figure 8.1, e). These wastes should be washed out thoroughly (by

dielectric flow) before the next discharge passed. The surface texture of the machined part is characterized by the typical discharge craters with a molten and resolidified zone and a heat affected zone. It is known that during the erosion of the workpiece, a superficial recast layer may be formed in the workpiece, composed in general of different distinct layers depending on the materials and machine parameters [182].

1.2. Single electrode EDM

In EDM, the machining process is realized by passing a series of discharge sparks (many of them) between the electrode and the workpiece, which leads to the adequate copy of the electrode into the workpiece. The main types of machining are die-sinking, with a complex 3D electrode (machined by milling or also by EDM) (Figure 8.2, a) and wire-cutting with a circulating wire electrode (Figure 8.2, b). Sometimes EDM is also used in the hole-drilling configuration, simply to machine holes in parts with an electrode tip (Figure 8.2, c). There is also an EDM configuration, called EDM milling, which consists in using of a tip electrode to perform the machining by computer numerical control (Figure 8.2, d).

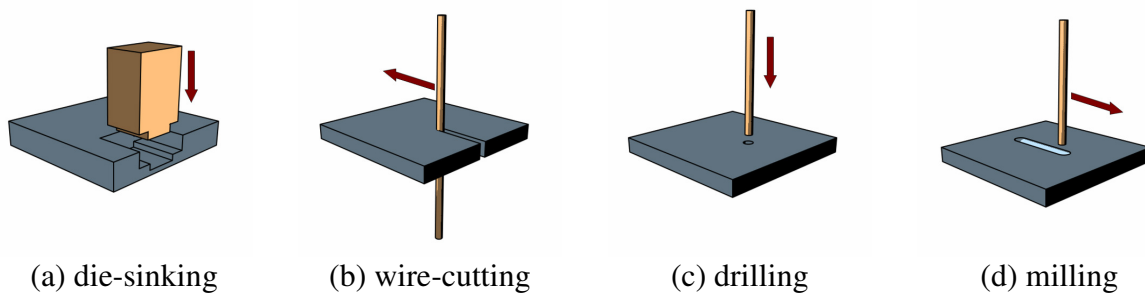


Figure 8.2 Different modes of EDM.

EDM milling is considered as an advanced process rarely used probably, because it is difficult to prepare thin electrode tip. Single electrode EDM milling is rather universal and allows complex 3D form machining using step-by-step engraving (Figure 8.3), however the machining time is significantly greater for the EDM milling, comparing with die-sinking EDM.

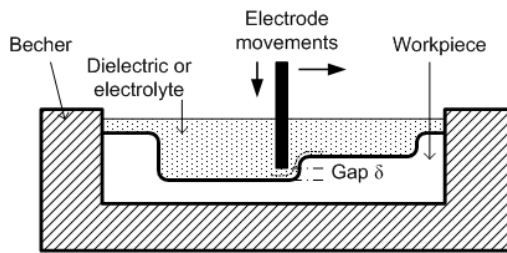


Figure 8.3

Step-by-step machining by single electrode EDM operating in milling mode.

1.3. The role of dielectric

As mentioned above, EDM is carried out in a dielectric environment, which is usually liquid: oil, kerosene, or deionized water [183] (more rarely air, oxygen and various gases can be used in a new promising process called dry EDM [184]). The most important role of this fluid is to wash out the machined particles. In case that the liquid flush is not sufficient, the machining process can be troubled by debris between the tool electrode and the workpiece, which may dramatically reduce machining performance and quality. It was shown, that dielectric fluid properties (conductivity, viscosity) have a great influence on MRR value and working electrode wear. Deionized water is claimed to be a good dielectric to be used in EDM process [166]. To improve the dielectric fluid circulation, workpiece ultrasonic vibration or work electrode rotation can be applied [185, 186].

1.4. Micro and nano EDM

Although there is a pioneering work from Reynaerts et al. as regards the machining of silicon [38, 187, 188], the use of EDM is not well established in the world of Microtechnology except for MEMS packaging [189] and hole drilling for ink jet printer head [190]. The reason is that EDM is considered as a low speed sequential machining process of limited resolution which cannot compete with collective fabrication.

In the field of micromechanics, which needs a wider range of materials and also often complex geometries, the miniaturization of EDM, called micro-EDM (μ EDM) is still currently under development at the micrometric resolution [191] and can be considered as (relatively) mature for specific topics like the fabrication of nozzle for innovative fuel injection device for diesel engine [176].

The very few existing commercial μ EDM machines are in general dedicated to wire EDM (e.g. with 20 μ m diameter wire) or hole drilling, and seem to be limited to a resolution of 20-50 μ m [192]. Current progress in μ EDM technique is conceived in general as an upgrade of the existing equipment and methods [193]. Sometimes these upgrades seem to be impressive [194], but so far we have not (yet) seen convincing applications for micrometric features. For a practical use of μ EDM at micrometric resolution, the main limitations seem to come from: (i) the fastidious fabrication of thin electrodes, which is often performed by

milling or reverse-EDM, (ii) the availability of electronics for ultra fast low energy discharge control, that is necessary at micrometric and submicrometric resolution, (iii) the lack of metrology integrated with the EDM process and used in combination with it, in order to facilitate the operation (evaluation of electrode wear, change of electrode during machining, etc.) and of course (iv) the cost of the equipment.

From a totally different perspective, it is worth to note that EDM at nanometric scale can be also conceived as an extension of the AFM-STM techniques with working electrodes directly mounted on commercial instruments. This approach is followed by Virwani, Malshe et al. with very preliminary results [195, 196].

There have indeed been little attempts to develop a dedicated low cost and compact μ EDM instrument making use of high resolution technology like piezoelectric actuators, which are commonly used by the AFM-STM community [192]. Thus, the objective of this work is to develop such an instrument. We propose first to develop this EDM set up so as to reach micrometric features, leaving for future research, the development of an STM based upgrade head for submicrometric or even nanometric features.

1.5. Summary of strategy and objectives

In the field of Microtechnology, the development of new processes for features machining on a wide range of materials at micro and nanoscale is essential. Various techniques are available like UV lithography combined dry (RIE) and/or wet etching, focused ion beam, LIGA, nanoimprinting, microcontact printing, femtosecond laser machining, etc. But currently there is no flexible, single, low cost process, capable to machine micro and nanoscale features and structures with high aspect ratio in hard metals or semiconductors, in a non-vacuum (e.g. liquid) environment, and in a single step.

Our aim here is to perform a preliminary work to develop such an instrument based on spark machining. An important innovation will be to prepare the electrode tools not by milling or by EDM [197] or reverse EDM (when the electrode is machined against the workpiece while the applied voltage pulses polarity is reversed [198-200]), but with a straightforward simple and low cost electrochemical process, used mainly for the manufacturing of STM tips and applied for the first time to EDM. Machining with high aspect ratio will be achieved by milling-EDM with a serial and automated process based on a layer by layer milling with a careful control of the process parameters, especially the management of the electrode-workpiece gap. The machine will be based on state of the art micro and nano actuators but a specific electronics will be developed to create the discharge. Also we will

take advantage of the machine architecture to perform some metrology using the working electrode for a three dimensional measurement tool.

Although the EDM process will remain based on a sequential principle, it can be in the future completely automated, including complex software for example for tool diameter or electrode wear compensation, change of electrode, interfacing to CAD/CAM package etc. Therefore our estimation is that this technology may allow machining of prototypes for research and development at a competitive cost compared to other technologies (FIB, e-beam & RIE, LIGA...).

2. Development of a μ EDM setup

2.1. Preparing of μ EDM electrode

To fabricate EDM microelectrodes (tips) Pt-Ir wires of 0.25 mm in diameter were used. We used also successfully Cu wires and W wires, but Pt-Ir material was chosen due to its properties: good electrical conductivity, stability (the electrode does not oxidize during the machining process), and high melting temperature. Owing to these properties, Pt-Ir electrodes are expected to have rather low wear factor when silicon machining. The wire was etched electrochemically using a simple setup, represented in Figure 8.4.

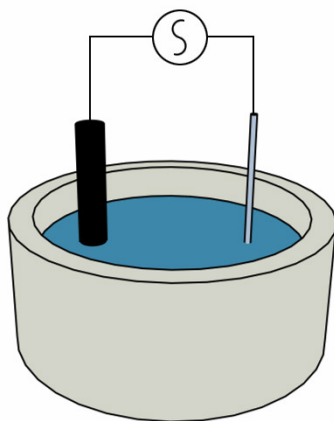


Figure 8.4

Setup scheme for Pt-Ir wire etching to form a μ EDM tip. For reference electrode, a thick graphite rod is used in our etching setup implementation.

The tip etching process performed is commonly referred as “drop-off” process [201]. The capillary forces of electrolyte form a meniscus around the wire when it is immersed into the electrolyte. In the meniscus the etching rate is enhanced [201, 202], thus, a necking phenomenon is observed. Finally, this part of the wire becomes so thin that can not hold the lower end of the wire, so the latter breaks off and a sharp tip is left behind (Figure 8.5).

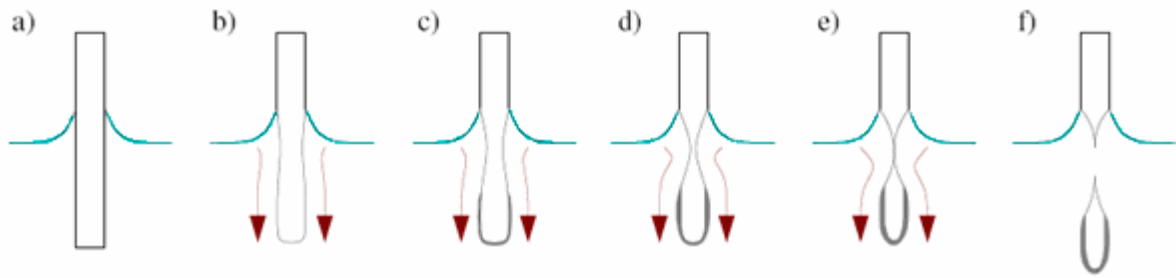


Figure 8.5 Illustration of “drop-off” method of sharp tip fabrication: a) the formation of meniscus; b) to e) necking phenomenon, arrows show Cl^- ions flow; f) drop-off of the lower part of the wire (the original scheme was taken from [203]).

According to [201, 202], non hazardous CaCl_2 or NaCl salt can be used to prepare the solution for electrochemical etching. Actually, we tried both salts and obtained the same final results, so there is no any particular issue to choose one or another. CaCl_2 solution has more Cl^- ions and this fact leads to faster overall etching process. However finally saturated NaCl solution was used for electrodes etching. The etching was performed in several steps:

- 1) Applying AC voltage of 30 V for initial fast etching step;
- 2) When the neck of the wire becomes rather thin (controlled by eye) the voltage was adjusted to 20 V;
- 3) Just before drop-off stage, the voltage was adjusted to 5—10 V to perform an accurate final drop-off step.

The following images (Figure 8.6) show the typical tip viewed by optical microscope.

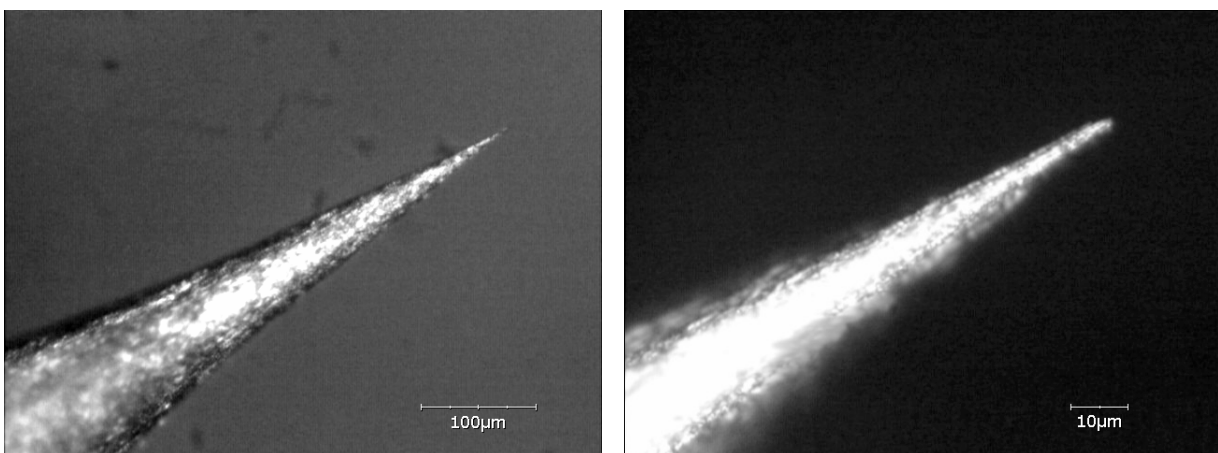


Figure 8.6 Pt-Ir wire μEDM tip fabricated by electrochemical etching in NaCl solution. Viewed by optical microscope, $\times 10$ magnification (left image), and $\times 50$ magnification (right image).

According to these photos, the tip head radius can be estimated as approximately $1\ \mu\text{m}$. However, these electrodes are not well suited for a durable EDM process due to the wear phenomenon that leads to the widening of the microelectrode tip. So, obtaining of a

cylindrical electrode is more preferable for EDM. A slight modification of the etching scheme (Figure 8.4) allows the formation of long cylindrical electrodes. It consists in drawing the electrode from the solution during the etching at a constant speed, so that the etching zone of meniscus is displaced along the electrode. The result of such kind of etching is presented in Figure 8.7. However in this case, the drawing was performed manually (we had not enough time to develop an automated process).

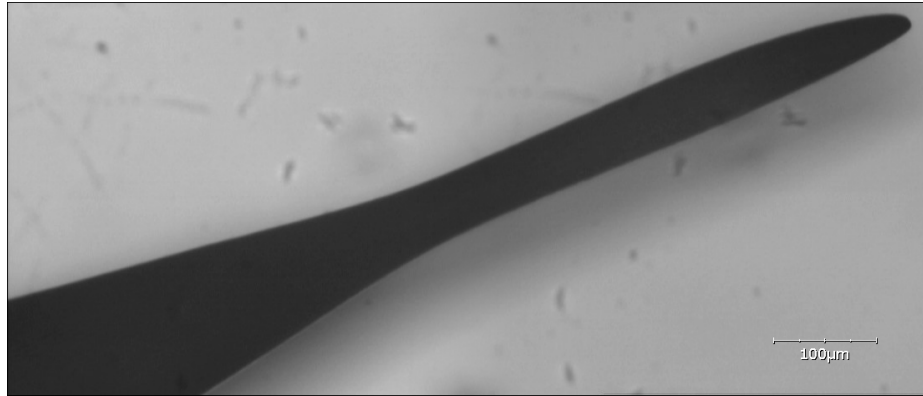


Figure 8.7 Pt-Ir electrode obtained by etching in NaCl solution with drawing applied in order to give a cylindrical shape.

2.2. Positioning actuators and mechanical frame

The mechanical part of μ EDM setup is made of a combination of micrometric and nanometric positioning actuators in order to achieve high working volume and accuracy. It consists in a motorized X Y table, with an independent motorized Z axis holding the working electrode, driven by stepper motors with a precision of $2.5 \mu\text{m}/\text{step}$ (speed up to 1000 steps/s). This table covers approximately a $10 \times 10 \text{ cm}^2$ area.

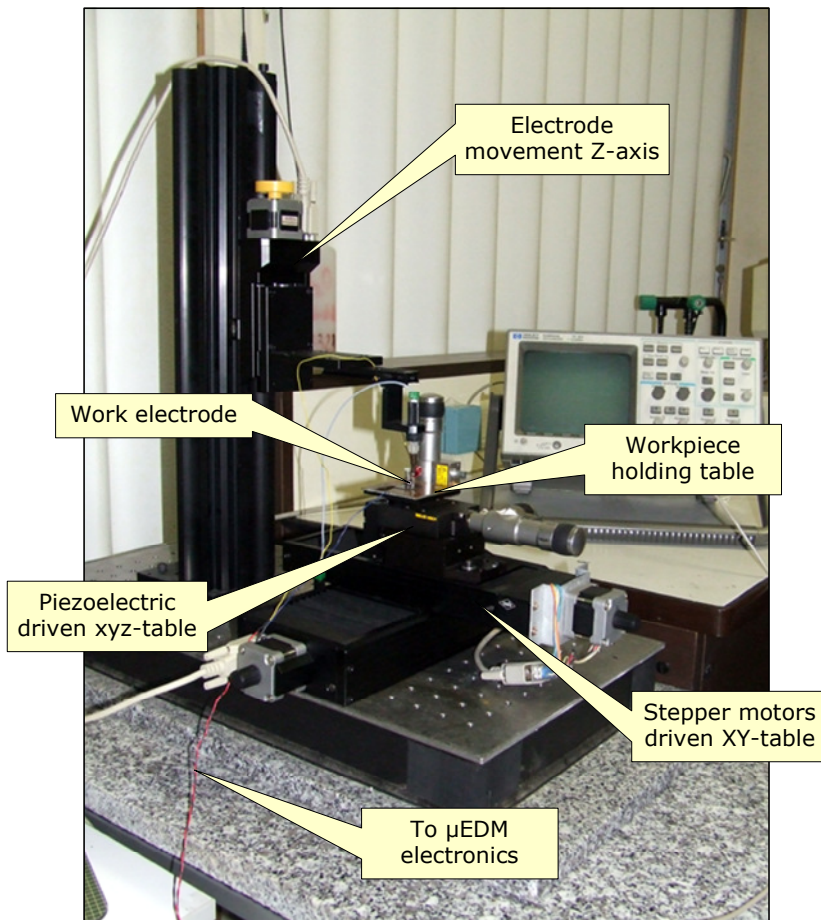


Figure 8.8

EDM setup mechanics
general view.

A second table driven with XYZ piezoactuators is mounted on the first one (Figure 8.8). We use Melles-Griot piezoactuators, with feedback correction, which provide 10 nm displacements along 30 μm range. The Piezo-driven table carries a workpiece holder, which can be either a plain copper electrode (Figure 8.9) or a cavity for keeping EDM dielectric liquid (Figure 8.10, left).

The stepper motors are controlled by a SM-32 board installed in a host PC. The piezoelectric driven table is controlled by a Melles-Griot 3-channel driver connected to the μEDM electronic board.

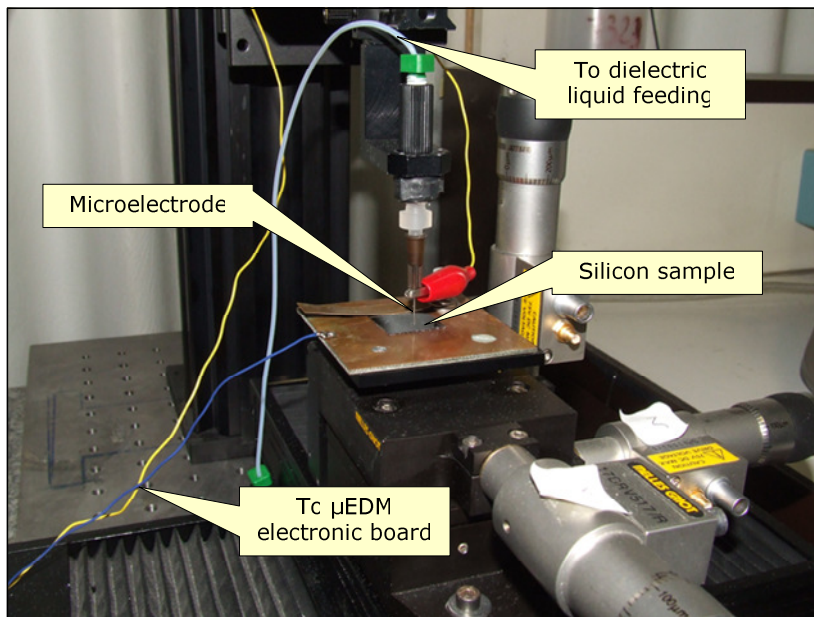


Figure 8.9

EDM setup workpiece holding table and microelectrode view.

In the figure below on the left, there is a general view of the machine with actuators electronics and the internally developed electronics for discharge pulses producing, which will be discussed below. On the right, there is a focus on a teflon tank, which is used to contain the dielectric.

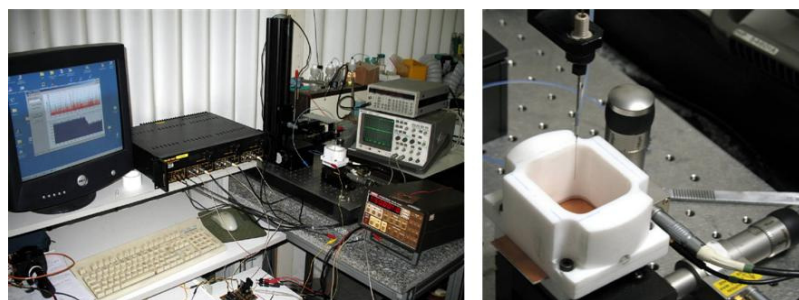


Figure 8.10 EDM setup at INL

2.3. EDM power generator

The generation of short ramp electrical pulses is needed throughout this work. The most important aspect for having a well controllable spark-erosion process is to pass a finite energy in every discharge pulse. Possible practical limitations of the machining may be set by the performance of the electronics and not by the physical or chemical principles underlying the processes. For example the resolution and the surface roughness of the parts machined by μ EDM depend on the minimum amount of electrical energy which can be accurately delivered to the electrode tool. Therefore different parameters will be adjusted (voltage, repetition rate) but at extreme low power. The capacitance of the electrode-part system, the stray capacitance of the machine in general and the parasitic capacitance of the electronic components may be important in this case. Therefore we have developed specialized

electronics for high speed pulses (25 ns of ramp) with a voltage of 1—100 V at programmable repetition rate (up to 50 kHz) so as to deliver energetic pulses from μJ to mJ level. In most cases RC-generator schemes is used as a spark source [172]. Different principles can be used to generate these pulses: RC relaxation circuit with discrete components, bipolar transistors relaxation RC circuits or even transmission RC line. In order to give some flexibility to the monitoring of the EDM process, we decided to use RC circuits controlled by fast ignition gate bipolar transistors IBGT with (25 ns switch time).

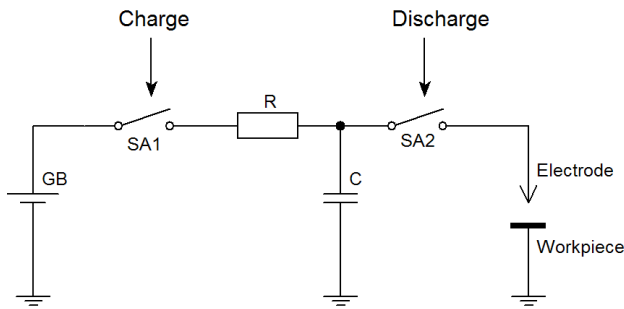


Figure 8.11

Basic RC-pulse EDM schematic.

So, the basic EDM setup electronics (Figure 8.11) consists of a voltage source GB, a capacitance C (as storage of finite charge), electrode and workpiece having spark-gap between each other, and a control system of switches SA1, SA2 to charge the capacitance and further discharge through the electrode-workpiece gap. The capacitance charging time is defined by RC value ($t_{\text{charge}} \sim RC$). The resistance R is basically used as a current limiter for the charging source GB, and is set to 100Ω in our device to protect the source. After the charge passed, the capacitance will hold energy equals to $CU^2/2$, where U is the source voltage. Switching on the SA2 key (while SA1 is switched off) initiates a discharge stage of EDM setup operation.

For the discharge stage from the experimental point of view we define four possibilities that can occur (Figure 8.12):

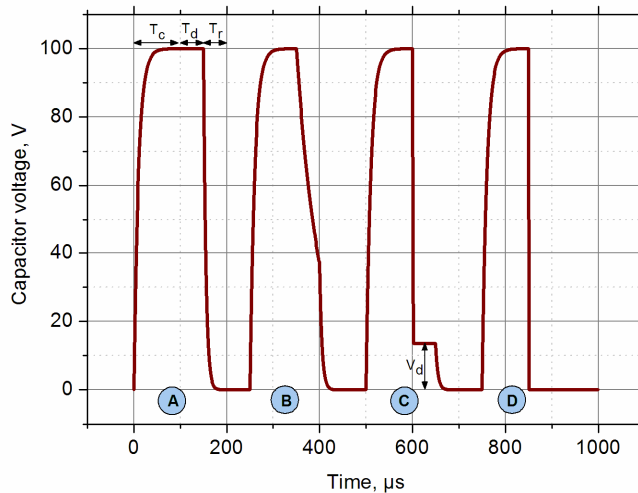


Figure 8.12

Capacitor voltage waveform for RC discharge machine (modeled signal for different discharge conditions)

$C=100\text{ nF}$

$R=100\ \Omega$

$T_c=100\ \mu\text{s}$

$T_d=50\ \mu\text{s}$

$T_r=50\ \mu\text{s}$

Repetition frequency=4 kHz

- A. The discharge does not occurs;
- B. Current leaks due to the faulty contact between electrode and workpiece;
- C. Normal discharge occurs (electrical spark between electrode and workpiece);
- D. Short circuit occurs (electrode touches a workpiece);

The first possibility (A) may happen mainly when the distance between the electrode and the workpiece is too large, or the voltage is too low to launch the ionization leading to discharge, or when the duration of the discharge pulse is too short (the time should be sufficient for electrolyte ionization and spark initiation).

Current leak (B) can be caused by a faulty contact between the electrode and the workpiece. Obviously this mode of operation is something between discharge absence (A) and a short circuit (D). Current leak (or rather charge leak) occurs when electrode actually touches the workpiece mostly through wastes (debris) of machined workpiece. Current passing through dielectric (which in this case cannot be considered as dielectric actually) can also cause this mode. Anyway, constant washing of the discharge location place and replacing of used dielectric permit to avoid this problem.

A short circuit (D) can occur when the electrode has an electric contact with the workpiece. This case is not limited to direct contact but also to a contact because of eroded debris. This mode does not lead to the workpiece machining but to the electrode and the workpiece heating and, actually, to the heating of the whole discharge circuit, caused by a short circuit current flow.

The normal discharge condition (C) is the ‘working mode’ of the EDM setup in which a spark is produced that leads to material removal. Spark discharge does not lead to a

complete capacitance discharge but stops at certain voltage V_d (referred as the discharge extinction voltage) when the dielectric polarization is not sufficient for discharge maintenance.

Actually, a stable spark-discharge can be obtained by constant balancing between mode (A) (spark absence) and mode (D) (short circuit) that can be accomplished by tracking feedback system. There is no any definite approach for this system implementation (particularly, in this work we propose several of them). Nevertheless the overwhelming majority of EDM hardware implementations uses discharge current pulses as a reference signal for feedback or the average tension between the electrode and the workpiece.

A simplified circuit schematic of μ EDM power supply implemented in this work is presented on (Figure 8.13). Full schematic can be found in the annex 1 of this thesis.

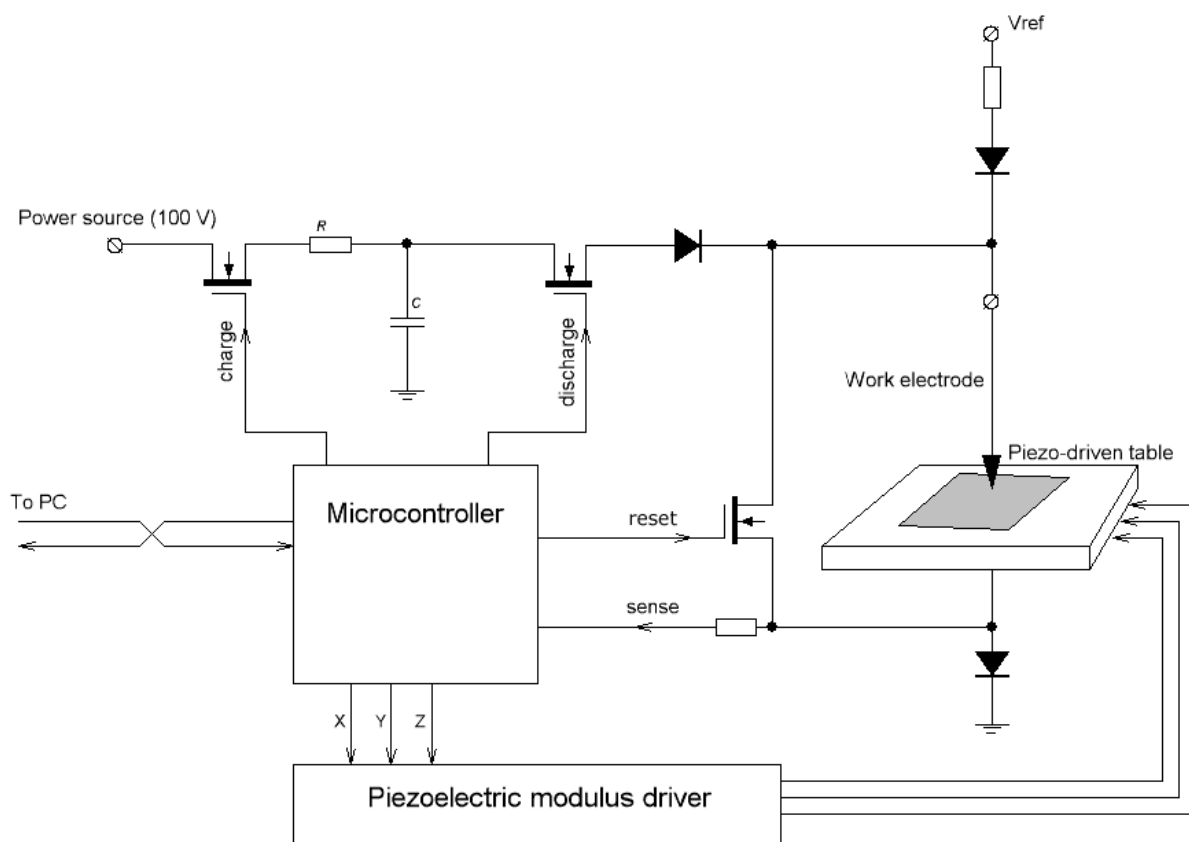


Figure 8.13 Simplified circuit schematic of the automated μ EDM setup

The μ EDM circuit is composed of three switches implemented by fast-switching IGBT transistors (fast FET-transistors can be used as well as shown in circuit schematic). The first switch, controlled by the 'charge' signal allows charging the working capacitor C through the current limiting resistor R by using an external power source. The second switch, controlled by the 'discharge' signal, closes the capacitor on the electrode-workpiece gap producing a discharge of the capacitor. The third switch, controlled by the 'reset' signal, is

used to implicitly reset the residual charge of capacitor (or even the whole charge if the spark did not occur). A voltage drop on the diode connected to the workpiece is used as a reference to produce the feedback signal, called ‘sense’. The RC-charge/discharge process is fully controlled by the microcontroller (MCU) which communicates with a host computer. MCU also controls the positioning of a sample against the working electrode by sending appropriate voltages to the positioning modulus of the piezo-driven table (stepper motors are controlled directly by the host computer via SM-32 card).

Thus, a single spark-discharge pulse formation is described by the following control signals waveforms (Figure 8.14):

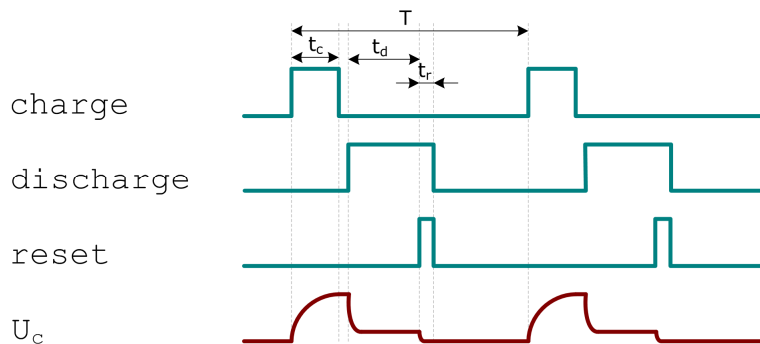


Figure 8.14

μEDM control signals waveform.

T — spark pulse period;
 t_c — charge time;
 t_d — discharge time;
 t_r — reset time.

The sequential following of ‘charge’, ‘discharge’, and ‘reset’ pulses produce a pulsed charge stored by the capacitor. The capacitor’s voltage pulses U_c are shown in Figure 8.14, (red curve) for the case of a normal spark-discharge. The typical timings are listed in Table 8.1.

Table 8.1 Typical EDM pulses timing values

Value	Typical range	Notes
t_c	10 μ s—10 ms	Depending on the used capacitance values and the voltage
t_d	5 μ s—100 μ s	During this time the discharge key is kept on. The real discharge can occurs at any time during this period.
t_r	5 μ s	The time to reset the residual charge. This time is fixed and cannot be changed programmatically.
T	20 μ s—20 ms	This time obviously depends on all upper timing values.

2.4. Discharge control techniques

As it was mentioned above, the EDM system should constantly balance between the open circuit (Figure 8.12, A) and short circuit (Figure 8.12, D) modes to maintain a stable spark discharge (Figure 8.12, C). Usually, this is achieved by monitoring the discharge current. However, this current does not always correspond to a normal spark discharge (which leads to material removal), but also can be caused by short circuit and charge leaks via electrode-workpiece debris. In this work we propose several methods for the monitoring of EDM discharge to obtain a stable machining process.

2.4.1. Control by tool-workpiece gap adjustment

The most evident approach to produce stable sparks is to maintain constant conditions of discharge. The voltage applied between the electrode and the workpiece can be easily sustained constant during the discharge pulse. However, spark erosion leads to tool wear, and thus, the gap between electrode and workpiece does not remain constant. As far as spark formation is a stochastic process, the simple tool wear compensation does not allow maintaining a constant distance between the tool and workpiece. So, regular electrode Z-position adjustment should be implemented to ensure that we have a desired gap to launch the spark.

Thus, in order to stabilize a spark, the first proposed scheme is to implement a vertical repositioning of the work electrode after each spark pulse passed. The repositioning process consists of moving the electrode towards the workpiece surface till touch (controlled by electrical contact while applying V_{ref} , Figure 8.13) and further elevation of the electrode to a defined position. In such way, we can be sure, that the distance between the electrode and the workpiece surface is always fixed. The following scheme (Figure 8.15) illustrates the process:

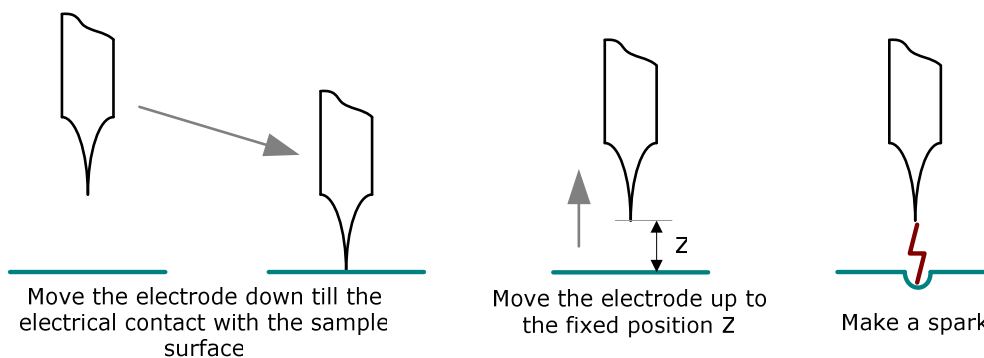


Figure 8.15 The scheme of maintaining of the constant distance Z between the electrode apex and workpiece surface.

The implementation of this method, however, did not bring a positive result, mainly, due to the microelectrodes deformation during the phase of ‘surface touching’. Indeed, the workpiece surface (which is silicon in our case) is oxidized during spark-erosion process. This leads to conductivity degradation and the electronics tries to establish a contact between the tool and workpiece by driving the electrode too strong into the workpiece. This inevitably leads to tool deformation (Figure 8.16). Thus, in spite of the fact that the first discharges were well controllable, this method can not be used for durable EDM process.

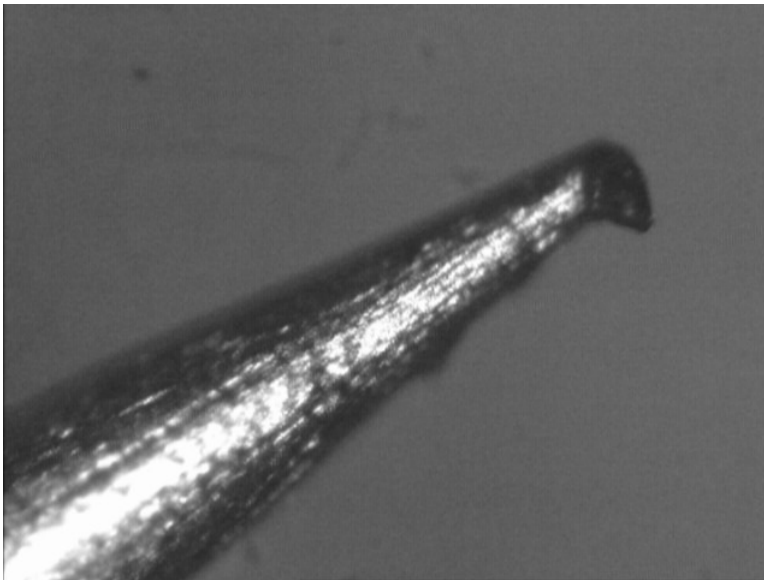


Figure 8.16

Deformation of microelectrode after trying to ‘find a surface’ of a workpiece.

2.4.2. Control by graduate approaching

After a failure of the earlier described gap control method, our thought was to descend the tool gradually towards the workpiece surface while sending spark pulses. In this way a spark *have to* occur at a certain distance between the tool and the workpiece. Although we cannot figure out this distance, this is actually not required to launch ‘good’ sparks in such manner. Obviously, the electrode will never touch the surface of a workpiece, unlike a spark never occurs during the whole ‘approach’ phase. The following scheme (Figure 8.17) demonstrates the algorithm described:

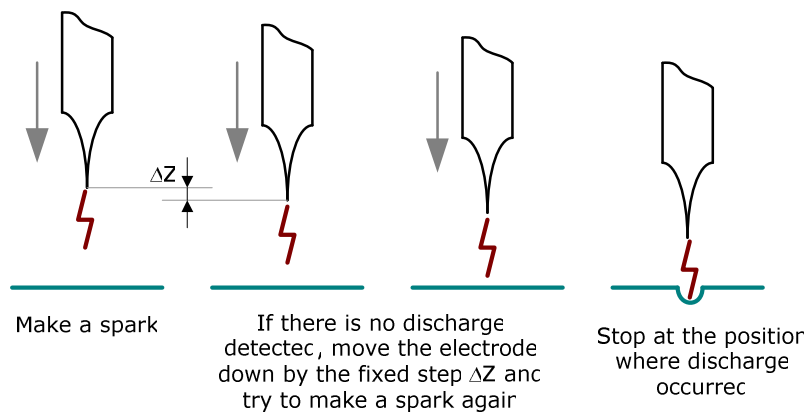


Figure 8.17 Graduate approaching of the electrode by fixed steps ΔZ . The spark is tried after each step down.

This algorithm can be even more simplified as far as we do not need to pass the whole charge-discharge cycle (Figure 8.14) after each step down, but we can keep the capacitor charged while moving the electrode down gradually to the workpiece till the discharge occurs. The optimized algorithm is represented by the following scheme (Figure 8.18):

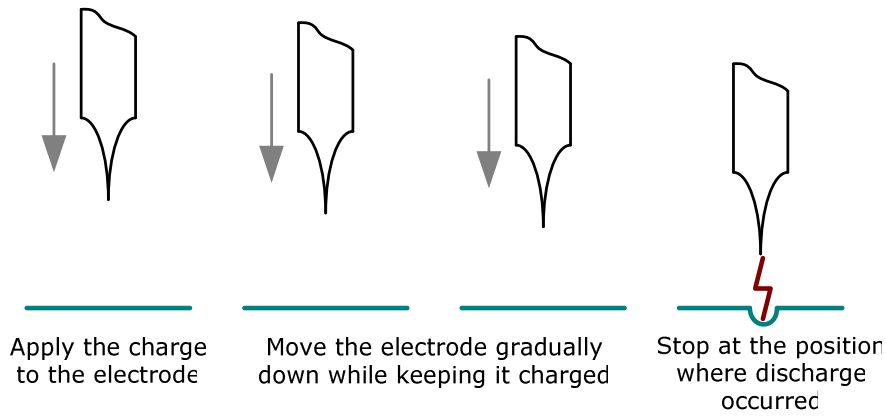


Figure 8.18 Smooth graduate approaching of the electrode till the spark occurrence detected.

As predicted, the proposed algorithm does not lead to tool-workpiece direct contact and produces stable discharge for each pulse launched. Particularly, this approach was chosen by us to implement a silicon surface micro-patterning by EDM process. Figure 8.19 demonstrates the result of silicon surface machining implementing the spark control method described. The method appears to be very reliable as far as each discharge pulse leads to a crater formation on silicon surface (Figure 8.19). However, the approach phase is rather slow, allowing launching no more than a couple of sparks per second.

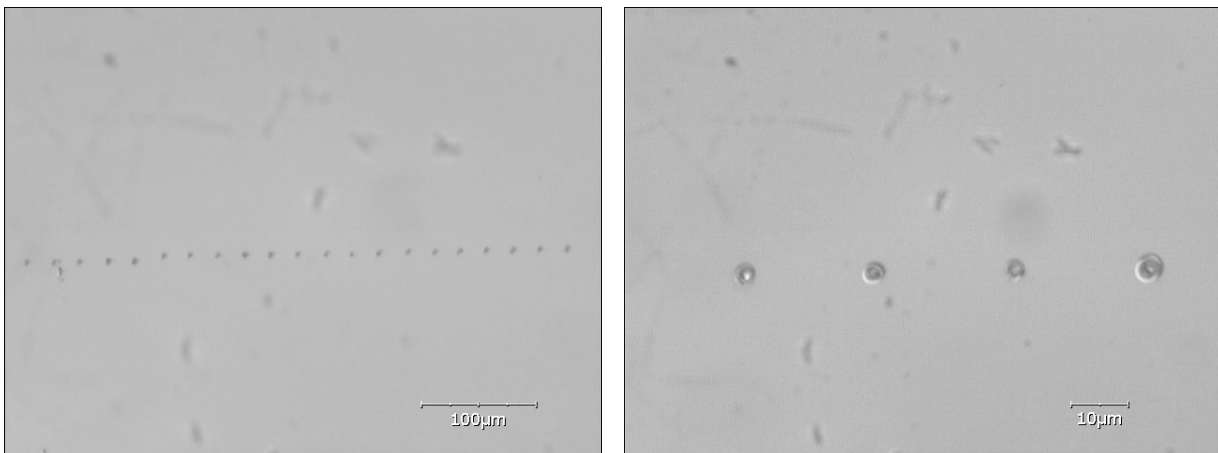


Figure 8.19 Series of sparks performed in air viewed by optical microscope. The following μ EDM parameters were used: $U=30$ V, $C=33$ nF ($W=14.85$ μ J).

2.4.3. Digital control of a spark

Despite the fact that the gradual approach of the tool always leads to a spark formation, this method is too slow and cannot be implemented in machining complex structures during reasonable time. So, we paid our attention to the ‘sense’ feedback signal (Figure 8.13) for different discharge conditions (Figure 8.12). The following waveforms (Figure 8.20) depict the behavior of the μ EDM system. As one can see, each time the capacitor is discharged (via the tool-workpiece gap or via the reset switch), the ‘sense’

signal is triggered. We can use a certain discrimination level to convert the ‘sense’ signal pulses into TTL pulses that can be treated directly by the MCU.

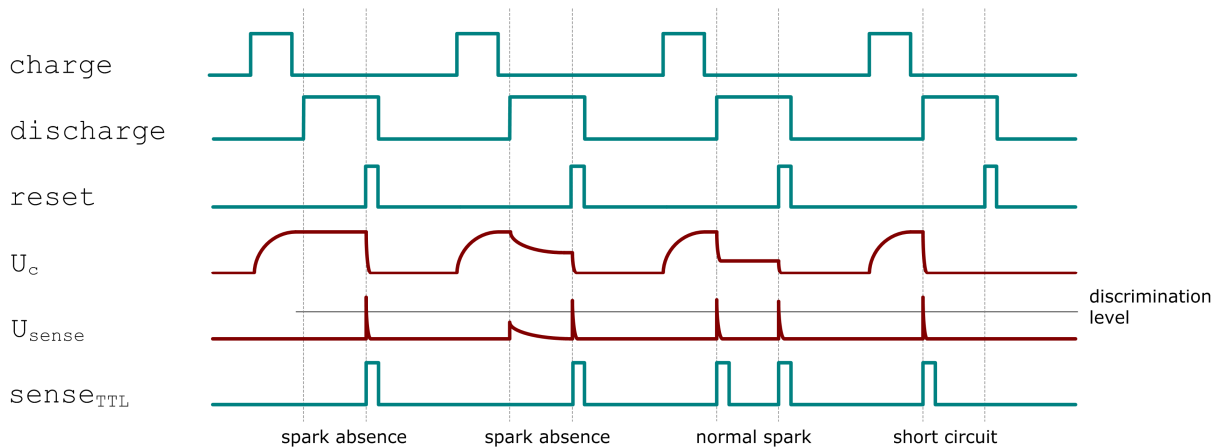


Figure 8.20 μ EDM control signals waveform according to the circuit schematic represented in (Figure 8.13).

Thus, receiving a ‘sense_{TTL}’ feedback just after the ‘discharge’ pulse means that some current flows via the tool-workpiece gap. This can be a spark discharge or a short circuit current. To clear this, we follow the ‘sense_{TTL}’ feedback during the reset stage. In this case, receiving a feedback means that some current flowed through the reset switch (Figure 8.13) i.e. the capacitor held some charge just before the reset stage. This way following the ‘sense’ pulses feedback, allows to make a decision whether a spark was good or not. The algorithm for such kind of an operation is represented by the following scheme (Figure 8.21).

The proposed scheme of spark controlling showed a good reliability during our experiments on μ EDM. It assures a fast feedback on spark and thus provides a great number of ‘good sparks’ among charge-discharge cycles (repetition rate 1—10 kHz). So, as far as the spark quality is guaranteed by automatics, we can move a workpiece while the spark generator remains operating and in this way provide an engraving mode by milling EDM.

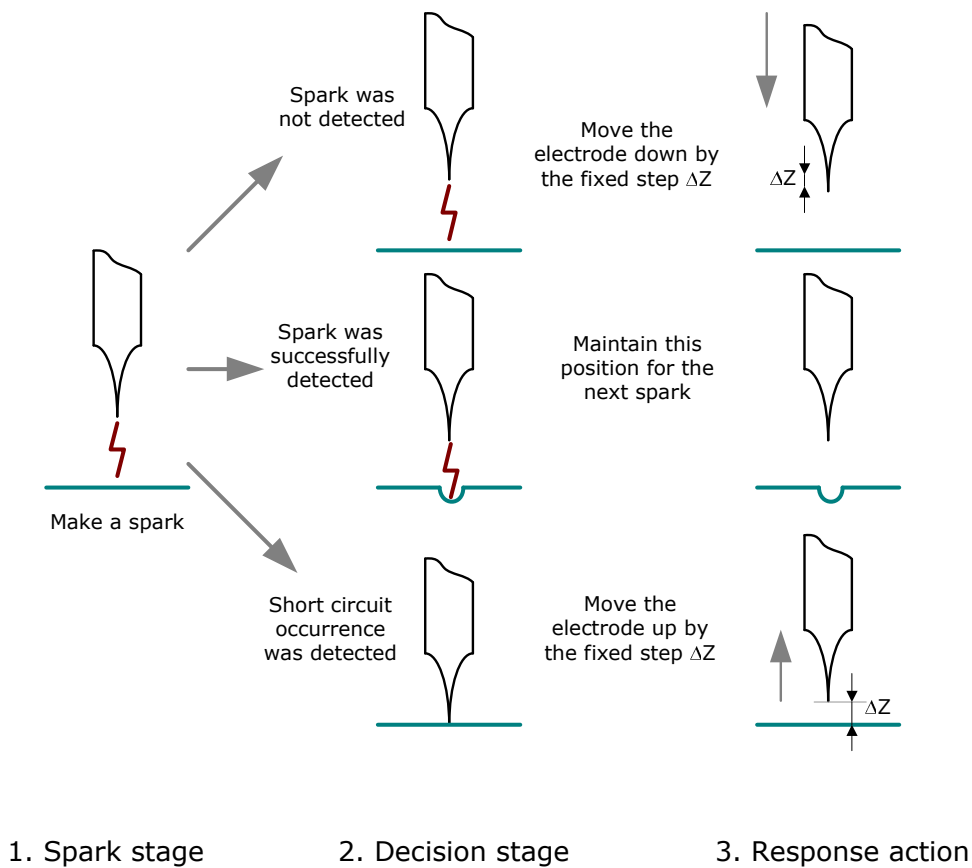


Figure 8.21 Complex spark-decision-response scheme of digital spark controlling proposed for fast and reliable machining.

2.5. μ EDM control software

To control the μ EDM setup, a special software was developed. This software includes a simple programming language compiler and execution environment. It works under MS Windows operating system and communicates with μ EDM control unit via a RS-232 communication port. A special language was developed to describe the machining design and set up all parameters (such as control pulses delays). The compiler converts an input design script to a bytecode that will be sent to μ EDM unit MCU during the machining process and also generates a schematic view of a future machining result. This design view can be used for script verification and adjustment before launching a real machining process. The bytecode generated by the compiler is interpreted by the μ EDM controller that drives all the hardware of the EDM setup to perform the machining of a real sample. So, the whole design workflow can be represented as follows (Figure 8.22). More detailed description of this μ EDM design scripting language can be found in the annex 2 of this thesis.

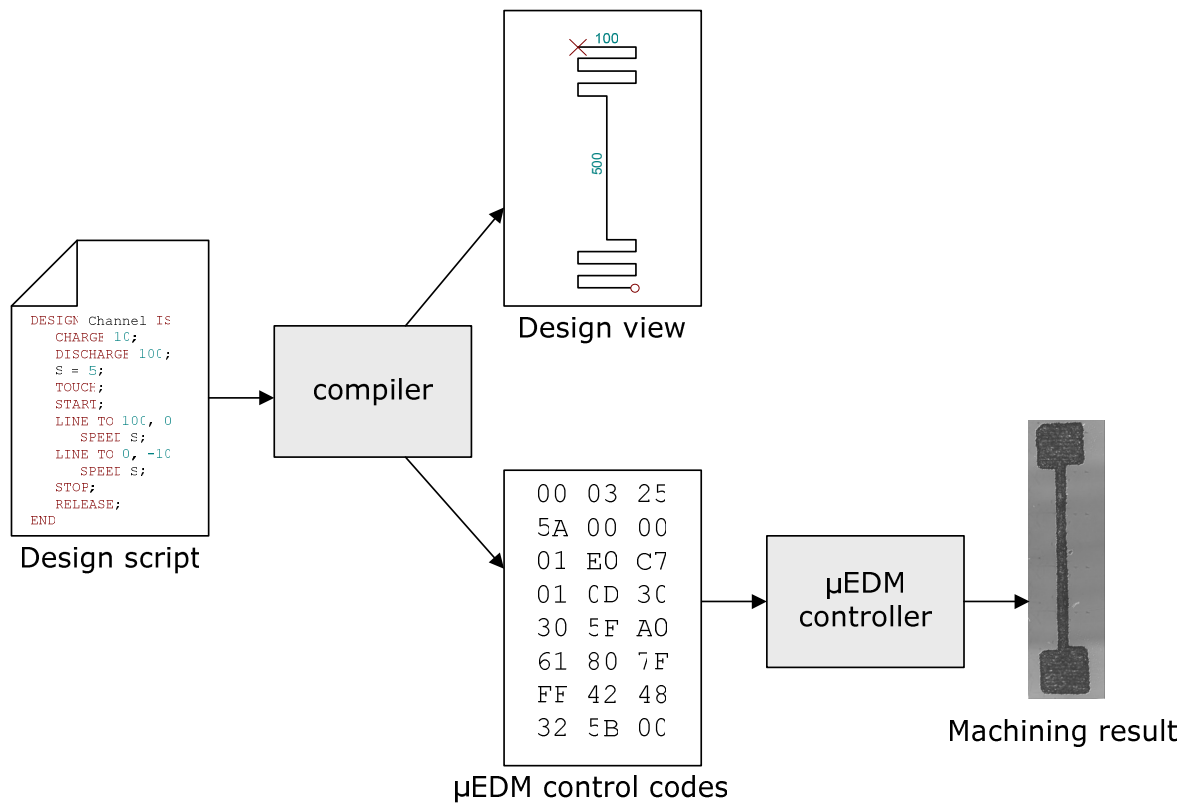


Figure 8.22 μEDM design workflow diagram.

2.6. μEDM metrology

The μEDM setup has a capability to estimate the work electrode wear by performing the direct electrical contact between electrode and workpiece. The Z-position at which this contact is detected is measured before the machining and just after it at the same reference point on the workpiece surface. Two positions are compared to calculate the tool wear. The whole process is depicted in the following figure (Figure 8.23), which shows the machining of the 250 μm line during 20 s with a Pt-Ir electrode (\varnothing 100 μm).

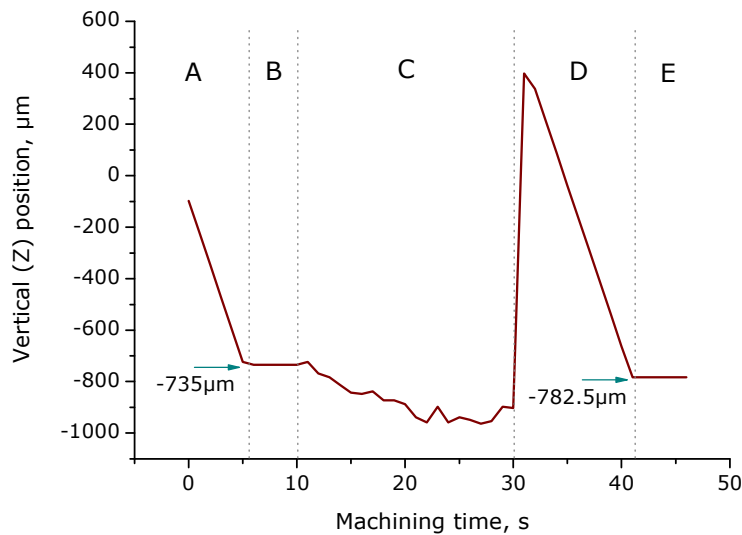


Figure 8.23

Work electrode position measured by the μ EDM setup during the whole machining cycle.

$C=1.5 \mu\text{F}$

$U=50 \text{ V}$

($W=1.8 \text{ mJ}$)

During the machining cycle the following stages are passed:

- A. Approaching phase, when the electrode touches the surface of the workpiece;
- B. Electrode vertical position estimation;
- C. Machining of some structure during a fixed time;
- D. Electrode release and repositioning to the initial reference point till the surface touch;
- E. Vertical position estimation of the electrode after the machining.

In such manner, the μ EDM setup allows us to estimate the electrode wear and machined structure depth from the curve. For this particular case the electrode wear is approximately $47 \mu\text{m}$.

3. EDM machining experiments

To illustrate the EDM setup developed capabilities, we tried to machine several simple structures. The designed μ EDM setup was preliminarily tested in ‘macro’ mode by machining features as small as $100\text{--}200 \mu\text{m}$ (that is currently a limit of industrial EDM machines) in silicon and stainless steel. Figure 8.24 shows a photo of a $100 \mu\text{m}$ copper electrode and a hole drilled by this electrode through the silicon wafer ($400 \mu\text{m}$ thickness) in approximately 20 s. A drop of deionized water was used as dielectric.



Figure 8.24

Photo of 100 μm copper electrode and a hole drilled by this electrode in p^+ silicon ($0.005 \Omega\cdot\text{cm}$) wafer.

$C=1.5 \mu\text{F}$

$U=30 \text{ V}$

The following photo (Figure 8.25) shows a channel machined in stainless steel. In this case a 100 μm tungsten wire was used as a work electrode, as far as stainless steel is a hard material with low MRR. Deionized water was used for this experiment as a dielectric liquid.

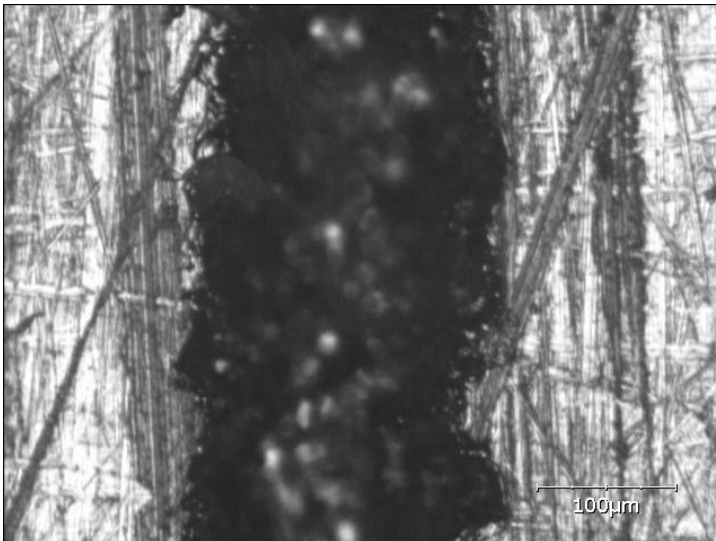


Figure 8.25

Optical microscope view of the channel machined in stainless steel by 100 μm tungsten electrode.

$C=2.2 \mu\text{F}$

$U=100 \text{ V}$

After these demonstrations of the EDM setup efficiency, we tried more accurate experiments. All the following structures were machined on p^+ -doped Si wafer with (100) crystallographic orientation.

3.1. Cavity with a tip inside

The next example demonstrates the machining of a cavity $250\times 250 \mu\text{m}$ (approximately) with a small tip inside it on a silicon substrate (Figure 8.26). We tried to make this internal tip as small as possible by adjusting design script and varying the EDM parameters. The bevel around the cavity border is drawn taking into consideration a finite

EDM electrode tip machining radius of approximately 15—25 μm , while working in engraving mode (milling EDM).

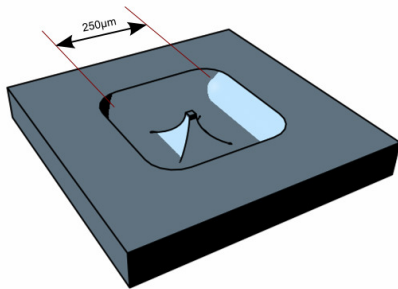


Figure 8.26

Design of a desired cavity of 250×250 μm with a tip inside it.

To accomplish the design (Figure 8.26) we decided to move the eroding tip by square spiral path from the center of the cavity (Figure 8.27).

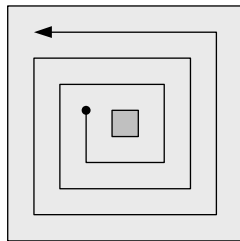


Figure 8.27

The machining path for the structure, presented in Figure 8.26.

In this way we can leave some matter inside (making desired tip) while machining the cavity deep down having smooth borders. Thus, a possible machining script can be as followed (this script takes into consideration that the motorized table has precision of 2.5 $\mu\text{m}/\text{step}$):

```
/**
 * cavity1.edm
 * Machining of a spiral path inside out,
 * leaving some matter in the center
 * 12/03/2007 Arthur Benilov
 */
DESIGN CavityWithTip IS
  CHARGE 10; // Charge time
  DISCHARGE 100; // Discharge time
  S = 7; // Machining speed (steps per second)
  Cycles = 5; // Number of machining cycles
  TOUCH; // Touch sample's surface by electrode
  START; // Starting pulse generator
  REPEAT Cycles IS
    LINE TO 0, -30 SPEED S;
    LINE TO 30, 0 SPEED S;
    LINE TO 0, 40 SPEED S;
    LINE TO -40, 0 SPEED S;
    LINE TO 0, -50 SPEED S;
    LINE TO 50, 0 SPEED S;
    LINE TO 0, 60 SPEED S;
    LINE TO -60, 0 SPEED S;
    LINE TO 0, -70 SPEED S;
    LINE TO 70, 0 SPEED S;
    LINE TO 0, 80 SPEED S;
    LINE TO -80, 0 SPEED S;
    LINE TO 0, -90 SPEED S;
```

```

LINE TO 90, 0 SPEED S;
LINE TO 0, 100 SPEED S;
LINE TO -100, 0 SPEED S;
LINE TO 0, -100 SPEED S;
RELEASE; // Move electrode up
MOVE TO 40, 60; // Move to the initial position
END;
STOP; // Shutting down pulse generator
RELEASE 1000; // Moving electrode up by 2.5mm
END.

```

The following series of photos show five attempts to machine this geometry while changing EDM parameters (voltage, capacitance, machining speed, and the number of machining cycles). Each photo represents a view by optical microscope of the whole cavity ($\times 10$ magnification) and the central part with a tip ($\times 50$ or $\times 100$ magnifications).

Figure 8.28 demonstrates the very first result of machining according to the designed script. The energy in the spark was rather high here as well as the machining speed (movement of the tool-electrode while spark erosion). At such a high energy, one can notice the formation of large craters (approx. $5\text{--}8\ \mu\text{m}$ in diameter). However, this machining result shows that the description of the contour in the script is correct.

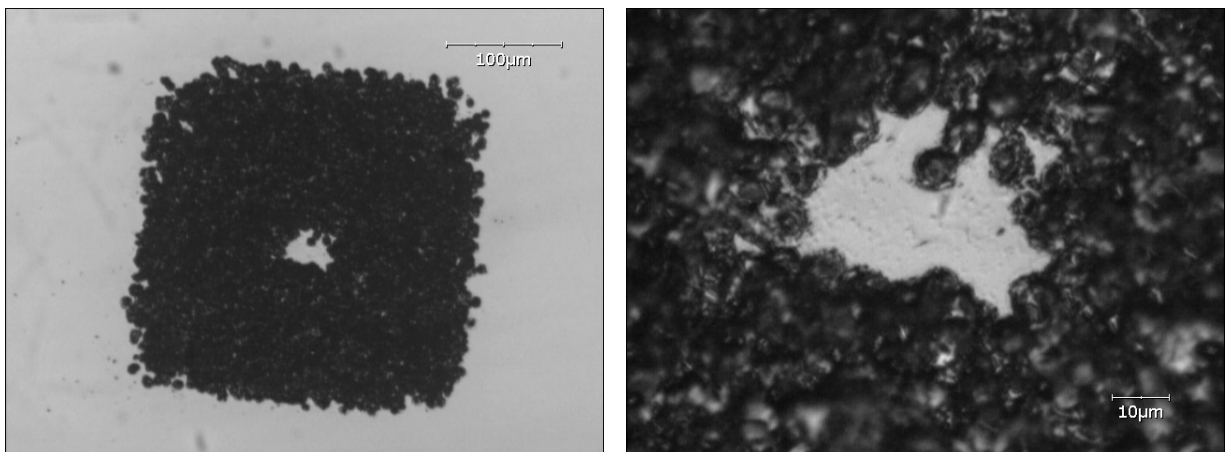


Figure 8.28 Optical microscope view of machined cavity. Machining parameters: $U=30\ \text{V}$, $C=33\ \text{nF}$, $\text{speed}=12.5\ \mu\text{m/s}$, single machining cycle.

Changing the EDM parameters improves somehow the machining quality (Figure 8.29 — Figure 8.32). Particularly, the decrease in the spark energy leads to smoother eroded surface (a $4.7\ \text{nF}$ capacitor finally gave $1\text{--}2\ \mu\text{m}$ features scale).

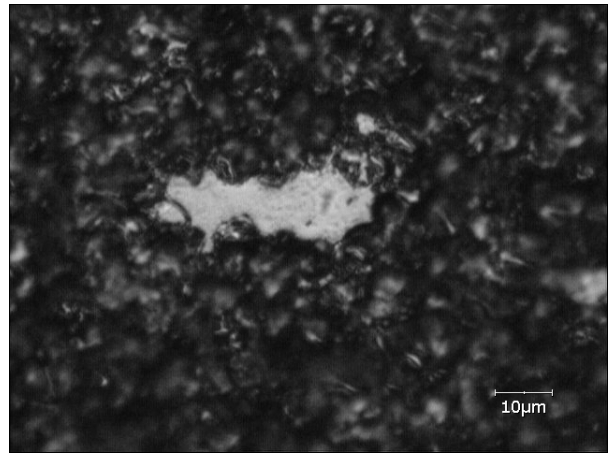
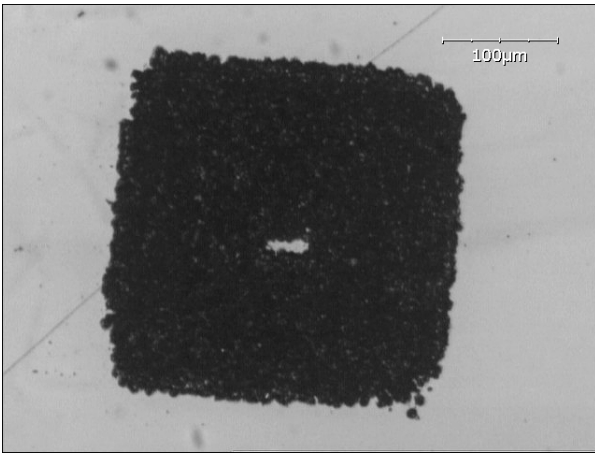


Figure 8.29 Optical microscope view of machined cavity.
Machining parameters: $U=30$ V, $C=33$ nF, speed= 7.5 $\mu\text{m/s}$, single machining cycle.

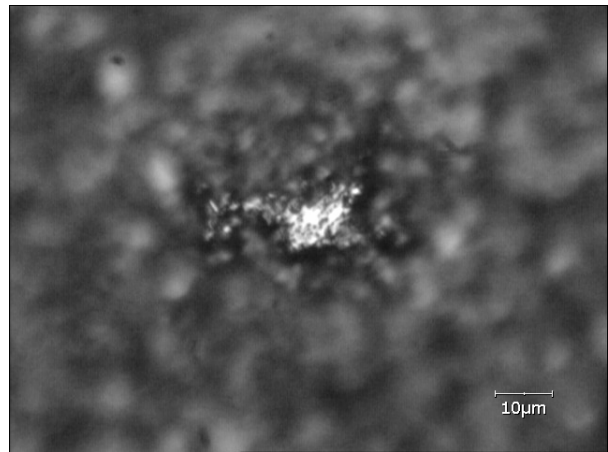
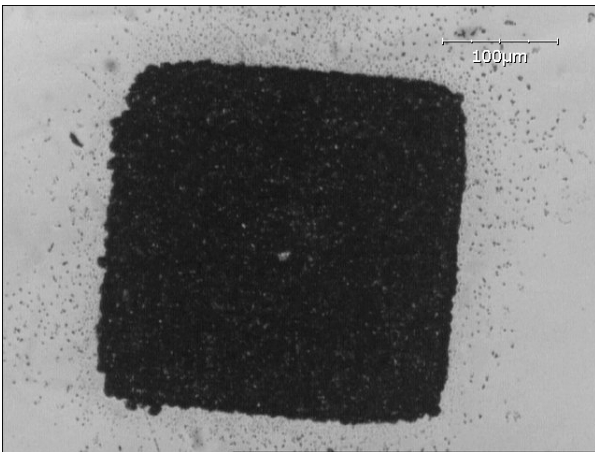


Figure 8.30 Optical microscope view of the machined cavity.
Machining parameters: $U=30$ V, $C=33$ nF, speed= 17.5 $\mu\text{m/s}$, 5 machining cycles.

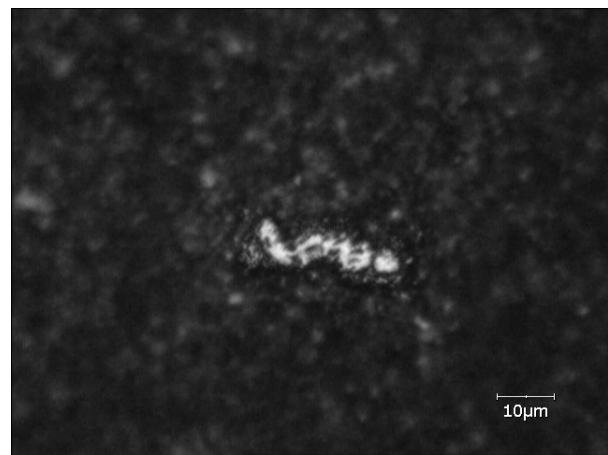
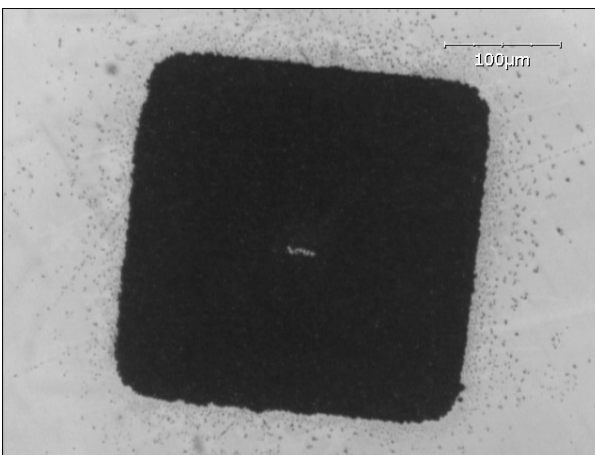


Figure 8.31 Optical microscope view of the machined cavity.
Machining parameters: $U=30$ V, $C=4.7$ nF, speed= 7.5 $\mu\text{m/s}$, 5 machining cycles.

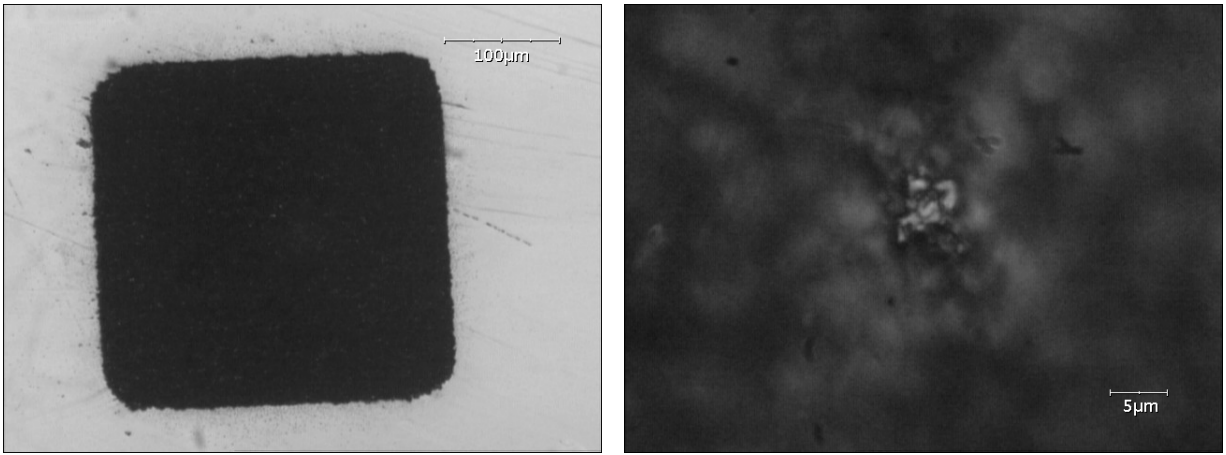


Figure 8.32 Optical microscope view of the machined cavity. Machining parameters: $U=30$ V, $C=4.7$ nF, speed= 5 $\mu\text{m/s}$, 4 machining cycles.

The last machining experiment (Figure 8.32) gave us a tip as small as 5 μm . A SEM view of this cavity (Figure 8.33) allows estimating the depth of the cavity (20 μm approximately). To conclude, we can mention that the achieved resolution is compatible with micromold manufacturing. This is very promising for the fabrication of microparts by polymer injection at elevated temperature.

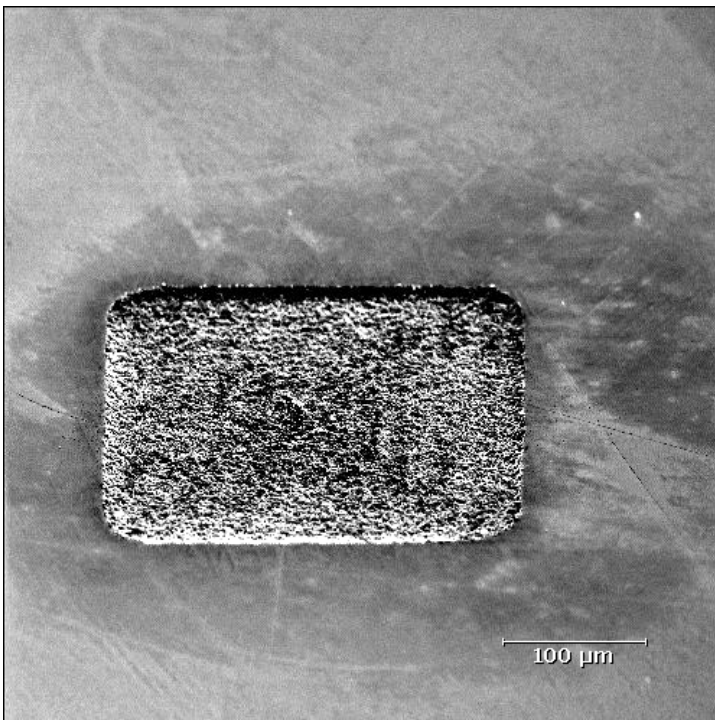


Figure 8.33 SEM view of the cavity presented also in Figure 8.32.

3.2. Microchannel with two cavities

The following example demonstrates the machining of a channel (1.25 mm in length, 50 μm in width) with two cavities (250×250 μm) on both ends of it (Figure 8.34). Such a


```

        LINE TO 0, -dY SPEED S;
    END;
    LINE TO CX/2, 0 SPEED S;

    /* Channel */
    LINE TO 0, -CH SPEED S;

    /* Second cavity */
    LINE TO CX/2, 0 SPEED S;
    REPEAT CY/dY/2 IS
        LINE TO 0, -dY SPEED S;
        LINE TO -CX, 0 SPEED S;
        LINE TO 0, -dY SPEED S;
        LINE TO CX, 0 SPEED S;
    END;

    STOP;           // Shutting down EDM pulse generator
    RELEASE 200;    // Move electrode up by 200 motor steps (0.5mm)
    MOVE TO -CX, 2*CY + CH; // Move to the initial position

    END;           // End of cycle

    RELEASE 1000;  // Move electrode up by 1000 motor steps (2.5mm)

    END.

```

The result of the machining is represented on the following figures.

The machining energy for the experiment of Figure 8.36 was rather high, resulting in formation of a deep channel having a high roughness.

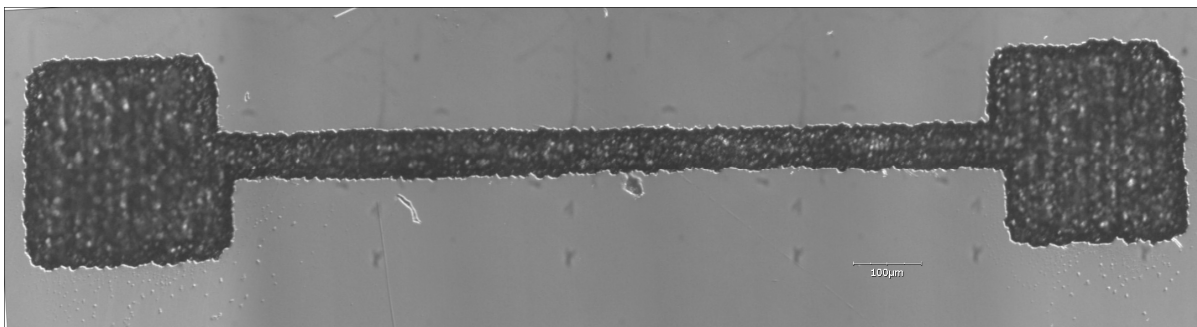


Figure 8.36 Optical microscope view of machined channel. Machining parameters: $C=33$ nF, $U=30$ V, machining speed= 25 $\mu\text{m/s}$, single machining cycle.

Figure 8.37 shows what happens when the machining speed is too high. Actually the engraving of the sample is rather poor here, so for the further tests the machining speed was turned down.

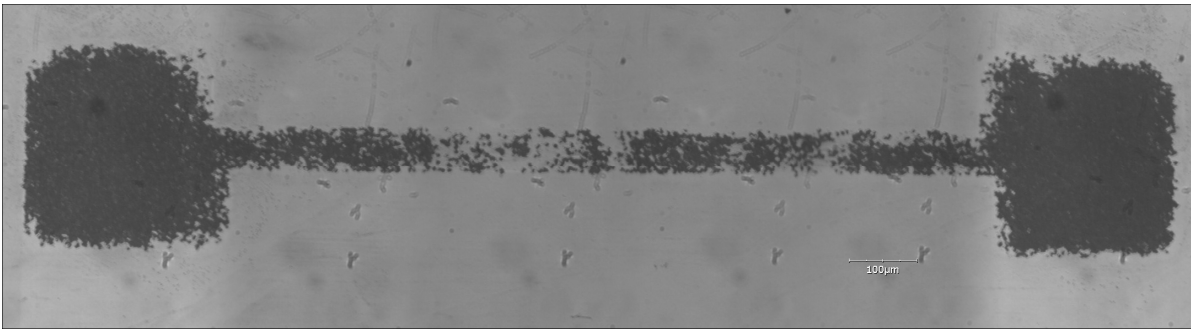


Figure 8.37 Optical microscope view of machined channel. Machining parameters: $C=4.7$ nF, $U=30$ V, machining speed= 10 $\mu\text{m/s}$, single machining cycle.

Figure 8.38 shows the result of the machining at a low electrode movement speed.

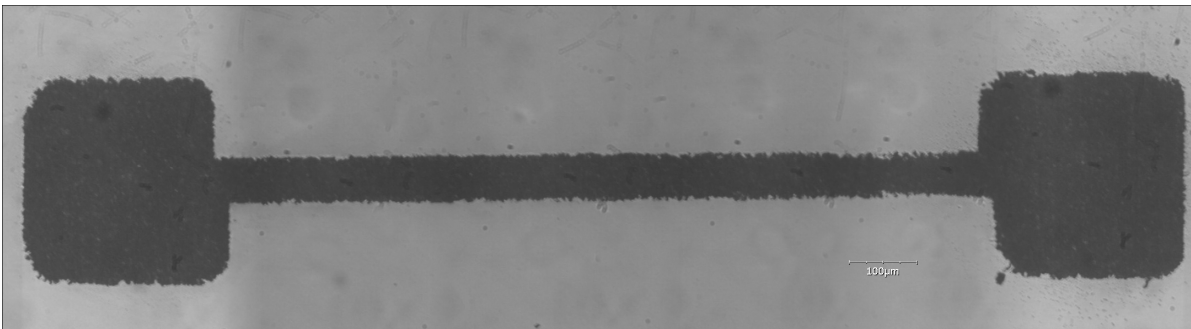


Figure 8.38 Optical microscope view of machined channel. Machining parameters: $C=4.7$ nF, $U=30$ V, speed= 2.5 $\mu\text{m/s}$, single machining cycle.

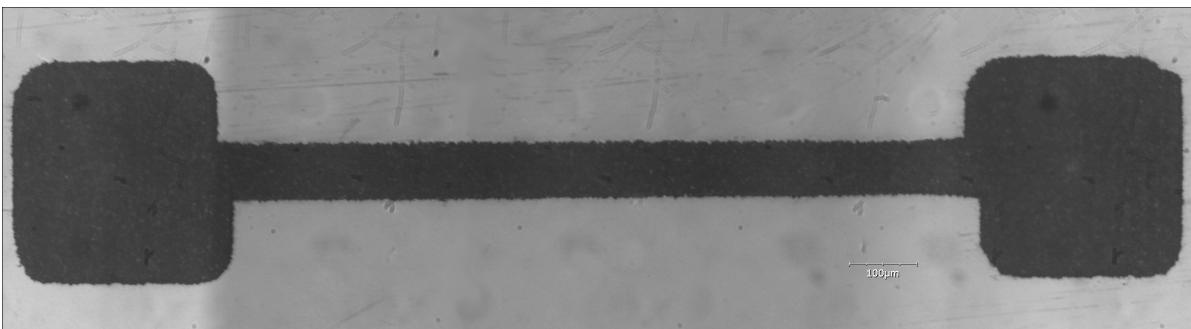


Figure 8.39 Optical microscope view of machined channel. Machining parameters: $C=4.7$ nF, $U=30$ V, speed= 2.5 $\mu\text{m/s}$, 3 machining cycles.

The final machining test (Figure 8.39 and Figure 8.40) shows a deep channel (50 μm approximately).

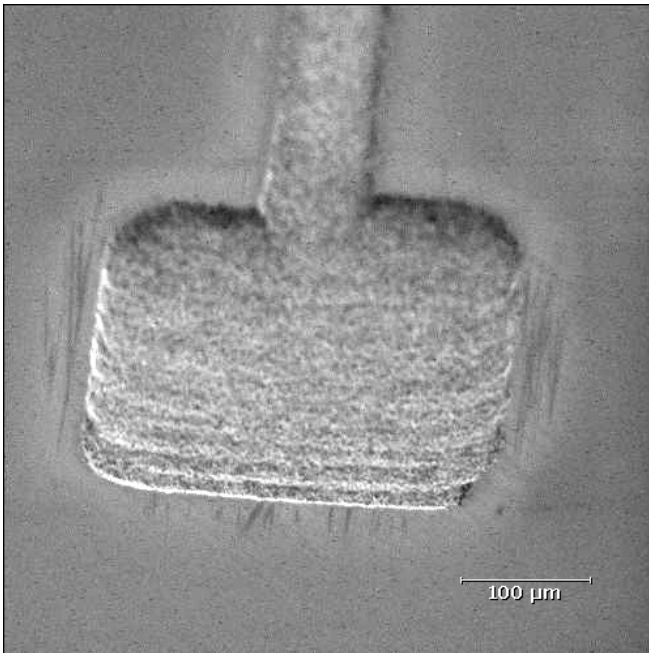


Figure 8.40

SEM view of the channel, presented also in Figure 8.39.

All these examples shows interesting 3D geometry but the resolution is limited to several tens micrometers. We tried to overcome this resolution threshold by establishing more precise μ EDM technique.

3.3. Towards the μ EDM

The very first experiments were carried out without any dielectric liquid, so the sparks occurred by breakdown in air between the sample and the tip. As workpiece, we used a silicon wafer, p^+ -doped ($0.001 \Omega \cdot \text{cm}$) with (100) crystallographic orientation.

Actually, single sparks in air cannot lead to any significant machining rates as far as the eroded material is not removed from the spark local area. Anyhow, our idea was to test the electronics to create features as small as possible according to the diameter of the electrode, prepared according to the process previously described. The first test was made by implementing a series of sparks spaced by $25 \mu\text{m}$ using the gradual electrode approach technique (Figure 8.19). One can see that the series of sparks formed craters on silicon surface of approximately $5 \mu\text{m}$ in diameter (the actual diameter varies from $4 \mu\text{m}$ to $6 \mu\text{m}$). These craters were measured using SEM and AFM techniques. A view of a typical crater formed by a single spark on silicon surface is shown in Figure 8.41.

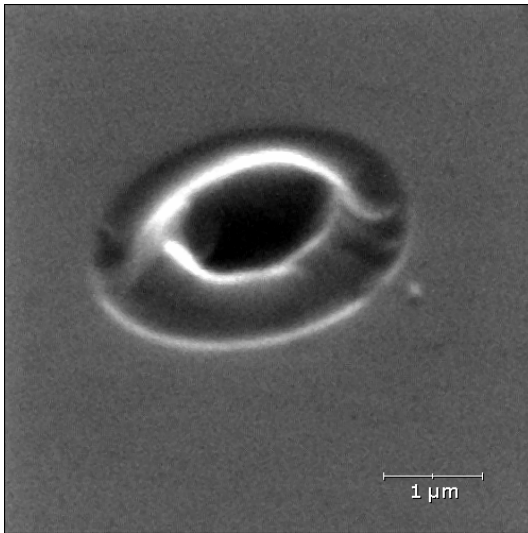


Figure 8.41

SEM view of a crater formed after a single spark on silicon surface.

$C=4.7$ nF

$U=30$ V

($W=2.1$ μJ)

As far as SEM gives us a general view of a crater, but no profile to measure the structure, we passed to AFM microscopy. AFM scans show that the craters have almost perfect round shape of 2—3 μm in diameter (Figure 8.42). This can be explained by the fact that the local melting of silicon after the spark impact leads to the formation of a circular wave of molten silicon on the surface. So, the craters that we see are just solidified waves.

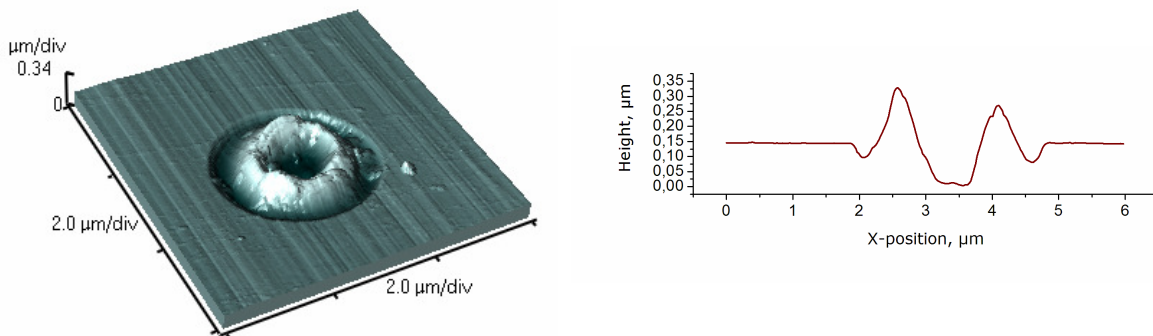


Figure 8.42 AFM 3D view and profile of a crater formed after a single spark on silicon surface (machining parameters: $C=4.7$ nF, $U=30$ V, $W=2.1$ μF).

Enabling silicon simple displacement (by piezo-driven table) allows us manufacturing more complex structures (Figure 8.43). As this sample was also machined in air, there was no significant material removal from the spark craters. There were many errors in the sparks positioning and also void sparks due to the silicon debris that were not removed from the surface.

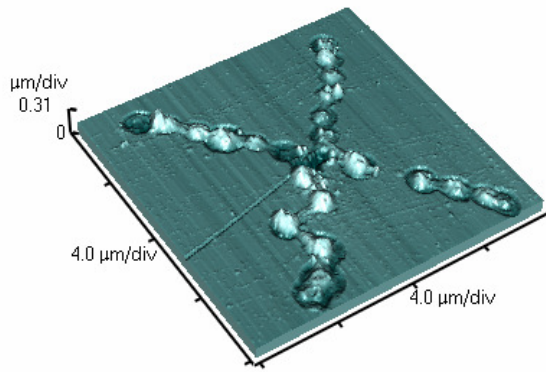


Figure 8.43

AFM view of an X-pattern ($12 \times 12 \mu\text{m}$) machined as a series of separate sparks in air. Each spark was made by the graduate approach method (machining parameters: $C=4.7 \text{ nF}$, $U=30 \text{ V}$, $W=2.1 \mu\text{J}$).

For better material removal and surface quality improvement the machining process should be carried out in a dielectric liquid environment. We tried first deionized water but were unable to get stable sparks. Finally we tried successfully mixtures of glycerol:water and ethanol:water (50:50% vol.). Both mixtures gave almost the same results (in the sense of having a stable spark), Ethanol:water solution manifested high wettability with the surface of silicon. So just a small drop of dielectric liquid was placed on the workpiece for micro-machining: the ethanol:water solution just flowed away from the machining area leading to EDM process failures. So, finally the glycerol:water solution was chosen as μEDM dielectric liquid. The following sample was machined in glycerol:water mixture that allowed to improve somehow the repeatability and machining quality (Figure 8.44).

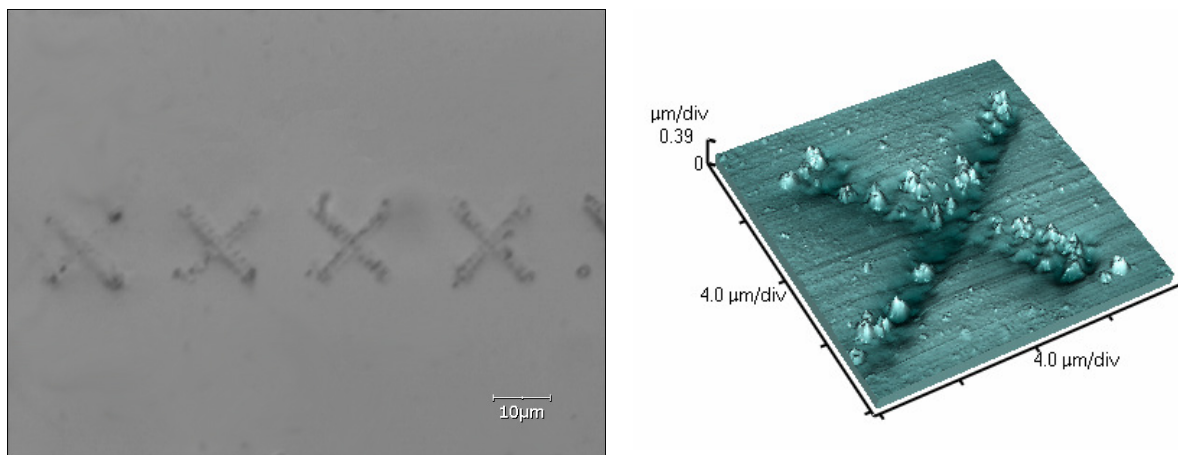


Figure 8.44

Optical microscope and AFM views of an X-pattern ($12 \times 12 \mu\text{m}$) machined as a series of separate sparks. Each spark was made by the gradual approach method while the sample was immersed in glycerol:water solution (machining parameters: $C=4.7 \text{ nF}$, $U=30 \text{ V}$).

In the future, it will necessary to better understand the relationship between the nature of the dielectric (conductibility, wettability, viscosity, etc.) and the machinability. It will be also necessary to study the flushing conditions, possibly with directed microflow through nozzles and/or additional mixing or vibrations (e.g. generated by the Z piezo actuator).

The contamination of the dielectric by the conductive debris and/or dust has also to be considered at the microscale.

Another point will be to prepare thinner electrodes. This seems possible for \varnothing 100—300 nm electrodes. It is known from previous work at INL related to the electrochemical etching of ultra thin electrodes for field emission., that single crystal W wires can be shaped with a sharp tip and deformed to high aspect ratio geometry by heating at high temperature in ultra high vacuum (UHV). The tip shape evolution during annealing in UHV is determined by the action of two mechanisms: surface diffusion and evaporation of tungsten atoms [204].

4. Porous silicon formation

As it was mentioned earlier in the first chapter of the thesis, spark processing of silicon surface can be used to produce porous silicon. According to the works of Hummel and others [12, 60, 205], to obtain nanometer-size silicon nanocrystals that manifest PL, the spark should be initiated by very high voltage (15 kV approximately) and the erosion process should be carried out for several hours. In the EDM process, the spark voltage stays in the limits of 10—300 V. Particularly in our EDM implementation the maximal voltage is limited by 100 V. So, we performed several experiments to test the possibility of porous Si formation using this setup. Finally, an additional step-up transformer was installed to elevate the spark voltage as high as 5 kV in pulsed mode.

The following photos represent the results of spark processing of p-doped 10 Ω ·cm (100) Si wafer at fixed spark voltage of 5 kV and different air gaps.

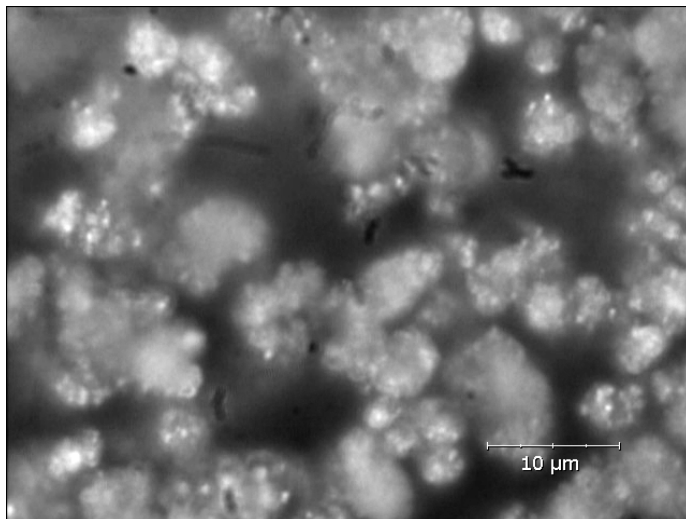


Figure 8.45

Optical microscope view of spark processed silicon surface. Discharge voltage is 5 kV, discharge gap is 2 mm approximately.

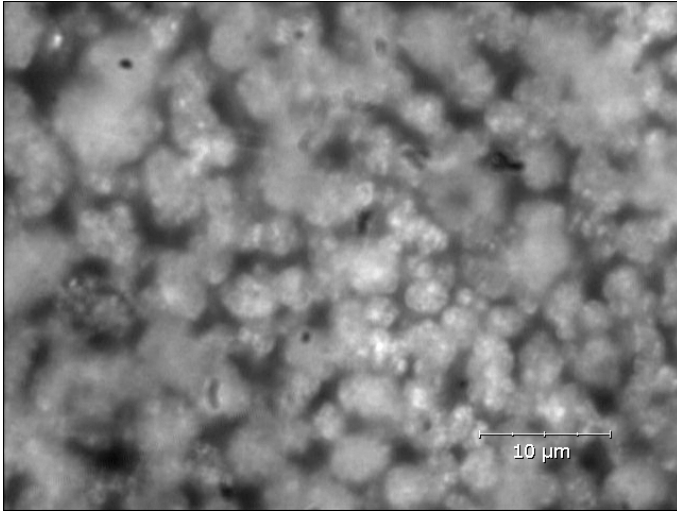


Figure 8.46

Optical microscope view of spark processed silicon surface. Discharge voltage is 5 kV; discharge gap is 1 mm approximately.

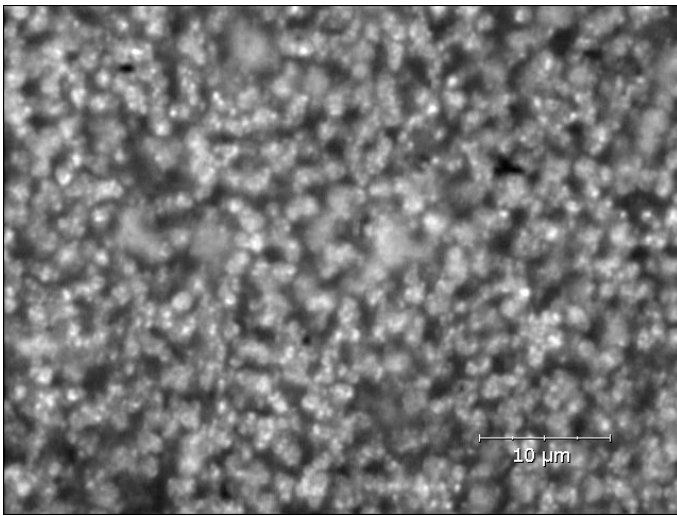


Figure 8.47

Optical microscope view of spark processed silicon surface. Discharge voltage is 5 kV; discharge gap is 0.3 mm approximately.

Using the specified processing parameters we did not manage to obtain silicon particles smaller than 0.5—1 μm, so the porous silicon formed does not manifest any photoluminescence signal and can be considered as macroporous Si. Interestingly, all samples were porosified quickly in a matter of two minutes. The distance between the electrode and the substrate was a parameter easy to adjust. So, this set up may facilitate further research, for example by moving laterally the electrode and changing the parameters of porosification.

We have noticed that during erosion process the spark streamers migrate along the sample surface along the crystallographic planes of Si crystal (Figure 8.48). It seems that, due to the high voltage, the spark can be generated at different points on the area in front of the electrode. The porosification starts first on small area and then tend to expand laterally.

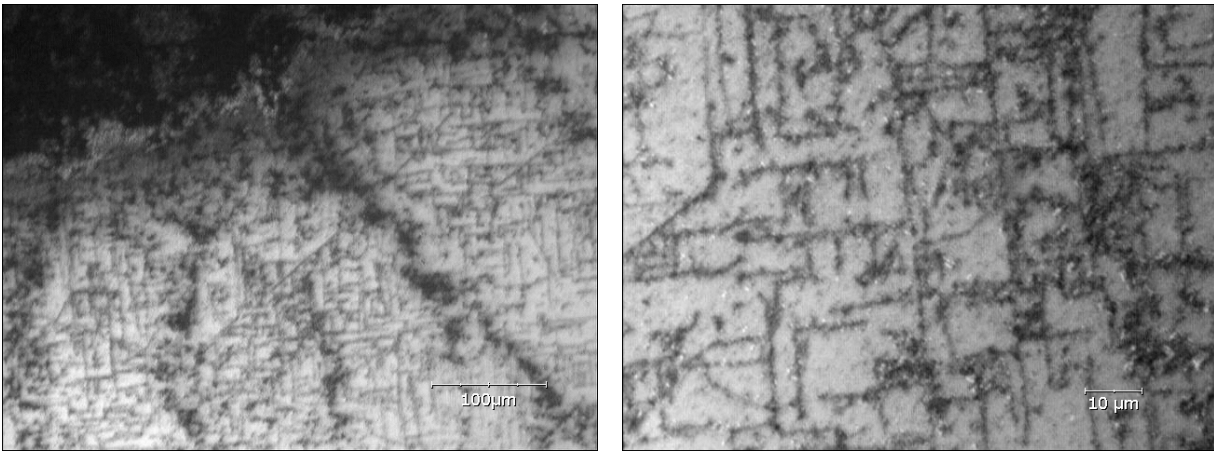


Figure 8.48 Optical microscope view of silicon surface after several seconds of spark processing. Discharge voltage 5 kV, discharge gap — 2 mm.

5. Conclusion

Coming to the conclusion of this chapter, it should be mentioned that μ EDM (and EDM itself) is the earliest non-conventional machining technique, which remains in constant development process. Resuming particularly our work, we can claim that the stochastic nature of spark occurrence can be well controlled, which allows reproducing of features as small as several microns on the surface of conductive material. There is no any objective reason for not to make these features even smaller. For the resolution achieved, there are many applications which need machining of metallic (stainless steel) or semiconducting materials (silicon), for example in microfluidics (micropumps, chemical micro-reactors, etc.), MEMS (micromotors, microgears, actuators, etc.), molds for polymer injection of microparts, etc. If (as expected but not demonstrated in this work), the resolution can be improved to 100—300 nm features with an optimization of the fabrication of the electrodes, this will open completely new applications for EDM in micro and nanotechnology to machine stainless steel, pure metals like gold, silver, chromium (chromium-glass photomasks), doped and undoped silicon (e.g. silicon masters for nanoimprinting or microcontact printing), photonic crystals, etc.

Spark processing can also produce porous silicon in a safe way (no strong chemicals involved). In fact it is possible to produce layers of porous silicon using the same setup as for silicon micromachining in a single cycle. This process will require further research to determine the morphology of the porous silicon, the photoluminescence and the material stability according to the process parameters.

Single electrode electrical discharge machining can be combined as well with more accurate techniques like electrochemical machining (ECM), and specially ECM with ultrashort pulses [206]. It is foreseen that EDM/ECM processes could be combined to AFM

or STM techniques to improve the resolution. These facts give some great perspectives to the μ EDM technique and its implementation in silicon machining, spark processing and chemical etching.

Conclusions and perspectives

Summarizing the work presented, we can claim the porous silicon is indeed a unique material suitable for sensor devices fabrication. However, this material possesses some negative properties such as chemical (degradation due to the oxidation even on open air) and optical instability (degradation of optical properties), and requirements of strong chemicals for silicon etching. In our work we tried to leave out somehow these drawbacks proposing some modifications to the existing methods and introducing the new ones.

Different modifications of the photoluminescence of porous silicon measurement technique were proposed, concerning the intensity and decay time measurement for sensor applications. The proposed techniques were used in our further research on the influence of pH level of adsorbed substances on the photoluminescence properties of porous silicon. As a result we have found that the photoluminescence of porous silicon is sensitive to the pH level, which can be explained by the processes of UV-induced hydrogen effusion and restoration from the aqueous solution. To prevent the porous silicon oxidation we have implemented a PEDOT polymer coating that resulted in a relative increase of porous layer stability. To conclude, a porous silicon layer can be used as an optical pH-sensitive transducer, but we are not beyond proof of concept because of the material instability.

Moreover to increase the sensitivity of porous silicon based transducers, catalytic metals incorporation inside the pores was proposed. We have considered the deposition of Pt, Ag, and Ni inside the pores during the stain etching of porous silicon. We have measured the profile of deposited metals inside the porous silicon layers and studied electrical properties and photoluminescence of several samples. Thus, we have found that samples with Ag and Pt deposited do not manifest photoluminescence, whereas porous Si with Ni still retains its luminescence properties but lose them quickly due to the photooxidation process.

The electrical properties of porous silicon were studied to detect the absorbance of different gases. We studied the behavior of localized states in Pd-porous Si-Si heterojunctions by DLTS technique and showed the influence of adsorbed gases on these states. The conductivity measurements of porous silicon / silicon structures were also proposed to be carried out in contact-less mode using eddy current method of detection. Unfortunately, we were not able to achieve a high sensitivity in conductivity changes detection (for the adsorption of NO₂ gas) using these contact-less measurements.

The question of light-assisted porous silicon etching in HF based solution was considered in order to produce localized regions of porous silicon on silicon surface without applying photolithographic resin. We have studied n-doped and p-doped silicon anodization process with direct light patterning that allows localizing porous spots with a resolution of approximately 100 μm (that is limited by minor carriers diffusion length in Si crystal). It was also shown that porous silicon profile can be controlled by applying the superficial electric field that proves the idea of the minor carriers leading role in light-assisted porous silicon etching. We believe that this work may be of practical high interest for production of low density biochip (e.g. DNA or protein chips for personalized medicine [207]).

The last part of our work was related to the electrical discharge machining (EDM) of silicon and the development of micro-EDM technique, which should take place besides the classical photolithographic process in silicon machining. As a result of this research, we have established the μEDM technique and managed to achieve resolution of machined features of several micrometers using (i) Pt-Ir microtips as working electrodes, (ii) high speed electronics based on IGBT transistors to create the electrical discharge and (ii) optimized algorithms for the discharge control. The developed method has some interesting perspectives for silicon machining by spark processing. This includes the local formation of porous silicon on silicon wafer by electro-erosion without involving any chemicals. Although, we had not the time to fully explore the potential of this technology, the instrument that we have developed will be used later in the laboratory to carry on this research. It will be interesting for example to find with this instrument, the parameters leading to photoluminescent porous silicon, as already performed by Hummel and coworkers, and very important to check if this leads to a more stable material. In that case, it will be possible to improve the sensors described in the first chapters of this report. Moreover our experimental set up has key advantages compared to Hummel's work in term of speed of fabrication, possibility to define locally porous silicon and to vary the parameter along the substrate.

At the resolution demonstrated in this work, μEDM in itself is a technique of very high interest in the field of MEMS, microfluidics, fabrication of micromolds for polymer

injection, etc. This process goes far beyond the world of silicon, since it can micro-machine all metallic and semiconducting materials, even the most difficult ones (e.g. SiC, titanium). Our experimental set up is surprisingly (to our eyes) simple, low cost, flexible and easy to use. Therefore we believe that this sequential technology should not be underestimated in the field of microtechnology, which is dominated by the collective fabrication concept. Also its ultimate limit in terms of resolution is still an opened question. Specially, to reach submicrometric resolution would be a breakthrough which may open new fields of application in micro and nanotechnology (e.g. optics, microphotonics). This will be related notably to our capacity to prepare ultrathin electrodes (e.g. \varnothing 100 nm) and to monitor ultrafast electrical discharge. The limit will come from the physics underlying the process, which have to be re-investigated at this scale.

Conclusion et perspectives

Pour résumer ce travail, on peut tout d'abord souligner le fait que le silicium poreux est un matériau très intéressant pour la fabrication de microdispositifs comportant des capteurs. Toutefois, ce matériau présente des inconvénients car il est sujet à une dégradation chimique (causée par une oxydation y compris à l'air libre), et une instabilité optique (dégradation des propriétés optiques). Il nécessite aussi l'utilisation de produits très réactifs pour la gravure du silicium. Au cours de ce travail, nous avons tenté de limiter ces inconvénients en proposant des modifications aux méthodes existantes ou en introduisant de nouvelles.

Nous avons proposé différentes modifications des techniques de mesure de photoluminescence du silicium poreux, concernant les mesures d'intensité et de durée de vie, pour des applications liées aux capteurs. Les méthodes ont été mises en œuvre par la suite dans notre travail concernant l'influence des niveaux de pH de substances adsorbées sur les propriétés de photoluminescence du silicium poreux. Le résultat trouvé a été que la photoluminescence du silicium poreux est sensible au niveau du PH, ce qui peut être expliqué par l'effusion de l'hydrogène induite par UV et sa restauration par la solution aqueuse. Pour empêcher l'oxydation du silicium poreux, nous avons déposé une couche de polymère PEDOT, ce qui améliore dans une certaine mesure la stabilité de la couche poreuse. Pour conclure, une couche de silicium poreux peut être utilisée comme capteur optique sensible au PH, mais nous n'avons pas pu aller au-delà de la preuve de concept à cause de l'instabilité résiduelle du matériau.

Par ailleurs pour accroître la sensibilité de capteurs en silicium poreux, une méthode d'incorporation de métaux catalytiques à l'intérieur des pores a été proposée. Nous avons étudié la déposition de Pt, Ag, et Ni durant la fabrication du silicium poreux par dissolution chimique. Nous avons mesuré les profils des métaux déposés dans une couche de silicium

poreux et étudié les propriétés électriques et de photoluminescence de certains échantillons. Nous avons trouvé que le silicium poreux avec du Pt ou Ag incorporé ne manifeste pas de la photoluminescence tandis que le Si poreux avec Ni garde sa photoluminescence, celle-ci pourtant est vite dégradée à cause de la photo-oxidation.

Puis nous avons étudié les propriétés électriques du silicium poreux pour détecter l'adsorption de différents gaz. Premièrement, nous avons étudié le comportement en spectroscopie dynamique des niveaux localisés des hétérojonctions Pd-Si poreux-Si par la technique DLTS et avons montré l'influence des gaz adsorbés sur ces niveaux. Puis des mesures de conductivité de structures silicium et silicium poreux ont été proposés de façon à pouvoir mettre en œuvre une méthode de détection sans contact basée sur des courants de Foucault. Malheureusement nous n'avons pas pu atteindre une grande sensibilité dans la détection des changements de conductivité entraînés par l'adsorption de NO₂.

La question de la gravure du silicium poreux dans du HF assistée par la lumière a aussi été traitée pour produire des zones localisées de silicium poreux sur des surfaces de silicium, sans faire appel à un procédé avec une résine photolithographique. Nous avons étudié un procédé d'anodisation de silicium dopé n et dopé p avec un transfert de motifs directement effectué avec de la lumière, ce qui permet de créer localement des plots poreux avec une résolution d'environ 100 μm (limitée par la longueur de diffusion des porteurs minoritaires dans le cristal de Si). Il a été montré aussi que le profil du silicium poreux peut être contrôlé en appliquant un champ électrique superficiel, ce qui est une preuve du rôle joué par les porteurs de charge minoritaires dans la gravure du silicium poreux assistée par la lumière. Nous pensons que ce travail est d'un grand intérêt pratique dans la production de masse de biopuces basse densité (par exemple de puces à ADN ou à protéines pour la médecine personnalisée [207]).

La dernière partie de notre travail concerne l'usinage du silicium par des décharges électriques (EDM) et le développement d'une technique de microélectroérosion, qui pourrait être complémentaire des procédés classiques de photolithographie pour l'usinage du silicium. Nos résultats ont été les suivants : nous avons mis en place un procédé de microélectroérosion et réussi à atteindre une résolution d'usinage de quelques micromètres avec (i) des micropointes Pt-Ir comme électrode de travail, (ii) une électronique rapide basée sur des transistors IGBT pour la création des décharges et (iii) des algorithmes optimisés de contrôle de décharge en fonction de l'enfoncement de l'électrode. La méthode développée conduit à d'intéressantes perspectives pour l'usinage du silicium par décharges électriques. Cela inclut la formation localisée de silicium poreux sur des wafers silicium par électro-érosion sans aucun produit chimique. Bien que nous n'ayons pas eu le temps d'explorer le potentiel de

cette technologie, l'instrument que nous avons développé sera utilisé ultérieurement dans le laboratoire pour continuer cette recherche. Il sera intéressant par exemple de trouver les paramètres menant à du silicium poreux photoluminescent, comme cela a déjà été fait par Hummel et son équipe, et ce qui est très important de vérifier si cela conduit à un matériau plus stable. Dans ce cas il sera possible d'améliorer les capteurs décrits dans les premiers chapitres de ce mémoire. De plus, notre dispositif expérimental présente des avantages déterminants, par rapport au travail de Hummel, en terme de vitesse de fabrication, possibilité de définir localement le silicium poreux et de faire varier les paramètres sur la surface du substrat.

A la résolution démontrée dans le cadre de ce travail, la microélectroérosion est en soi une technique d'un très grand intérêt dans le champ des MEMS, de la microfluidique, de la fabrication de micromoules pour l'injection de polymère, etc. Ce procédé s'applique bien au-delà du monde du silicium, puisqu'il permet de micro-usiner tous les métaux et semiconducteurs, y compris les plus difficiles (SiC, Titane,...). Notre dispositif expérimental est, de manière surprenante (du moins à nos yeux), simple, de faible coût, flexible et facile à mettre en œuvre. C'est pourquoi, nous pensons que cette technologie séquentielle ne doit pas être sous-estimée dans le champ de la microtechnologie, qui est dominée par le concept de fabrication collective. De plus, sa limite ultime en terme de résolution est encore une question ouverte. Soulignons qu'atteindre une résolution submicrométrique serait un bond en avant, qui ouvrirait de nouveaux champs d'applications en micro et nanotechnologie (optique, microphotonique, etc.). Cela dépendra notamment de notre capacité à préparer des électrodes ultrafines (par exemple \varnothing 100 nm) et à contrôler des décharges électriques ultrarapides. La limite viendra de la physique du procédé qu'il faudra ré-étudier à cette échelle.

Annex 1

μ EDM Electronics Schematic

In this annex, the schematic of μ EDM setup electronics is presented. It is not a well optimized and final design, however, this electronic implementation was used in our μ EDM setup used for the experiments described in the last chapter of the thesis. The whole schematic consists of two parts: digital part with MCU and interface with a host PC, and analog part with power switches and work tool / workpiece connections. The MCU's firmware, which is required for electronics to operate, is not presented in this annex.

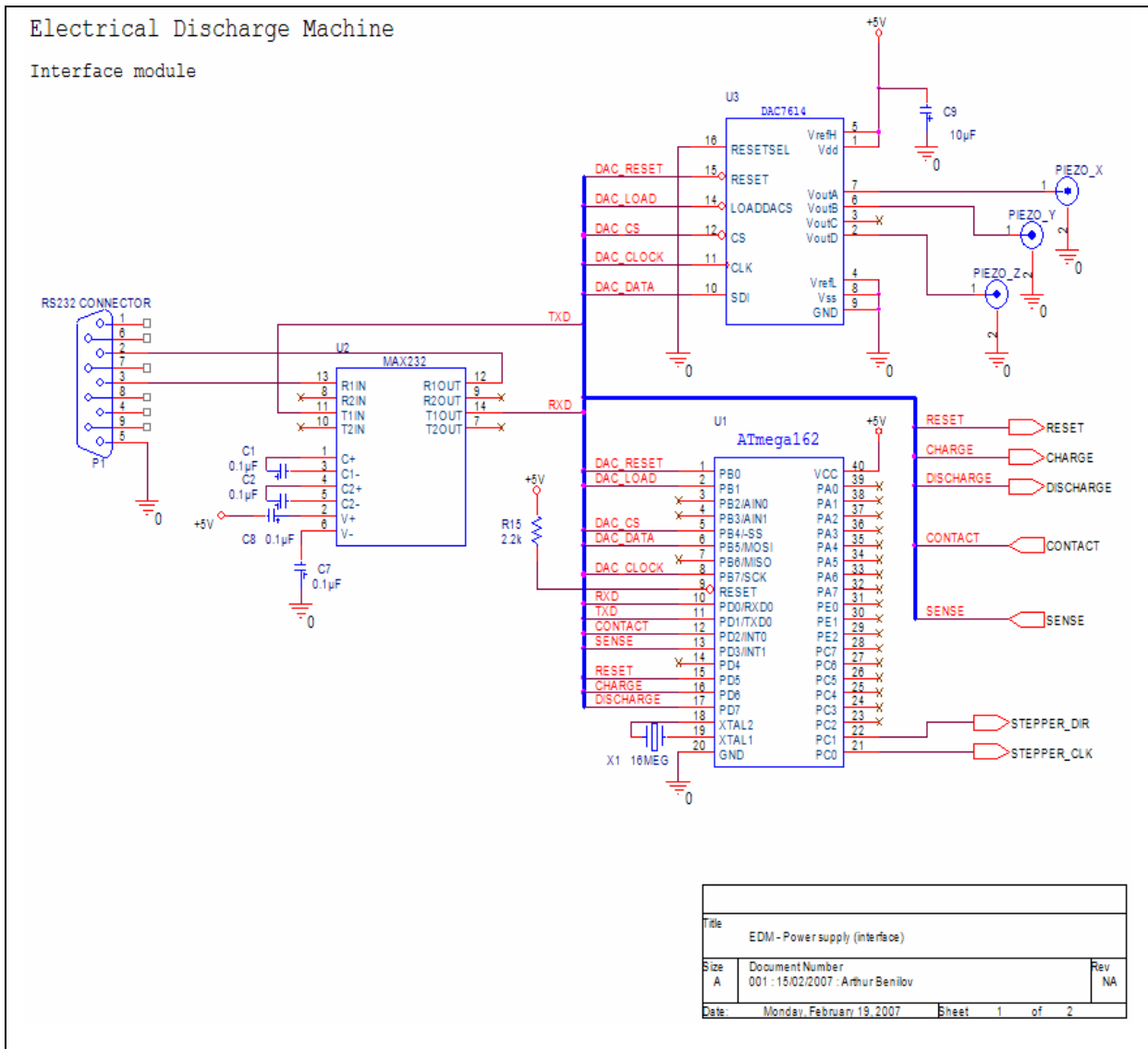


Figure 1 μ EDM circuit schematic. MCU and interface part.

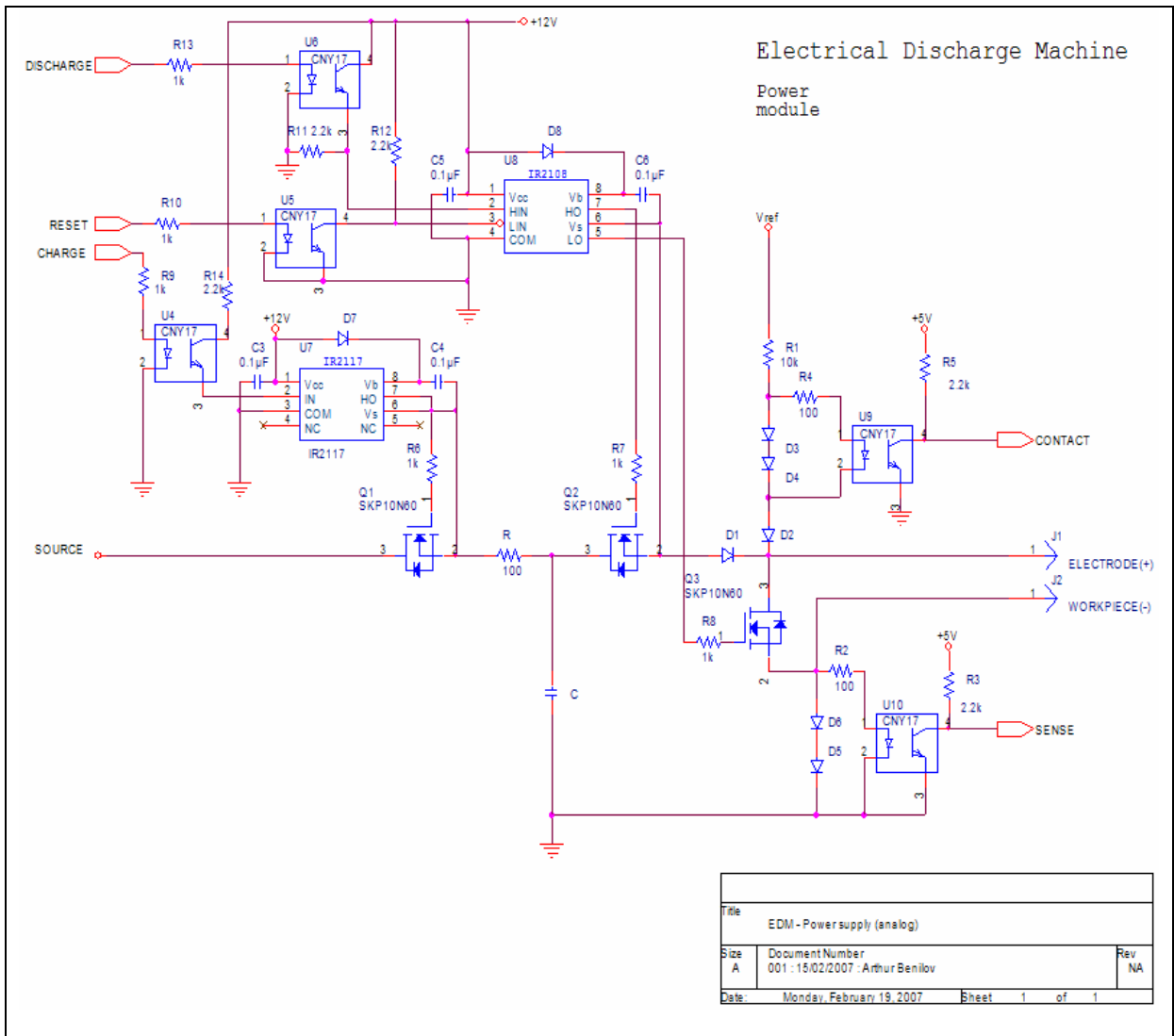


Figure 2 μ EDM circuit schematic. Analog part.

Annex 2

μEDM Scripting Language

The μEDM scripting language was specially developed for easy description of part geometry and machining with the μEDM setup. In this annex a general syntax of this language is defined. Some examples of its usage can be found in the last chapter of this thesis. It should be mentioned that the μEDM scripting language described in this manuscript was tuned to be used mainly in our research work and does not intend to be a valuable programming and design language for EDM setups controlling. However, even in its present, form the scripting language allows describing of rather complex machining structures and moreover it can be easily developed to implement any other control structures and directives required.

The syntax of μEDM scripting language consists of reserved (key-) words which can be combined into control operators, and identifiers that can be defined by designer to facilitate the script and design-related calculations. Each design script is framed in the following construction:

```
DESIGN <ScriptName> IS  
    ...  
END.
```

<ScriptName> is identifier that defines a name for this particular script. The design definition itself is going between ‘DESIGN’ and ‘END’ keywords. All identifiers are represented by a set of characters that can be combined with numbers and ‘_’ symbol.

Designer can define macro-values inside the script. To define a macro-value a simple construction is used:

```
<Identifier> = <value>;
```

Where <Identifier> defines a macro's name, and the <value> its corresponding value. The value can be represented by floating point numbers or by expression, that can include numbers, previously defines macros, basic mathematical operations ('+', '-', '*', '/', and brackets), and functions (such as `sin()`, `sqrt()`, etc.).

Other important part of μ EDM scripting language is the operators to control the EDM setup. Some of these operators take several parameters that can be defined as numbers or macros identifiers. The following table represents the list of such operators with description of each of them.

Operator	Description
TOUCH;	Move electrode towards the workpiece surface and stop on contact.
RELEASE [<n>;]	Move electrode <n> steps up. The parameter <n> can be omitted; in this case the default value is 64 steps of Z-positioning system.
CHARGE <time>;	Setting up the charge time. The <time> value is defined in microseconds.
DISCHARGE <time>;	Setting up the discharge time in microseconds.
MOVE TO <x>, <y>;	Displace the positioning system by <x> steps along the X-axis, and by <y> steps along the Y-axis. For this displacement a stepper motors driven table is used. The displacement is accomplished at speed of 1000 steps per second (2.5 mm/s)
TABLE TO <x>, <y>;	Displace the piezo-driven table by <x> and <y> values along the corresponding directions. The values of <x> and <y> are defined in nanometers.
START;	Starting the pulse generator. The voltage pulses are supplied to the work electrode after execution of this command.
STOP;	Shutting down the pulse generator.
LINE TO <x>, <y> SPEED s;	Move by <x>, <y> steps at the speed of <s> steps per second. Stepper motors driven table is used.
WAIT <t>;	Suspend all activity waiting <t> seconds.

HOLE <s>;	'Drilling' inside the workpiece during <s> seconds.
SPARK ;	Make a single spark using gradual electrode approach mode.
PRINT <expression>;	Output <expression> value to the logging window. This instruction is useful mainly for script debugging.
REPEAT <n> IS ... END ;	Repeat whatever is between 'REPEAT <n> IS' and 'END' statements <n> times. Very useful for one-type features machining.

All scripts are stored in '*.edm' files that can be loaded and executed by the EDM control software.

Bibliography

1. Uhlir, A., *Electrolytic Shaping of Germanium and Silicon*. Bell Syst. Tech. J., 1956. **35**: p. 333-347.
2. Arthur Uhlir, J. and I.W. Uhlir, *Historical perspective on the discovery of porous silicon*. phys. stat. sol. (c), 2005. **2**(9): p. 3185-3187.
3. *Properties of Porous Silicon*, ed. L.T. Canham. 1997, London, UK: INSPEC, The Institution of Electrical Engineers.
4. Buda, F., J. Kohanoff, and M. Parrinello, *Optical Properties of Porous Silicon: A First-Principles Study*. Physical Review Letters, 1992. **69**(8): p. 1272-1275.
5. Kux, A. and M. Ben Chorin, *Band gap of porous silicon*. Physical Review B, 1995. **51**(24): p. 17535-17541.
6. Fiory, A.T. and N.M. Ravindra, *Light Emission from Silicon: Some Perspectives and Applications*. Journal of Electronic Materials, 2003. **32**(10): p. 1043-1051.
7. Novikov, P.L., L.N. Aleksandrov, A.V. Dvurechenskii, and V.A. Zinov'ev, *Mechanism of silicon epitaxy on porous silicon layers*. JETP Letters, 1998. **67**(7): p. 539-544.
8. Canham, L.T., *Silicon quantum wire array fabrication by electrochemical and chemical dissolution of wafers*. Appl. Phys. Lett., 1990. **57**(10): p. 1046-1048.
9. Bisi, O., S. Ossicini, and L. Pavesi, *Porous silicon: a quantum sponge structure for silicon based optoelectronics*. Surface Science Reports, 2000. **38**: p. 1-126.
10. Canham, L.T., M.R. Houlton, W.Y. Leong, C. Pickering, and J.M. Keen, *Atmospheric impregnation of porous silicon at room temperature*. J. Appl. Phys., 1991. **70**(1): p. 422-431.
11. Dimova-Malinovska, D., M. Sendova-Vassileva, N. Tzenov, and M. Kamenova, *Preparation of thin porous silicon layers by stain etching*. Thin Solid Films, 1997. **297**: p. 9-12.
12. Hummel, R.E. and S.-S. Chang, *Novel technique for preparing porous silicon*. Appl. Phys. Lett., 1992. **61**(16): p. 1965-1967.
13. Lihao, R. and A. Pavlov, *Preparation of porous silicon films by laser ablation*. Thin Solid Films, 1995. **255**: p. 9-11.
14. Beale, M.I.J., N.G. Chew, M.J. Uren, A.G. Cullis, and J.D. Benjamin, *Microstructure and formation mechanism of porous silicon*. Appl. Phys. Lett., 1985. **46**(1): p. 86-88.
15. Smith, R.L. and S.D. Collins, *Porous silicon formation mechanisms*. Journal of Applied Physics, 1992. **71**(8): p. R1-22.

16. Chazalviel, J.-N., R.B. Wehrspohn, and F. Ozanam, *Electrochemical preparation of porous semiconductors: from phenomenology to understanding*. Materials Science and Engineering B, 2000. **69-70**: p. 1-10.
17. Cullis, A.G., L.T. Canham, and P.D.J. Calcott, *The structural and luminescence properties of porous silicon*. Journal of Applied Physics, 1997. **82**(3): p. 909-965.
18. Arrand, H.F., *Optical waveguides and components based on porous silicon*. 1997, University of Nottingham: Nottingham.
19. Tao, Y. and M. Esashi, *Macroporous silicon-based deep anisotropic etching*. J. Micromech. Microeng., 2005. **15**: p. 764-770.
20. Müller, F., A. Birner, U.M. Gösele, V. Lehmann, S. Ottow, and H. Föll, *Structuring of Macroporous Silicon for Applications as Photonic Crystals*. Journal of Porous Materials, 2000. **7**: p. 201-204.
21. Lehmann, V. and U. Gösele, *Porous silicon formation: A quantum wire effect*. Appl. Phys. Lett., 1991. **58**(8): p. 856-858.
22. Erlebacher, J., K. Sieradzki, and P.C. Searson, *Computer simulations of pore growth in silicon*. Journal of Applied Physics, 1994. **76**(1): p. 182-187.
23. Lehmann, V., *The physics of macroporous silicon formation*. Thin Solid Films, 1999. **255**: p. 1-4.
24. Скришевський, В.А., *Фізичні основи напівпровідникових хімічних сенсорів*. 2006, Київ: ВПЦ "Київський університет".
25. Hamilton, B., *Porous silicon*. Semicond. Sci. Technol., 1995. **10**: p. 1187-1207.
26. Föll, H., J. Carstensen, M. Christophersen, and G. Hasse, *A New View of Silicon Electrochemistry*. phys. stat. sol. (a), 2000. **182**: p. 7-16.
27. Ronkel, F. and J.W. Schultze, *Electrochemical Aspects of Porous Silicon Formation*. Journal of Porous Materials, 2000. **7**: p. 11-16.
28. Koker, L., A. Wellner, P.A.J. Sherratt, R. Neuendorf, and K.W. Kolasinski, *Etchant composition effects on porous silicon morphology and photoluminescence*. phys. stat. sol. (a), 2003. **197**(1): p. 117-122.
29. Koker, L. and K.W. Kolasinski, *Photoelectrochemical etching of Si and porous Si in aqueous HF*. Phys. Chem. Chem. Phys., 2000. **2**: p. 277-281.
30. Tanino, H., A. Kuprin, H. Deai, and N. Koshida, *Raman study of free-standing porous silicon*. Physical Review B, 1996. **53**(4): p. 1937-1947.
31. Cojocar, I., V. Pasat, V. Karavanskii, and V. Chumash, *Optical Hysteresis in Free-standing Porous Silicon Films*. Journal of Optoelectronics and Advanced Materials, 2001. **3**(1): p. 133-135.
32. Charrier, J., C. Lupi, L. Haji, and C. Boisrobert, *Optical study of porous silicon buried waveguides fabricated from p-type silicon*. Materials Science in Semiconductor Processing, 2000. **3**: p. 357-361.
33. Charrier, J., E.L. Gorju, L. Haji, and M. Guendouz, *Optical Waveguides Fabricated from Oxidised Porous Silicon*. Journal of Porous Materials, 2000. **7**: p. 243-246.
34. Liu, S., C. Palsule, S. Yi, and S. Gangopadhyay, *Characterization of stain-etched porous silicon*. Physical Review B, 1994. **49**(15): p. 10318-10325.
35. Starostina, E.A., V.V. Starkov, and A.F. Vyatkin, *Porous-Silicon Formation in HF-HNO₃-H₂O Etchants*. Russian Microelectronics, 2002. **31**(2): p. 88-96.
36. Vázsonyi, É., E. Szilágyi, P. Petrik, Z.E. Horváth, T. Lohner, M. Fried, and G. Jalsovszky, *Porous silicon formation by stain etching*. Thin Solid Films, 2001. **388**: p. 295-302.
37. Hummel, R.E., A. Morrone, M. Ludwig, and S.-S. Chang, *On the origin of photoluminescence in spark-eroded (porous) silicon*. Appl. Phys. Lett., 1993. **63**(20): p. 2771-2773.

38. Song, X., D. Reynaerts, W. Meeusen, and H. Van Brussel, *A study on the elimination of micro-cracks in a sparked silicon surface*. Sensors and Actuators A, 2001. **92**: p. 286-291.
39. Tao, Y. and M. Esashi, *Local formation of macroporous silicon through a mask*. J. Micromech. Microeng., 2004. **14**: p. 1411-1415.
40. Starkov, V.V., E.Y. Gavrilin, J. Konle, H. Presting, A.F. Vyatkin, and U. König, *SU8 photoresist as an etch mask for local deep anodic etching of silicon*. phys. stat. sol. (a), 2003. **197**(1): p. 150-157.
41. Rossi, A.M., S. Borini, L. Boarino, and G. Amato, *Lateral structuring of porous silicon: application to waveguides*. phys. stat. sol. (a), 2003. **197**(1): p. 284-287.
42. Setzu, S., P. Ferrand, G. Léron del, and R. Romestain, *Photo-lithography for 2D optical microstructures in porous silicon: application to nucleation of macropores*. Applied Surface Science, 2002. **186**: p. 588-593.
43. Léron del, G., R. Romestain, J.C. Vial, and M. Thönissen, *Porous silicon lateral superlattices*. Appl. Phys. Lett., 1997. **71**(2): p. 196-198.
44. Pagonis, D., G. Kaltsas, and A.G. Nassiopoulou, *Implantation masking technology for selective porous silicon formation*. phys. stat. sol. (a), 2003. **197**(1): p. 241-245.
45. Noguchi, N. and I. Suemune, *High-Resolution Patterning of Luminescent Porous Silicon with Photoirradiation*. Jpn. J. Appl. Phys., 1994. **33**: p. 590-593.
46. Noguchi, N. and I. Suemune, *Selective formation of luminescent porous silicon by photosynthesis*. Journal of Applied Physics, 1994. **75**(9): p. 4765-4767.
47. Schmuki, P. and L.E. Erickson, *Selective high-resolution electrodeposition on semiconductor defect patterns*. Physical Review Letters, 2000. **85**(14): p. 2985-2988.
48. Fauchet, P.M., *Photoluminescence and electroluminescence from porous silicon*. Journal of Luminescence, 1996. **70**: p. 294-309.
49. Guerrero-Lemus, R., F.A. Ben-Hander, J.L.G. Fierro, C. Hernández-Rodríguez, and J.M. Martínez-Duart, *Compositional and photoluminescent properties of anodically and stain etched porous silicon*. phys. stat. sol. (a), 2003. **197**(1): p. 137-143.
50. Zhaoa, Y., D. Yanga, D. Lia, and M. Jianga, *Photoluminescence of oxidized porous silicon under UV-light illumination*. Materials Science and Engineering B, 2005. **116**: p. 95-98.
51. Tsybeskov, L., J.V. Vandyshev, and P.M. Fauchet, *Blue emission in porous silicon: Oxygen-related photoluminescence*. Physical Review B, 1994. **49**(11): p. 7821-7824.
52. Joshkin, V.A., M.N. Naidenkov, V.N. Pavlenko, A.V. Kvit, and S.R. Oktyabrsky, *Evidence for quantum confinement in porous silicon from photoluminescence measurements*. Physical Review B, 1995. **52**(16): p. 12102-12107.
53. Caldas, M.J., *Si Nanoparticles as a Model for Porous Si*. phys. stat. sol. (a), 2000. **217**: p. 641-663.
54. Saunders, W.A., P.C. Cersel, R.B. Lee, H.A. Atwater, K.J. Vahala, R.C. Flagan, and E.J. Escorcia-Aparcio, *Synthesis of luminescent silicon clusters by spark ablation*. Appl. Phys. Lett., 1993. **63**(11): p. 1549-1551.
55. Shepherd, N. and R.E. Hummel, *Improved electroluminescence of spark-processed silicon by an aerosol-assisted technique*. phys. stat. sol. (a), 2003. **197**(1): p. 222-227.
56. Yuan, J. and D. Haneman, *Electroluminescence from spark-processed porous silicon*. Appl. Phys. Lett., 1995. **67**(22): p. 3328-3330.
57. Rüter, D., T. Kunze, and W. Bauhofer, *Blue light emission from silicon surfaces prepared by spark-erosion and related techniques*. Appl. Phys. Lett., 1994. **64**(22): p. 3006-3008.
58. Hummel, R.E., M. Ludwig, S.-S. Chang, and G. LaTorre, *Comparison of anodically etched porous silicon with spark-processed silicon*. Thin Solid Films, 1995. **255**: p. 219-223.

59. Ludwig, M.H., A. Augustin, and R.E. Hummel, *Colour-switching effect of photoluminescent silicon after spark-processing in oxygen*. Semicond. Sci. Technol., 1997. **12**: p. 981-986.
60. Hummel, R.E. and M.H. Ludwig, *Spark-processing - A novel technique to prepare light-emitting, nanocrystalline silicon*. Journal of Luminescence, 1996. **68**: p. 69-76.
61. Vincent, G., *Optical properties of porous silicon superlattice*. Appl. Phys. Lett., 1994. **64**(18): p. 2367-2369.
62. Birner, A., R.B. Wehrspohn, U.M. Gösele, and K. Busch, *Silicon-Based Photonic Crystals*. Advanced Materials, 2001. **13**(6): p. 377-388.
63. Benson, T.M., H.F. Arrand, P. Sewell, D. Niemeyer, A. Loni, R.J. Bozeat, M. Krüger, R. Arens-Fischer, M. Thönissen, and H. Lüth, *Progress towards achieving integrated circuit functionality using porous silicon optoelectronic components*. Materials Science and Engineering B, 1999. **69-70**: p. 92-99.
64. Garrone, E., S. Borini, P. Rivolo, L. Boarino, F. Geobaldo, and G. Amato, *Porous Silicon in NO₂: A chemisorption mechanism for enhanced electrical conductivity*. phys. stat. sol. (a), 2003. **197**(1): p. 103-106.
65. Mihalcescu, I., J.C. Vial, and R. Romestain, *Absence of Carrier Hopping in Porous Silicon*. Physical Review Letters, 1998. **80**(15): p. 3392-3395.
66. Ben-Chorin, M., A. Kux, and I. Schechter, *Adsorbate effects on photoluminescence and electrical conductivity of porous silicon*. Appl. Phys. Lett., 1994. **64**(4): p. 481-483.
67. Pancheri, L., C.J. Oton, Z. Gaburro, G. Soncini, and L. Pavesi, *Very sensitive porous silicon NO₂ sensor*. Sensors and Actuators B, 2003. **89**: p. 237-239.
68. Massera, E., I. Nasti, L. Quercia, I. Rea, and G. Di Francia, *Improvement of stability and recovery time in porous-silicon-based NO₂ sensor*. Sensors and Actuators B, 2004. **102**: p. 195-197.
69. Pancheri, L., C.J. Oton, Z. Gaburro, G. Soncini, and L. Pavesi, *Improved reversibility in aged porous silicon NO₂ sensors*. Sensors and Actuators B, 2004. **97**: p. 45-48.
70. Angelucci, R., A. Poggi, L. Dori, A. Tagliani, G.C. Cardinali, F. Corticelli, and M. Marisaldi, *Permeated Porous Silicon Suspended Membrane as Sub-ppm Benzene Sensor for Air Quality Monitoring*. Journal of Porous Materials, 2000. **7**: p. 197-200.
71. Geobaldo, F., P. Rivolo, G.P. Salvador, G. Amato, L. Boarino, and E. Garrone, *Free carriers reactivation on p⁺-mesoporous silicon through ammonia adsorption: a FTIR study*. Sensors and Actuators B, 2004. **100**: p. 205-208.
72. Lehmann, V., R. Stengl, and A. Luigart, *On the morphology and the electrochemical formation mechanism of mesoporous silicon*. Materials Science and Engineering B, 2000. **69-70**: p. 11-22.
73. Fellah, S., F. Ozanam, N. Gabouze, and J.-N. Chazalviel, *Porous Silicon in Solvents: Constant-Lifetime PL Quenching and Confirmation of Dielectric Effects*. phys. stat. sol. (a), 2000. **182**: p. 367-372.
74. Kirkey, W.D., Y. Sahoo, X. Li, Y. He, M.T. Swihart, A.N. Cartwright, S. Bruckensteinc, and P.N. Prasad, *Quasi-reversible photoluminescence quenching of stable dispersions of silicon nanoparticles*. J. Mater. Chem., 2005. **15**: p. 2028-2034.
75. Chvojka, T., V. Vrkoslav, I. Jelinek, J. Jindrish, M. Lorenc, and J. Dian, *Mechanisms of photoluminescence sensor response of porous silicon for organic species in gas and liquid phases*. Sensors and Actuators B, 2004. **100**: p. 246-249.
76. Di Francia, G., M. Della Noce, V. La Ferrara, L. Lancellotti, P. Morvillo, and L. Quercia, *Nanostructured porous silicon for gas sensor applications*. Materials Science and Technology, 2002. **18**: p. 767-771.
77. Lauerhaas, J.M., G.M. Credo, J.L. Heinrich, and M.J. Sailor, *Reversible luminescence quenching of porous Si by solvents*. J. Am. Chem. Soc., 1992. **114**: p. 1911-1912.

78. Content, S., W.C. Trogler, and M.J. Sailor, *Detection of Nitrobenzene, DNT, and TNT Vapors by Quenching of Porous Silicon Photoluminescence*. Chem. Eur. J., 2000. **6**(12).
79. Balagurov, L.A., B.M. Leiferov, E.A. Petrova, A.F. Orlov, and E.M. Panasenko, *Influence of water and alcohols on photoluminescence of porous silicon*. Journal of Applied Physics, 1996. **79**(9): p. 7143-7147.
80. Stewart, M.P. and J.M. Buriak, *Chemical and Biological Applications of Porous Silicon Technology*. Advanced Materials, 2000. **12**(12): p. 859-869.
81. Tischler, M.A., R.T. Collins, J.H. Stathis, and J.C. Tsang, *Luminescence degradation in porous silicon*. Appl. Phys. Lett., 1992. **60**(5): p. 639-641.
82. Elhouichet, H., M. Oueslati, B. Bessaïs, E. Ezzaouia, and B.Y. O., *Laser Induced Degradation of Photoluminescence Intensity of Porous Silicon*. Journal of Porous Materials, 1999. **7**: p. 307-310.
83. Koropecski, R.R., R.D. Arce, and J.A. Schmidt, *Photo-oxidation effects in porous silicon luminescence*. Physical Review B, 2004. **69**: p. 205317.
84. Lin, V.S.-Y., K. Motesharei, K.-P.S. Dancil, M.J. Sailor, and M. Reza Ghadiri, *A Porous Silicon-Based Optical Interferometric Biosensor*. Science, 1997. **278**: p. 840-843.
85. Steinem, C., A. Janshoff, V.S.-Y. Lin, N.H. Völcker, and M.R. Ghadiri, *DNA hybridization-enhanced porous silicon corrosion: mechanistic investigations and prospect for optical interferometric biosensing*. Tetrahedron, 2004. **60**: p. 11259-11267.
86. De Stefano, L., L. Rotiroti, I. Rendina, L. Moretti, V. Scognamiglio, M. Rossi, and S. D'Auria, *Porous silicon-based optical microsensor for the detection of l-glutamine*. Biosensors and Bioelectronics, 2006. **21**: p. 1664-1667.
87. Zangoie, S., R. Bjorklund, and H. Arwin, *Vapor sensitivity of thin porous silicon layers*. Sensors and Actuators B, 1997. **43**: p. 168-174.
88. Gao, J., T. Gao, and M.J. Sailor, *Porous-silicon vapor sensor based on laser interferometry*. Appl. Phys. Lett., 2000. **77**(6): p. 901-903.
89. Liu, R., T.A. Schmedake, Y.Y. Li, M.J. Sailor, and Y. Fainman, *Novel porous silicon vapor sensor based on polarization interferometry*. Sensors and Actuators B, 2002. **87**: p. 58-62.
90. Min, H.-K., H.-S. Yang, and S.M. Cho, *Extremely sensitive optical sensing of ethanol using porous silicon*. Sensors and Actuators B, 2000. **67**: p. 199-202.
91. Mulloni, V., Z. Gaburro, and L. Pavesi, *Porous Silicon Microcavities as Optical and Electrical Chemical Sensors*. phys. stat. sol. (a), 2000. **182**: p. 479-484.
92. Chan, S., Y. Li, L.J. Rothberg, B.L. Miller, and P.M. Fauchet, *Nanoscale silicon microcavities for biosensing*. Materials Science and Engineering C, 2001. **15**: p. 277-282.
93. Martín-Palma, R.J., V. Torres-Costa, M. Arroyo-Hernández, M. Manso, J. Pérez-Rigueiro, and J.M. Martínez-Duart, *Porous silicon multilayer stacks for optical biosensing applications*. Microelectronics Journal, 2004. **35**: p. 45-48.
94. De Stefano, L., I. Rendina, L. Moretti, and A.M. Rossi, *Optical sensing of flammable substances using porous silicon microcavities*. Materials Science and Engineering B, 2003. **100**: p. 271-274.
95. Meskini, O., A. Abdelghani, A. Tlili, R. Mgaïeth, N. Jaffrezic-Renault, and C. Martelet, *Porous silicon as functionalized material for immunosensor application*. Talanta, 2007. **71**: p. 1430-1433.
96. Ravi Kumar Reddy, R., I. Basu, E. Bhattacharya, and A. Chadha, *Estimation of triglycerides by a porous silicon based potentiometric biosensor*. Current Applied Physics, 2003. **3**: p. 155-161.

97. Thust, M., M.J. Schöning, S. Frohnhoff, R. Arens-Fischer, P. Kordos, and H. Lüth, *Porous silicon as a substrate material for potentiometric biosensors*. Meas. Sci. Technol., 1996. **7**: p. 26-29.
98. Lüth, H., M. Thust, A. Steffen, P. Kordos, and M.J. Schöning, *Biochemical sensors with structured and porous silicon capacitors*. Materials Science and Engineering B, 2000. **69-70**: p. 104-108.
99. Schöning, M.J., F. Ronkel, M. Crott, M. Thust, J.W. Schultze, P. Kordos, and H. Lüth, *Miniaturization of potentiometric sensors using porous silicon microtechnology*. Electrochimica Acta, 1997. **42**(20-22): p. 3185-3193.
100. Zairi, S., C. Martelet, N. Jaffrezic-Renault, R. Lamartine, R. M'gaieth, H. Maaref, M. Gamoudi, and G. Guillaud, *Porous silicon as a potentiometric transducer for ion detection: effect of the porosity on the sensor response*. Applied Surface Science, 2001. **172**: p. 225-234.
101. Song, M.-J., D.-H. Yun, J.-H. Jin, N.-K. Min, and S.-I. Hong, *Comparison of Effective Working Electrode Areas on Planar and Porous Silicon Substrates for Cholesterol Biosensor*. Jpn. J. Appl. Phys., 2006. **45**(9A): p. 7197-7202.
102. Björkqvist, M., J. Salonen, E. Laine, and L. Niinistö, *Comparison of stabilizing treatments on porous silicon for sensor applications*. phys. stat. sol. (a), 2003. **197**(2): p. 374-377.
103. Gavrilov, S.A., A.I. Belogorokhov, and L.I. Belogorokhova, *A Mechanism of Oxygen-Induced Passivation of Porous Silicon in the HF: HCl : C₂H₅OH Solutions*. Semiconductors, 2002. **36**(1): p. 98-101.
104. Benilov, A.I. and V.A. Skryshevsky, *Improvement over the luminescence lifetime measurement technique*. Bulletin of the University of Kiev, Series: Physics & Mathematics, 2006. **4**: p. 269-278.
105. McQuarrie, D.A. and J.D. Simon, *Physical Chemistry, a molecular approach*. University Science Books. 1997.
106. Valeur, B., *Molecular Fluorescence - Principles and Applications*. 2002: WILEY-VCH.
107. O'Connor, D.V. and D. Phillips, *Time Correlated Single Photon Counting*. Academic Press. 1984, London.
108. Lukasiak, Z., P. Dalasinski, and W. Bala, *Kinetics of photoluminescence of porous silicon studied by photo-luminescence excitation spectroscopy and time-resolved spectroscopy*. Optoelectronics Review, 2003. **11**(2): p. 113-117.
109. *Photomultiplier tubes handbook*. Hamamatsu Photonics. 1994.
110. Zianni, X. and A.G. Nassiopoulou, *Multi-component behavior of the photoluminescence lifetime in porous Si*. phys. stat. sol. (a), 2003. **197**(2): p. 311-315.
111. Benilov, A.I., I.V. Gavrilchenko, I.V. Benilova, V.A. Skryshevsky, and M. Cabrera, *Influence of pH Solution on Photoluminescence of Porous Silicon*. Sensors and Actuators A, 2007. **doi: 10.1016/j.sna.2007.02.032**.
112. Hamm, D., T. Sakka, and Y.H. Ogata, *Etching of porous silicon in basic solution*. phys. stat. sol. (a), 2003. **197**(1): p. 175-179.
113. Ogata, Y.H., T. Tsuboi, T. Sakka, and S. Naito, *Oxidation of Porous Silicon in Dry and Wet Environments under Mild Temperature Conditions*. Journal of Porous Materials, 2000. **7**: p. 63-66.
114. Belogorokhov, A.I. and L.I. Belogorokhova, *Optical properties of porous silicon layers processed with HF:HCl:C₂H₅OH electrolyte*. Semiconductors, 1999. **33**(2): p. 169-174.
115. Hadj Zoubir, N., M. Vergnat, T. Delatour, A. Burneau, and P. de Donato, *Interpretation of the luminescence quenching in chemically etched porous silicon by the desorption of SiH₃ species*. Appl. Phys. Lett., 1994. **65**(1): p. 82-84.

116. Gole, J.L., J.A. DeVincentis, L. Seals, P.T. Lillehei, S.M. Prokes, and D.A. Dixon, *Chloride salt enhancement and stabilization of the photoluminescence from a porous silicon surface*. Physical Review B, 2000. **61**(8): p. 5615-5631.
117. Bakker, J.W.P., H. Arwin, G. Wang, and K. Järrendahl, *Improvement of porous silicon based gas sensors by polymer modification*. phys. stat. sol. (a), 2003. **197**(2): p. 378-381.
118. Zhao, Y., D. Li, and D. Yang, *Effect of post-treatment processes on the photoluminescence of porous silicon*. Physica B, 2005. **364**: p. 180-185.
119. Soldatkin, A.P., A.V. El'skaya, S.g.A. A., L.I. Netchiporuk, A.M. Nyamsy Hendji, N. Jaffrezic-Renault, and C. Martelet, *Glucose-sensitive field-effect transistor with additional Nafion membrane: Reduction of influence of buffer capacity on the sensor response and extension of its dynamic range*. Anal. Chem. Acta., 1993. **283**(2): p. 695-701.
120. Tolstoy, V.P., I.V. Chernyshova, and V.A. Skryshevsky, *Handbook of Infrared Spectroscopy of Ultrathin Films*. 2003: John Wiley & Sons, Inc.
121. Collins, R.T., M.A. Tischler, and J.H. Stathis, *Photoinduced hydrogen loss from porous silicon*. Appl. Phys. Lett., 1992. **61**(14): p. 1649-1651.
122. Schöning, M.J., A. Simonis, C. Ruge, H. Ecken, M. Müller-Veggian, and H. Lüth, *A (Bio-)Chemical Field-Effect Sensor with Macroporous Si as Substrate Material and a SiO₂ / LPCVD-Si₃N₄ Double Layer as pH Transducer*. Sensors, 2002. **2**: p. 11-22.
123. Chan, S., S. Kwon, T.-W. Koo, L.P. Lee, and A.A. Berlin, *Surface-Enhanced Raman Scattering of Small Molecules from Silver-Coated Silicon Nanopores*. Advanced Materials, 2003. **15**(19): p. 1595-1598.
124. Lin, J.-C., W.-C. Tsai, and W.-S. Lee, *The improved electrical contact between a metal and porous silicon by deposition using a supercritical fluid*. Nanotechnology, 2006. **17**: p. 2968-2971.
125. Peng, K., J. Hu, Y. Yan, Y. Wu, H. Fang, Y. Xu, S.T. Lee, and J. Zhu, *Fabrication of Single-Crystalline Silicon Nanowires by Scratching a Silicon Surface with Catalytic Metal Particles*. Adv. Funct. Mater., 2006. **16**: p. 387-394.
126. Verhaverbeke, S., H. Bender, M. Meuris, P.W. Mertens, H.P. Schmidt, and M.M. Heyns. in *MRS Symp. on Surface Chemical Cleaning and Passivation for Semiconductor Proc.* 1993. San Francisco, CA.
127. Kuznetsov, G.V., V.A. Skryshevsky, T.A. Vdovenkova, A.I. Tsyganova, P. Gorostiza, and F. Sanz, *Platinum electroless deposition on silicon from hydrogen fluoride solutions: electrical properties*. J. Electrochem. Soc., 2001. **148**: p. 528-532.
128. Peng, K., Y. Wu, H. Fang, X. Zhong, Y. Xu, and J. Zhu, *Uniform, Axial-Orientation Alignment of One-Dimensional Single-Crystal Silicon Nanostructure Arrays*. Angew. Chem. Int. Ed., 2005. **44**: p. 2737-2742.
129. Tripathy, S., R.K. Soni, S.K. Ghoshal, and K.P. Jain, *Optical properties of nano-silicon*. Bull. Mater. Sci., 2001. **24**(3): p. 285-289.
130. Каганович, Э.Б., Э.Г. Манойлов, И.Р. Базылюк, and С.В. Свечников, *Спектры фотолюминесценции нанокристаллов кремния*. ФТП, 2003. **37**(3): p. 353-357.
131. Magee, T.J., C. Leung, and H. Kawayoshi, *Getting of mobile oxygen and defect stability within back-surface damage regions in Si*. Appl. Phys. Lett., 1981. **38**(11): p. 891-893.
132. Skryshevsky, V.A., V.M. Zinchuk, A.I. Benilov, Y.S. Milovanov, and O.V. Tretyak, *Overcharging of porous silicon localized states at gas adsorption*. Semicond. Sci. Technol., 2006. **21**: p. 1605-1608.
133. Tretyak, O.V., V.A. Skryshevsky, V.A. Vikulov, B.Y. V., and V.M. Zinchuk, *Surface electronic states in metal-porous silicon-silicon structures*. Thin Solid Films, 2003. **445**: p. 144-150.

134. Skryshevskii, Y.A. and V.A. Skryshevskii, *Thermally stimulated luminescence in porous silicon*. Journal of Applied Physics, 2001. **89**(5): p. 2711-2714.
135. Sze, S.M., *Physics of semiconductor Devices*. 1981, New York: Wiley-Interscience Publ., Wiley & Sons.
136. Vdovenkova, T.A., V. Strikha, and V. Vikulov, *Auger electron spectroscopy study of the electronic structure of porous silicon-metal interfaces*. Journal of Electron Spectroscopy and Related Phenomena, 1997. **83**(2): p. 159-163.
137. Vo-Dinh, T., D.L. Stokes, G.D. Griffin, M. Volkan, U.J. Kim, and M.I. Simon, *Surface-enhanced Raman Scattering (SERS) Method and Instrumentation for Genomics and Biomedical Analysis*. Journal of Raman Spectroscopy, 1999. **30**: p. 785-793.
138. Ershov, M., R. H., A. Shik, and A.G.U. Perera, *Theory of transient spectroscopy of multiple quantum well structures*. Journal of Applied Physics, 1999. **86**(3): p. 1510-1513.
139. Ilchenko, V.V., S.D. Lin, C.P. Lee, and O.V. Tretyak, *Deep level transient spectroscopy characterization of InAs self-assembled quantum dots*. Journal of Applied Physics, 2001. **89**(2): p. 1172-1174.
140. Stein, B.L., E.T. Yu, E.T. Croke, A.T. Hunter, T. Laursen, J.W. Mayer, and C.C. Ahn, *Deep-level transient spectroscopy of Si/Si_{1-x}yGe_xC_y heterostructures*. Appl. Phys. Lett., 1998. **73**(5): p. 647-649.
141. Pinčik, E., P. Bartoš, M. Jergel, C. Falcony, J. Bartoš, M. Kučera, and J. Kákoš, *The metastability of porous silicon/crystalline silicon structure*. Thin Solid Films, 1999. **343-344**: p. 277-280.
142. Dittrich, T., K. Kliefoth, I. Sieber, J. Rappich, S. Rauscher, and V.Y. Timoshenko, *Electronic properties of thin Au/nanoporous-Si/n-Si structures*. Thin Solid Films, 1996. **276**: p. 183-186.
143. Lang, D.V., *Deep-level transient spectroscopy: A new method to characterize traps in semiconductors*. Journal of Applied Physics, 1974. **45**(7): p. 3023-3032.
144. Bube, R.H., *Photoelectronic Properties of Semiconductors*. 1992, Cambridge: Cambridge University Press.
145. Schroder, D.K., *Semiconductor Materials and Device Characterisation*. 1990, New York: Wiley.
146. Skryshevsky, V.A., V.M. Zinchuk, Y.S. Milovanov, A.I. Benilov, B.Y. V., O.V. Tretyak, and T. Dittrich. in *4th Int. Conf. Porous Semiconductors - Science and Technology*. 2004. Cullera-Valencia, Spain.
147. Dittrich, T. and V. Duzhko, *Photovoltage in free-standing mesoporous silicon layers*. phys. stat. sol. (a), 2003. **197**(1): p. 107-112.
148. Benilov, A.I., A.I. Tsyganova, S.V. Litvinenko, and V.A. Skryshevsky, *Eddy-current application for conductivity measurement in semiconductor sensing systems*. Bulletin of the University of Kyiv, 2005. **8**(Radiophysics and electronics): p. 11-13.
149. Oton, C.J., L. Pancheri, Z. Gaburro, L. Pavesi, C. Baratto, G. Faglia, and G. Sberveglieri, *Multiparametric porous silicon gas sensors with improved quality and sensitivity*. phys. stat. sol. (a), 2003. **197**(2): p. 523-527.
150. *Electromagnetic Testing (Eddy Current, Flux)*. Second ed. Nondestructive Testing Handbook. Vol. 4. 1986: ASNT.
151. Watanabe, T., K. Watamura, K. Kawatani, and H. Aoki, *Apparatus for inducing eddy current in a semiconductor wafer for measuring the electric conductivity or resistivity thereof*, in *United States Patents*. 1972: USA. p. 6.
152. Auld, B.A. and J.C. Moulder, *Review of Advances in Quantitative Eddy Current Nondestructive Evaluation*. Journal of Nondestructive Evaluation, 1999. **18**(1): p. 3-36.
153. Bareham, F.R., *Choice of frequency for eddy-current tube testing*. British Journal of Applied Physics, 1960. **11**: p. 218-222.

154. El-Hanany, U., *A Q-Meter Method for Measuring the Grain Size and the Resistivity Temperature Dependence of Metallic Powders*. Rev. Sci. Instrum., 1973. **44**(8): p. 1067-1068.
155. Benilov, A.I., M. Cabrera, V.A. Skryshevsky, and J.-R. Martin, *Porous silicon localization for implementation in matrix biosensors*. Materials Science and Engineering B, 2007. **139**: p. 221-225.
156. Bessueille, F., *Contribution à l'elaboration et à la lecture des puces à ADN*. 2001, Ecole Centrale de Lyon: Ecully.
157. Archer, M. and P.M. Fauchet, *Electrical sensing of DNA hybridization in porous silicon layers*. phys. stat. sol. (a), 2003. **198**(2): p. 503-507.
158. Chan, S., P.M. Fauchet, Y. Li, L.J. Rothberg, and B.L. Miller, *Porous Silicon Microcavities for Biosensing Applications*. phys. stat. sol. (a), 2000. **182**: p. 541-546.
159. van Noort, D., J. Rumberg, E.W.H. Jager, and C.-F. Mandenius, *Silicon based affinity biochips viewed with imaging ellipsometry*. Meas. Sci. Technol., 2000. **11**: p. 801-808.
160. Archer, M., M. Christophersen, and P.M. Fauchet, *Macroporous Silicon Electrical Sensor for DNA Hybridization Detection*. Biomedical Microdevices, 2004. **6**:3: p. 203-211.
161. Bell, T.E., P.T.J. Gennisen, D. DeMunter, and M. Kuhl, *Porous silicon as a sacrificial material*. J. Micromech. Microeng., 1996. **6**: p. 361-369.
162. Shirtcliffe, N.J., S. Aqil, C. Evans, G. McHale, M.I. Newton, C.C. Perry, and P. Roach, *The use of high aspect ratio photoresist (SU-8) for super-hydrophobic pattern prototyping*. J. Micromech. Microeng., 2004. **14**: p. 1384-1389.
163. Bras, M., V. Dugas, F. Bessueille, J.-P. Cloarec, J.-R. Martin, M. Cabrera, J.-P. Chauvet, E. Souteyrand, and M. Garrigues, *Optimisation of a silicon / silicon dioxide substrate for a fluorescence DNA microarray*. Biosensors and Bioelectronics, 2004. **20**: p. 797-806.
164. Robinson, G.M. and M.J. Jackson, *A review of micro and nanomachining from a materials perspective*. Journal of Materials Processing Technology, 2005. **167**: p. 316-337.
165. Yan, Y., T. Sun, Y. Liang, and S. Dong, *Investigation on AFM-based micro/nano-CNC machining system*. International Journal of Machine Tools & Manufacture, 2007. **47**: p. 1651-1659.
166. Ho, K.H. and S.T. Newman, *State of the art electrical discharge machining (EDM)*. International Journal of Machine Tools & Manufacture, 2003. **43**: p. 1287-1300.
167. Schumacher, B.M., *After 60 years of EDM the discharge process remains still disputed*. Journal of Materials Processing Technology, 2004. **149**: p. 376-381.
168. Lazarenko, B.R., *About the Inversion of Metal Erosion and Methods to Fight Ravage of Electric Contacts*. 1943. (**Moscow: WEI-Institut**) (**in Russian**).
169. Zhixin, J., A. Xing, and Z. Jianhua, *Study on mechanical pulse electric discharge machining*. Precision Engineering, 1995. **17**: p. 89-93.
170. Tsai, Y.-Y. and T. Masuzawa, *An index to evaluate the wear resistance of the electrode in micro-EDM*. Journal of Materials Processing Technology, 2004. **149**: p. 304-309.
171. Lauwers, B., J.P. Kruth, W. Liu, W. Eeraerts, B. Schacht, and P. Bleys, *Investigation of material removal mechanisms in EDM of composite ceramic materials*. Journal of Materials Processing Technology, 2004. **149**: p. 347-352.
172. Wong, Y.S., M. Rahman, H.S. Lim, H. Han, and N. Ravi, *Investigation of micro-EDM material removal characteristics using single RC-pulse discharges*. Journal of Materials Processing Technology, 2003. **140**: p. 303-307.
173. Lee, H.T. and T.Y. Tai, *Relationship between EDM parameters and surface crack formation*. Journal of Materials Processing Technology, 2003. **142**: p. 676-683.

174. Rebelo, J.C., A. Morao Dias, D. Kremer, and J.L. Lebrun, *Influence of EDM pulse energy on the surface integrity of martensitic steels*. Journal of Materials Processing Technology, 1998. **84**: p. 90-96.
175. Miller, S.F., A.J. Shih, and J. Qu, *Investigation of the spark cycle on material removal rate in wire electrical discharge machining of advanced materials*. International Journal of Machine Tools & Manufacture, 2004. **44**: p. 391-400.
176. Diver, C., J. Atkinson, H.J. Helml, and L. Li, *Micro-EDM drilling of tapered holes for industrial applications*. Journal of Materials Processing Technology, 2004. **149**: p. 296-303.
177. Klocke, F., D. Lung, D. Thomaidis, and G. Antonoglou, *Using ultra thin electrodes to produce micro-parts with wire-EDM*. Journal of Materials Processing Technology, 2004. **149**: p. 579-584.
178. Yan, M.-T. and H.-T. Chien, *Monitoring and control of the micro wire-EDM process*. International Journal of Machine Tools & Manufacture, 2007. **47**: p. 148-157.
179. Descoedres, A., C. Hollenstein, G. Walder, and R. Perez, *Time-resolved imaging and spatially-resolved spectroscopy of electrical discharge machining plasma*. J. Phys. D: Appl. Phys., 2005. **38**: p. 4066-4073.
180. Descoedres, A., *Characterization of Electrical Discharge Machining Plasmas*, in *La Faculte Sciences de Base, Centre de Recherche en Physique des Plasmas*. 2006, Ecole Polytechnique Federale de Lausanne: Lausanne.
181. Dhanik, S. and S.S. Joshi, *Modeling of a Single Resistance Capacitance Pulse Discharge in Micro-Electro Discharge Machining*. Journal of Manufacturing Science and Engineering, 2005. **127**: p. 759-767.
182. Lee, L.C., L.C. Lim, V. Narayanan, and V.C. Venkatesh, *Quantification of Surface Damage of Tool Steels After EDM* Int. J. Mach. Tools Manuf., 1998. **28**(4): p. 359-372.
183. Leao, F.N. and I.R. Pashby, *A review on the use of environmentally-friendly dielectric fluids in electrical discharge machining*. Journal of Materials Processing Technology, 2004. **149**: p. 341-346.
184. Kunieda, M., Y. Miyoshi, T. Takaya, N. Nakajima, Y.Z. Bo, and M. Yoshida. *High Speed 3D Milling by Dry EDM*. in *General Assembly of the International Academy for Production Engineering (CIRP)*. 2003. Montreal, Canada.
185. Mohd Abbas, N., D.G. Solomon, and M. Faud Bahari, *A review on current research trends in electrical discharge machining (EDM)*. International Journal of Machine Tools & Manufacture, 2006. doi:10.1016/j.ijmachtools.2006.08.026.
186. Egashira, K., A. Matsugasako, H. Tsuchiya, and M. Miyazaki, *Electrical discharge machining with ultralow discharge energy*. Precision Engineering, 2006. **30**(4): p. 414.
187. Reynaerts, D., W. Meeusen, and H. Van Brussel, *Machining of three-dimensional microstructures in silicon by electro-discharge machining*. Sensors and Actuators A, 1998. **67**: p. 159-165.
188. Reynaerts, D., W. Meeusen, X. Song, H. Van Brussel, S. Reyntjens, D. De Bruyker, and R. Puers, *Integrating electro-discharge machining and photolithography: work in progress*. J. Micromech. Microeng., 2000. **10**: p. 189-195.
189. Velten, T., H.H. Ruf, D. Barrow, N. Aspragathos, P. Lazarou, C.K. Erik Jung Malek, M. Richter, J. Kruckow, and M. Wackerle, *Packaging of bio-MEMS: strategies, technologies, and applications*. IBMT, Fraunhofer Inst. for Biomed. Eng., 2005. **28**(4): p. 533-546.
190. Allen, D.M., *Microelectrodischarge machining for MEMS applications*. Sch. of Ind. & Manuf. Sci., 2000: p. 6/1-6/4.
191. Schoth, A., R. Forster, and W. Menz, *Micro wire EDM for high aspect ratio 3D microstructuring of ceramics and metals*. Microsyst. Technol., 2005. **11**: p. 250-253.

192. Moylan, S.P., S. Chandrasekar, and G.L. Benavides, *High-Speed Micro-Electro-Discharge Machinig*, in *Sandia Report*. 2005, Sandia National Laboratories: Albuquerque.
193. Pham, D.T., S.S. Dimov, S. Bigot, A. Ivanov, and K. Popov, *Micro-EDM—recent developments and research issues*. *Journal of Materials Processing Technology*, 2004. **149**: p. 50-57.
194. Beltrami, I., C. Joseph, R. Clavel, J.-P. Bacher, and S. Bottinelli, *Micro- and nanoelectric-discharge machining*. *Journal of Materials Processing Technology*, 2004. **149**: p. 263-265.
195. Virwani, K.R., K.P. Rajurkar, and A.P. Malshe, *Current displacement (I-Z) spectroscopy-based characterization of nanoscale electro machining (nano-EM) tools*. *Proc. IMechE*, 2006. **220**(Part N): p. 21-27.
196. Malshe, A.P., K. Virwani, K.P. Rajurkar, and D. Deshpande. *Investigation of Nanoscale Electro Machining (nano-EM) in Dielectric Oil*. in *55th General Assembly of CIRP*. 2005. Atlanta, Turkey.
197. Fleischer, J., T. Masuzawa, J. Schmidt, and M. Knoll, *New applications for micro-EDM*. *Journal of Materials Processing Technology*, 2004. **149**: p. 246-249.
198. Takezawa, H., H. Hamamatsu, N. Mohri, and N. Saito, *Development of micro-EDM-center with rapidly sharpened electrode*. *Journal of Materials Processing Technology*, 2004. **149**: p. 112-116.
199. Yamazaki, M., T. Suzuki, N. Mori, and M. Kunieda, *EDM of micro-rods by self-drilled holes*. *Journal of Materials Processing Technology*, 2004. **149**: p. 134-138.
200. Kim, B.H., B.J. Park, and C.N. Chu, *Fabrication of multiple electrodes by reverse EDM and their application in micro ECM*. *J. Micromech. Microeng.*, 2006. **16**: p. 843-850.
201. Nam, A.J., A. Teren, T.A. Lusby, and A.J. Melmed, *Benign making of sharp tips for STM and FIM: Pt, Ir, Au, Pd, and Rh*. *J. Vac. Sci. Technol. B*, 1995. **13**(4): p. 1556-1559.
202. Melmed, A.J., *The art and science and other aspects of making sharp tips*. *J. Vac. Sci. Technol. B*, 1991. **9**(2): p. 601-608.
203. Lucier, A.-S., *Preparation and Characterization of Tungsten Tips Suitable for Molecular Electronics Studies*, in *Center for the Physics of Materials, Department of Physics*. 2004, McGill University: Montréal, Québec Canada. p. 129.
204. Binh, V.T., A. Piquet, H. Roux, R. Uzan, and M. Drechsler, *Sharpening of metal tips by heat treatment in vacuum*. *J. Phys. E: Sci. Instrum.*, 1976. **9**: p. 377-381.
205. Ludwig, M.H., J. Menniger, and R.E. Hummel, *Cathodoluminescing properties of spark-processed silicon*. *J. Phys.: Condens. Matter*, 1995. **7**: p. 9081-9089.
206. Allongue, P., P. Jiang, V. Kirchner, A.L. Trimmer, and R. Schuster, *Electrochemical Micromachining of p-Type Silicon*. *J. Phys. Chem. B*, 2004. **108**: p. 14434-14439.
207. Cabrera, M., M. Jaber, V. Dugas, J. Broutin, E. Vnuk, J.-P. Cloarec, E. Souteyrand, and J.-R. Martin, *Implementation of DNA chips obtained by microprojection for diagnostic and personalized medicine*. *Cellular and Molecular Biology*, 2004. **50**(3): p. 225-232.

AUTORISATION DE SOUTENANCE

Vu les dispositions de l'arrêté du 25 avril 2002,

Vu la demande du Directeur de Thèse

Monsieur Y. ROBACH

et les rapports de

Monsieur Ph. ALLONGUE
Directeur de Recherche CNRS - Laboratoire de Physique de la Matière Condensée
Ecole Polytechnique - 91128 PALAISEAU cedex

et de

Monsieur M. KLYUI
Professeur - V. Lashkarev Institute of Semiconductor Physics - National Academy of Science of Ukraine -
41 Prospect Nauki - Kyiv 03028 - Ukraine

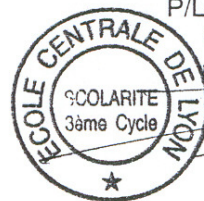
Monsieur BENILOV Artur

est autorisé à soutenir une thèse pour l'obtention du grade de **DOCTEUR**

Ecole doctorale ELECTRONIQUE, ELECTROTECHNIQUE, AUTOMATIQUE (EEA)

Fait à Ecully, le 10 juillet 2007

P/Le Directeur de l'E.C.L.
Le Directeur des Etudes



J. JOSEPH